NUMERICAL ANALYSIS OF A FLOATING HARBOR SYSTEM AND COMPARISON WITH EXPERIMENTAL RESULTS

A Thesis

by

HEONYONG KANG

Submitted to the Office of Graduate Studies of
Texas A&M University
in partial fulfillment of the requirements for the degree of

MASTER OF SCIENCE

May 2010

Major Subject: Ocean Engineering

NUMERICAL ANALYSIS OF A FLOATING HARBOR SYSTEM AND COMPARISON WITH EXPERIMENTAL RESULTS

A Thesis

by

HEONYONG KANG

Submitted to the Office of Graduate Studies of
Texas A&M University
in partial fulfillment of the requirements for the degree of

MASTER OF SCIENCE

Approved by:

Chair of Committee,	Moo-Hyun Kim
Committee Members,	Richard S. Mercier
	David A. Brooks
Head of Department,	John Niedzwecki

May 2010

Major Subject: Ocean Engineering

ABSTRACT

Numerical Analysis of a Floating Harbor System and Comparison with Experimental Results.

(May 2010)

HeonYong Kang, B.S., Pusan National University

Chair of Advisory Committee: Dr. Moo-Hyun Kim

As a comparative study, the global performance of two cases for a floating harbor system are researched by numerical analysis and compared with results from experiments: one is a two-body case such that a floating quay is placed next to a fixed quay, a normal harbor, and the other is a three-body case such that a container ship is posed in the middle of the floating quay and the fixed quay.

The numerical modeling is built based on the experimental cases. Mooring system used in the experiments is simplified to sets of linear springs, and gaps between adjacent bodies are remarkably narrow as 1.3m~1.6m with reference to large scales of the floating structures; a water plane of the fixed quay is 480m×160m, and the ship is 15000 TEU (twenty-foot equivalent unit) class.

With the experiment-based models, numerical analysis is implemented on two domains: frequency domain using a three dimensional constant panel method, WAMIT, and time domain using a coupled dynamic analysis program of moored floating structures, CHARM3D/HARP.

Following general processes of the two main tools, additional two calibrations are implemented if necessary: revision of external stiffness and estimation of damping coefficients. The revision of the external stiffness is conducted to match natural frequency of the simulation with that of the experiment; to find out natural frequencies RAO comparison is used. The next, estimation of damping coefficients is carried out on time domain to match the responses of the simulation with those of the experiment.

After optimization of the numerical analysis, a set of experimental results from regular wave tests is compared with RAO on frequency domain, and results from an irregular wave test of the experiment are compared with response histories of simulation on time domain. In addition, fender forces are compared between the simulation and experiment. Based on response histories relative motions of the floating quay and container ship are compared. And the floating harbor system, the three-body case, is compared with a conventional harbor system, a fixed quay on the portside of the container ship, in terms of motions of the container ship. As an additional simulation, the three-body case is investigated on an operating sea state condition.

From the present research, the experimental results are well matched with the numerical results obtained from the simulation tools optimized to the experiments. In addition, the floating harbor system show more stable motions of the container ship than the conventional harbor system, and the floating harbor system in the operating sea state condition have motions even smaller enough to operate in term of relative motions between the floating quay and the container ship.

This thesis is dedicated

to my parents and two sisters

with love and respect.

ACKNOWLEDGEMENTS

I would like to thank all those who have stood by me and helped throughout the course of this research. First of all, I sincerely appreciate my committee chair, Dr. M.H. Kim, for giving me great opportunities and providing me with thoughtful guidance and cheerful support. And I thank my committee members, Dr. Mercier and Dr. Brooks, for their invaluable advice and encouragement.

Heartfelt thanks also go to my friends and colleagues and the department faculty and staff for making my time at Texas A&M University a great experience. I also want to extend my gratitude to the senior engineers from Dr. M.H. Kim's research group: Dr. S.J. Lee, Dr. S.S. Ryu, and S.H. Lim, for helping make smooth progress in research. In addition, I'd like to express my sincere gratitude to Dr. J.H. Kim at KORDI for providing precious experimental data.

Finally, thanks to my father, MyeongKi Kang, my mother, YeongDoo Jeong, and my sisters, JiHye Kang and JiSook Kang, deeply.

TABLE OF CONTENTS

LIST OF FIGURES

Page

Page

Page

LIST OF TABLES

CHAPTER I

INTRODUCTION

With globalization, the number of international trades has been grown up as shown in Fig. 1.1; in other words, the capacity of container traffic is directly related to power of growth in the current global era. In the meantime, sustainable development has become a world-wide problem owing to global warming. Based on these two remarkable points, demand of an alternative harbor system has been increasing, which has expanded capacity and is built by eco-friend construction.

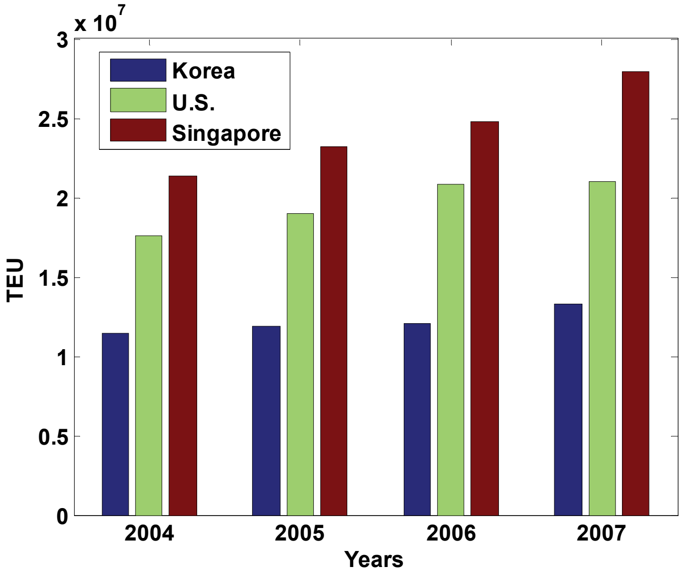

Figure 1.1 Increasing Container Traffic (Source: AAPA World Port Rankings)

This thesis follows the style of Ocean Engineering.

For recent years, as the alternative a Floating Harbor System, which has a floating quay as additional container terminal on the sea around a normal harbor on land, has been researched by numerical analysis and experiment. A research group under Dr. Moo-Hyun Kim, Texas A&M University, had carried out the numerical analysis of the floating harbor system as a preliminary research. On the other hands, the experiments of the Floating Harbor System had been conducted at Korea Ocean Research & Development Institute (KORDI), Korea, which applies narrow gaps, mooring system of real fenders and hawser lines, and geographical features, which is more practical in comparison with numerical analysis conditions.

In this research, two experimental cases of the floating harbor system conducted by KORDI are analyzed by numerical analysis and the results from the simulations are compared with those from experiment.

For decades, a lot of researches about various topics related to the present research topic had been carried out. As multiple-body analysis, Kodan (1984) examined the two slender bodies posed parallel in oblique waves. Sannasiraj et al. (2000) studied multiple-body's dynamics in multi-directional waves using finite element method. For the narrow gap, Huijsmans et al. (2001) applied lid on the gaps. Furthermore, as the Liquefied Natural Gas (LNG) market is growing, Buchner et al. (2001) studied the interaction of LNG carrier and FPSO moored side by side, and Buchner et al. (2004) examined the motions and mooring loads of multiple-body focused on narrow gaps between LNG carrier and FPSO.

Concerning a box-shaped floating structure, which is the shape of the floating quay, Chen and Huang (2004) carried out the time-domain simulation of floating pier/ship around harbor in potential flow. And for resonance phenomena, Lee and Kim (2005) studied about the interaction of two-body resonance by full and partial coupling.

In terms of the comparative study of numerical simulation and experiments, two researches of LNG system, LNG carrier and FPSO or shuttle tankers, had done. Inoue and Islam (1999) analyzed the system on both frequency domain based on linear wave theory and time domain based on analysis of dynamics coupled by mooring system. On the other hand, Hong et al. (2005) analyzed the system on frequency domain based on second order wave theory. As an initiative step of the floating harbor system, Kim et al. (2006) researched into numerical analysis of the floating harbor system on both frequency domain and time domain. The analysis on frequency domain is based on linear wave potential theory, and that on time domain includes nonlinearities of fluid and coupled dynamics.

In this study, general method is based on Kim et al. (2006). Furthermore, two calibrating processes are implemented if necessary as shown in Fig. 1.2; the first calibration is stiffness revision to match natural frequencies with those of experiment, and the second is estimation of damping force to match the responses with those of experiment. In Chapter II, two-body case of the floating harbor system is investigated; the floating quay is posed next to the fixed quay. In Chapter III, three-body case is examined, which consists of the floating quay on the starboard of the 15000TEU container ship and the fixed quay on the portside of the ship.

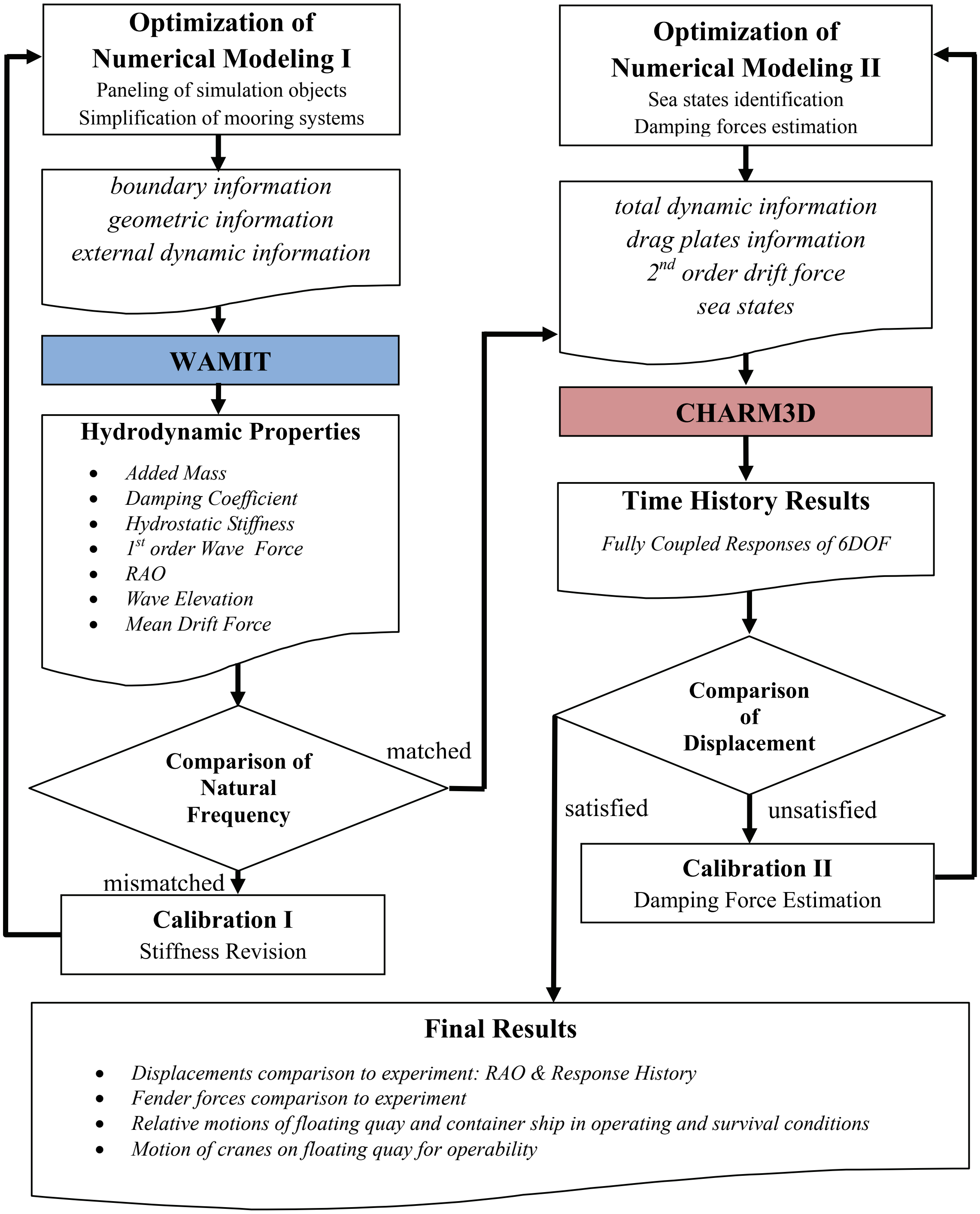

Figure 1.2 General Process

CHAPTER II

TWO-BODY ANALYSIS: FLOATING QUAY AND FIXED QUAY

2.1 Introduction

To examine the survivability of floating quay in a severe sea state, this two-body case is taken up, which is the floating quay moored to the fixed quay. In experiment, a series of regular wave tests with wave height 0.7m were conducted, and an irregular wave test with significant wave height 2.5m were carried out.

In this chapter, numerical modeling is at first investigated such as panel modeling, simplification of fenders/hawsers. Based on the experiment-based modeling, both of frequency domain analysis and time domain analysis are conducted. In frequency domain analysis, hydrodynamic properties and response are calculated at each wave frequency using WAMIT. And Response Amplitude Operator (RAO)'s obtained by WAMIT are compared with the experimental regular wave test results. In time domain analysis, the irregular wave test is carried out using CHARM3D; hydrodynamic properties are imported from WAMIT, and the responses are calculated based on stokes wave theory such that an irregular wave is made by superposition of a set of regular waves. The response histories obtained by CHARM3D are compared with experimental irregular wave test results. Furthermore, total RAO's are compared such that the experimental regular wave tests and WAMIT RAO results are compared with spectrum RAO's obtained from both of experimental and numerical response histories.

2.2 Frequency Domain Analysis

In frequency domain analysis, two simulation cases are conducted to analyze the two-body case, which are distinguished from modeling of the fixed quay; one is that the fixed quay is paneled by user, and the other is that the fixed quay is automatically generated in WAMIT. The first case is explained from Section 2.2.1 to 2.2.6, and the next case is explained in Section 2.2.7.

Theoretically, the ocean is assumed as ideal fluid based on the linear velocity potential theory; ideal fluid represents inviscid, incompressible, and irrotational flow, and the linear velocity potential theory is first order wave theory derived from linear boundary conditions (Newman, 1967).

Using WAMIT, two differential equations are solved: Laplace equation, which is a Partial Differential Equation (PDE) to get the velocity potential, and Motion equation, which is an Ordinary Differential Equation (ODE) to get the response at each frequency.

2.2.1 Boundary Information

The Laplace Equation, equation (2.1), is derived from Mass Conservation and Momentum Conservation of ideal fluid.

$$\nabla^2\Phi_T = 0 \quad where,\ \Phi_T = \Phi_I + \Phi_S + \Phi_R \qquad (2.1)$$

From the superposition principle of linear theory, total velocity potential Φ_T is made of three velocity potentials such as incident velocity potential Φ_I, scattered (reflected) velocity potential Φ_S, and radiated velocity potential Φ_R. And the Φ_T should satisfy a set of linear boundary conditions. In addition to general boundary conditions like bottom boundary condition, kinematic/dynamic free surface boundary condition, and radiation condition, the body surface boundary condition, which is generated by wetted surface of a floating structure, is also included.

To set up the general boundary conditions, boundary information which consists of water depth, wave heading, and wave frequency region are specified; wave frequency region imply the region of discrete wave frequencies to be calculated in WAMIT.

In this comparative study, boundary information is based on the experiments: water depth is 18m, wave heading is 135 degree with respect to positive x axis, and wave frequency region is 0.01 rad/sec to 1.6 rad/sec. The reason that the minimum frequency is 0.01 rad/sec is that certain natural frequencies of floating quay are expected to be below 0.1 rad/sec due to the small external stiffness. And 25 discrete wave frequencies in the frequency region are input with the frequencies denser in low frequency region.

2.2.2 Geometric Information

To set the body surface boundary condition, the wetted surface of floating structures are input by a set of quadrilateral panels as geometric information; it can be input with triangular panels if necessary.

With the paneling criteria above, floating quay and fixed quay of experiment are paneled from the particulars of the floating quay and the schematic as given in Table 2.1 and Fig. 2.1. The geometric information is given by coordinates of each panel's vertices.

Table 2.1 Geometric Particulars of Floating Quay

	Floating Quay
Length [meter]	480
Breadth [meter]	160
Draft [meter]	6
Shape of Submerged Part	Simple box barge type

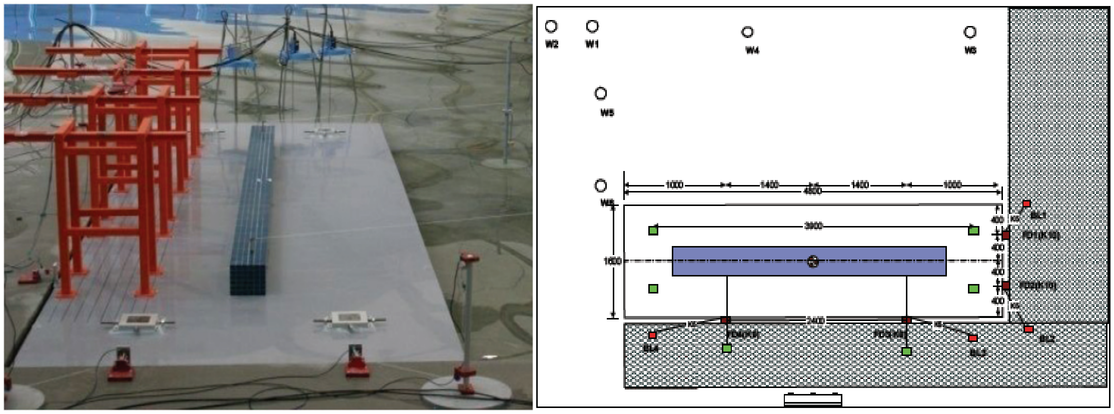

Figure 2.1 Experimental Schematic of Two-body Case

For floating quay and fixed quay, 3840 and 2965 panels are used respectively. In Fig. 2.2, the fixed quay, green panels, is modeled as slightly longer in x direction and twice longer in y direction than the floating quay, yellow panels, from the experimental schematic. On the right and bottom of the figure, fixed quay has larger draft than floating quay because the draft of fixed quay is same as water depth. In the x-y plane, the origins of each body coordinate system are indicated and the enlarged figure shows remarkably narrow gap as 1.3m. In this case, the origin of floating quay's body coordinate system is simultaneously set as the origin of global coordinate system for this two-body case. In addition, all origins of the coordinate systems are placed on mean water line.

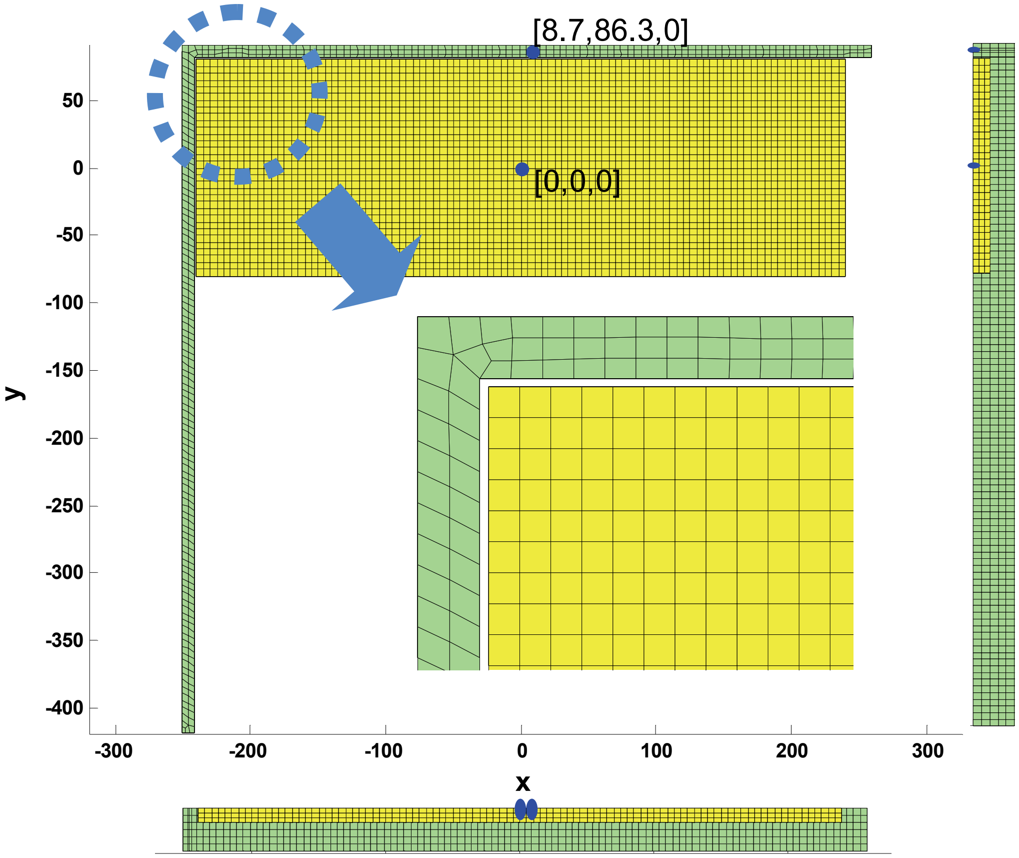

Figure 2.2 Panel Modeling and Arrangement of Two-body Case; Center Is x-y Plane, Right Is y-z Plane, and Bottom Is x-z Plane

From the set of boundary conditions as given so far, velocity potentials are calculated at the center of each panel, and the velocity potential in each panel is assumed to be constant.

As velocity potentials on the whole panels, which represents the effect of fluid on the floating structure, are obtained, hydrodynamic properties are calculated at each frequencies: added mass, radiation damping coefficient, first order wave force (exciting force), mean drift force, RAO, and free surface elevation.

2.2.3 External Dynamic Information

Section 2.2.1 to 2.2.2 dealt with the input to solve the PDE, the first equation of two equations solved by WAMIT as mentioned at the beginning of the frequency domain analysis. This section accounts for the inputs to solve the ODE, the next equation of the two equations, as a motion equation of the floating structures.

Mathematically, it is non-homogeneous with constant coefficients, and it is physically a motion equation for forced vibrating motion of damped mass-spring system. In this regard, vibrating object is a floating structure and components of the equation such as mass, spring, and damping are reformed owing to the interaction with ocean and mooring system from general ODE like equation (2.2) to equation (2.3).

$$M\ddot{X} + C\dot{X} + KX = F \tag{2.2}$$

$$(M + \Delta M_{\omega})\ddot{X}_{\omega} + (C_{R\omega} + C_{E})\dot{X}_{\omega} + (K_{E} + K_{H})X_{\omega} = F_{W1\omega} \tag{2.3}$$

For the mass component, added mass is added to the mass of the floating structure to account for resistance of fluid against structure's accelerated/decelerated motion. And the total mass as sum of structure mass M (external mass) and added mass ΔM_{ω} is referred to as "virtual mass". In the spring term K, both the stiffness of structure (external stiffness K_E) and hydrostatic stiffness K_H by gravity are applied. The third component, damping coefficient C can consist of radiation damping coefficient $C_{R\omega}$ from the radiation/diffraction theory, and viscous damping or external damper (external damping coefficient C_E). Subscript ω represents that the values are the function of each incident wave frequency; for instance, if $\omega = 0.5 rad/\sec$, ΔM , C_R, and F_{W1} are calculated for the frequency 0.5 rad/sec and then the response X is calculated for the frequency as well.

To solve the motion equation at each frequency, two groups of inputs are substituted into the motion equation: hydrodynamic properties obtained from the velocity potentials at each frequency and the coefficients such as M , K_E, C_E. In this Section 2.2.3, we set the coefficients of the floating quay, which are supposed to input by user, based on the experiment information.

For the fixed quay, it is fixed as a part of land around the floating quay. Thus, we assume that the fixed quay has as enormous mass and stiffness, 10 times more than those of the floating quay. Thus, the process to get the external dynamic information of the fixed quay is omitted.

2.2.3.1 External Mass Matrix

Theoretically, the equation (2.3) is obtained by solving linear and angular momentum equation with respect to 6 Degree of Freedom (DOF) motions of each body. Thus, if N is the number of floating bodies, the 6×N ODE's are given for 6×N DOF motions, including coupling effects in the 6×N DOF motions: surge-pitch coupling, sway-roll coupling (Mercier, 2004).

Using WAMIT, the set of equations are formed as matrix equations. As parts of the external matrix M mass matrix of each body is input by

$$M = \begin{bmatrix} m & 0 & 0 & 0 & mz_{CG}^{B} & -my_{CG}^{B} \\ 0 & m & 0 & -mz_{CG}^{B} & 0 & mx_{CG}^{B} \\ 0 & 0 & m & my_{CG}^{B} & -mx_{CG}^{B} & 0 \\ 0 & -mz_{CG}^{B} & my_{CG}^{B} & \mathrm{I}_{XX}^{B} & -\mathrm{I}_{YX}^{B} & -\mathrm{I}_{Zx}^{B} \\ mz_{CG}^{B} & 0 & -mx_{CG}^{B} & -\mathrm{I}_{XY}^{B} & \mathrm{I}_{YY}^{B} & -\mathrm{I}_{ZY}^{B} \\ -my_{CG}^{B} & mx_{CG}^{B} & 0 & -\mathrm{I}_{XZ}^{B} & -\mathrm{I}_{YZ}^{B} & \mathrm{I}_{ZZ}^{B} \end{bmatrix} \tag{2.4}$$

which has ten independent variables;

m : mass of the structure,

$[x_{CG}^{B}, y_{CG}^{B}, z_{CG}^{B}]$: coordinates of center of gravity with respect to body coordinate system,

$[I_{XX}^{B}, I_{YY}^{B}, I_{ZZ}^{B}, I_{XY}^{B}, I_{YZ}^{B}, I_{ZX}^{B}]$: mass moment of inertia with respect to body coordinate system, where $I_{XY}^{B} = I_{YX}^{B}$, $I_{XZ}^{B} = I_{ZX}^{B}$, and $I_{ZY}^{B} = I_{YZ}^{B}$.

In the present study, the external mass matrix of floating quay is input as equation (2.5) from the particulars in Table 2.2; the particulars are given by KORDI and the mass of body is checked with the displacement calculated from WAMIT.

Table 2.2 Inertia Particulars of Floating Quay

	Floating Quay
Mass	4.7232E+008 kg
C.G.	[0 , 0 , 0.14]
$[I_{XX}^{B}, I_{YY}^{B}, I_{ZZ}^{B}]$	[2.16E+012 , 7.5E+012 , 9.5E+012]
$[I_{XY}^{B}, I_{YZ}^{B}, I_{ZX}^{B}]$	[0 , 4E+010 , -2.21E+009]

$$M = \begin{bmatrix} 4.7232\text{E}+8 & 0 & 0 & 0 & 6.6125\text{E}+7 & 0 \\ 0 & 4.7232\text{E}+8 & 0 & -6.6125\text{E}+7 & 0 & 0 \\ 0 & 0 & 4.7232\text{E}+008 & 0 & 0 & 0 \\ 0 & -6.6125\text{E}+7 & 0 & 2.16\text{E}+12 & 0 & -2.21\text{E}+9 \\ 6.6125\text{E}+7 & 0 & 0 & 0 & 7.5\text{E}+12 & 4\text{E}+10 \\ 0 & 0 & 0 & -2.21\text{E}+9 & 4\text{E}+10 & 9.5\text{E}+12 \end{bmatrix} \quad (2.5)$$

2.2.3.2 External Stiffness Matrix

In the matrix equation of equation (2.3), the K_E is also 6N×6N, and it accounts for the external mooring system of floating structures as simplified linear springs for 6 DOF motions.

In a general numerical analysis, the best option is that certain mooring system is simplified as linear spring on frequency domain, and then altered to real mooring system on time domain by CHARM3D. The reasons that the simplified stiffness is input on frequency domain are at first WAMIT solves only the ODE with constant coefficients and secondly mean drift force results on frequency domain is dependent on the stiffness. Thus, to get more accurate mean drift forces and responses on frequency domain, the simplified linear spring is indispensible.

In the present study, the numerical modeling is based on experimental structures, which are moored by fenders and hawsers; on frequency domain the mooring system is simplified to external stiffness on frequency domain, and moreover the use of simplified stiffness is extended to time domain analysis owing to the complexity of this system such as large scaled three bodies with narrow gap.

In the experiment of this two-body case, floating quay is moored to the fixed quay by fenders and mooring lines, which mainly suppress surge, sway, and yaw as shown in Fig. 2.3.

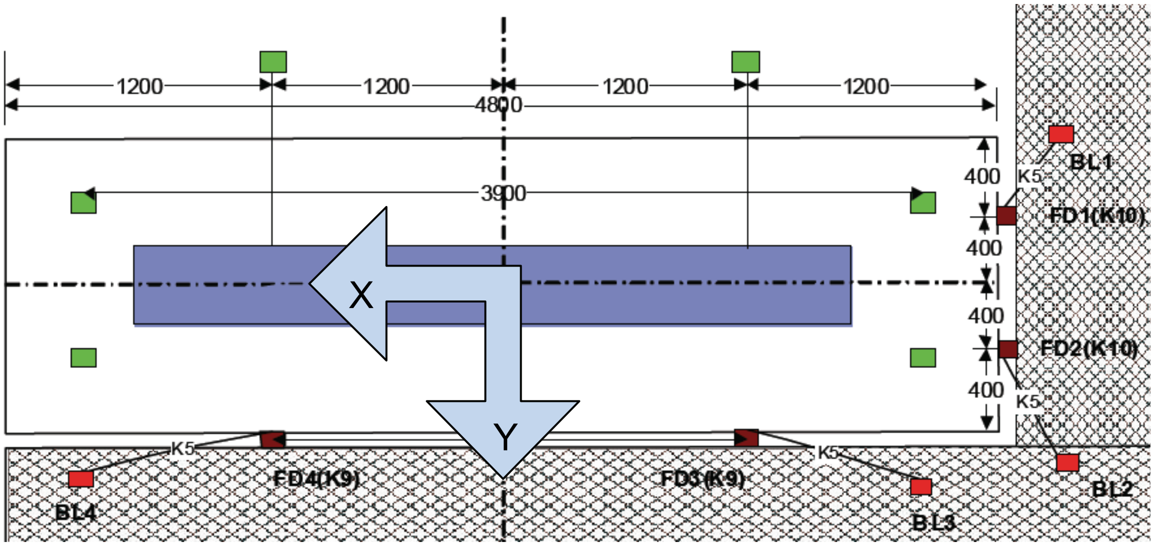

Figure 2.3 Schematic of Mooring System for Two-body Case

The hawser lines indicated as K5 and fenders as K9 or K10 are equipped at four points with stiffness as Table 2.3.

Table 2.3 Stiffness of Mooring System

Mooring System	Spring type	Stiffness (ton/m)
K5 (MOORING LINE)	Tension	8031.5
K9 (Fender, Longitudinal side)	Compression	12613
K10 (Fender, Lateral side)	Compression	4376

Before the simplification of the fenders and hawsers to linear spring stiffness, one thing should be recognized; the floating quay has two types of stiffness for one motion; for example, K5, mooring line stiffness, acts for negative sway motion, and for positive sway motion K9, fender stiffness, would work. Thus to apply the system to the simplified spring stiffness, which represents only one stiffness regardless of the direction of a motion, the two stiffness should be estimated as one value.

As an alternative, a single stiffness is obtained from reaction force data of hawser and fender measured in the experiment. The approximated stiffness of each motion is given in Table 2.4.

Table 2.4 Linear Spring Stiffness of Two-body Case

Motion	Stiffness (N/m)
SURGE	1.3E+7
SWAY	2.3E+7
HEAVE1	1.15E+7
HEAVE2	0.65E+7

And to calculate matrix K_E, the linear springs are assumed to act on the same positions as hawsers/fenders in Fig. 2.4. And the positions are given in Table 2.5.

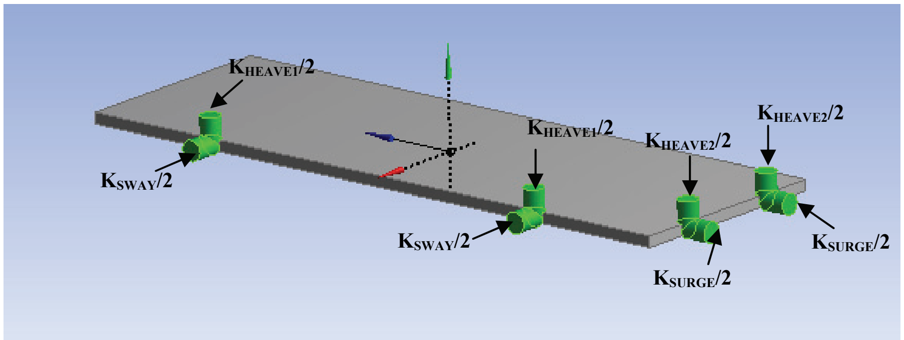

Figure 2.4 Schematic of Linear Springs

Table 2.5 Spring Positions of Two-body Case

Point Number	**Coordinates**
P1	(120, 80, 2)
P2	(-120, 80, 2)
P3	(-240, 40, 2)
P4	(-240, -40, 2)

Assuming the linear springs as given by Fig. 2.4 and Table 2.5, external stiffness of rotational motions and coupled motions between 6×N motions are calculated by formula below; the calculation is based on the principal that stiffness of certain mode represents the total external restoring force induced by unit displacement of the mode.

In case of roll, if floating body has unit roll angle, the external restoring force by eight springs are

$$K_{roll} = K_{sway} \times P1_z^{\ 2} + K_{heave1} \times P1_y^{\ 2} = 2.3E+07 \ \times 2^2 + 1.15E+07 \times 80^2$$
$$= 7.3692\mathrm{E}+010 \ \mathrm{Nm/rad} \tag{2.6}$$

In the same manner, respective external stiffness of pitch and yaw is given by

$$K_{pitch} = K_{surge} \times P3_z^{\ 2} + K_{heave2} \times P3_x^{\ 2} = 1.3E+07 \ \times 2^2 + 0.65E+07 \times 240^2$$
$$= 3.7445\mathrm{E}+011 \ \mathrm{Nm/rad} \tag{2.7}$$

$$K_{yaw} = K_{surge} \times P3_y^{\ 2} + K_{sway} \times P1_x^{\ 2} = 1.3E+07 \ \times 40^2 + 2.3E+07 \times 120^2$$
$$= 3.52\mathrm{E}+011 \ \mathrm{Nm/rad} \tag{2.8}$$

In that the springs are acting on the points off the origin of the body coordinate system, the springs generate coupled stiffness between translational and rotational motions. Thus, the coupled stiffness is calculated as

$$K_{surge-pitch} = K_{surge} \times P1_z = 1.3E+07 \ \times 2 = 2.6\mathrm{E}+07 \ \mathrm{N} \tag{2.9}$$

$$K_{sway-roll} = -K_{sway} \times P3_z = -2.3E+07 \ \times 2 = -4.6\mathrm{E}+07 \ \mathrm{N} \tag{2.10}$$

$$K_{heave1-roll} = K_{heave1} \times P1_y = 1.15E+07 \times 80 = 9.2\mathrm{E}+08\mathrm{N} \tag{2.11}$$

$$K_{heave2-pitch} = K_{heave2} \times P3_x = 0.65E+07 \times 240 = 1.56\mathrm{E}+09\mathrm{N} \tag{2.12}$$

Summing up, the external stiffness is input as

$$K_E = \begin{bmatrix} 1.3\mathrm{E}+7 & 0 & 0 & 0 & 2.6\mathrm{E}+7 & 0 \\ 0 & 2.3\mathrm{E}+7 & 0 & -4.6\mathrm{E}+7 & 0 & 0 \\ 0 & 0 & 1.8\mathrm{E}+7 & 9.2\mathrm{E}+8 & 1.56\mathrm{E}+9 & 0 \\ 0 & -4.6\mathrm{E}+7 & 9.2\mathrm{E}+8 & 7.3692\mathrm{e}+10 & 0 & 0 \\ 2.6\mathrm{E}+7 & 0 & 1.56\mathrm{E}+9 & 0 & 3.7445\mathrm{e}+11 & 0 \\ 0 & 0 & 0 & 0 & 0 & 3.52\mathrm{E}+11 \end{bmatrix} \tag{2.13}$$

2.2.3.3 External Damping Coefficient Matrix

In general, using external damping coefficient matrix C_E , constant damping coefficient is applied to the ODE, and the constant coefficients can account for linear viscous roll damping or a constant external damper.

However, in the present study, C_E is assumed to be zero on frequency domain. And damping force including various kinds of damping effects from viscous damping to eddy damping is applied in time domain analysis.

2.2.4 Results of Hydrodynamic Properties

As mentioned with equation (2.3) hydrodynamic properties such as added mass ΔM , radiation damping coefficient C_R, hydrostatic stiffness K_H , first order wave force F_{W1} , and second order wave force F_{W2} (mean drift force) are calculated by solving the Laplace Equation with a set of boundary equations at each incident wave frequency using WAMIT.

The separate results based on the 25 discrete frequencies are connected by linear interpolation.

In this research, the linear velocity potential is obtained by source formulation on each panel and integrated by Green Theorem. And the effect of irregular frequencies, a well-known mathematical problem of the velocity potential theory, is not removed.

2.2.4.1 Added Mass / Added Moment of Inertia

Theoretically, added mass/moment of inertia of each motion ΔM_{ij} is calculated by surface integral of real part of certain radiation velocity potential relevant to the motion Φ_{Ri} along boundary surface;

$$\Delta M_{ij} = \rho \iint_{SB} \mathrm{Re}\{\Phi_{Ri} \cdot n_j\} ds \tag{2.14}$$

For instance, ΔM_{14} is added mass of surge motion generated by roll motion.

The results of the present two-body case are shown in Fig. 2.5 for 6 DOF pure motions. Based on the fact that coupling terms ΔM_{ij} where $i \neq j$ is relatively quite small, generally less than 10% of results for pure motions, the coupling results are omitted in the figures; however, all the coupling terms are input in numerical analysis. In Fig. 2.5, there are several peaks suddenly changed owing to pumping modes generated on gaps between adjacent bodies; 1.3m gap between floating quay and fixed quay in both longitudinal and transverse sides. In addition, irregular frequency results also can cause those peaks.

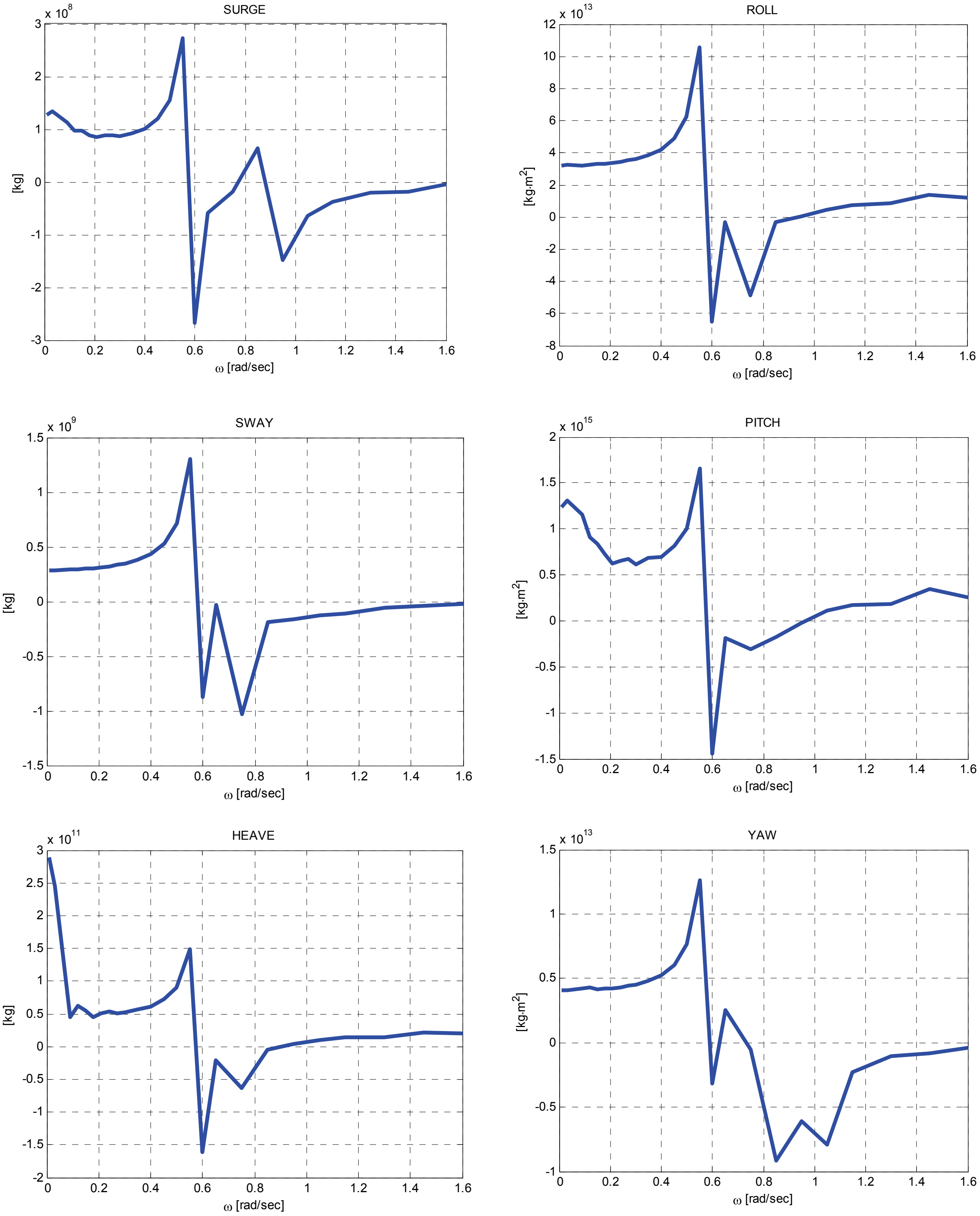

Figure 2.5 Added Mass / Moment of Inertia of Floating Quay, 2-body Case

2.2.4.2 Radiation Damping Coefficient

Radiation damping coefficient is also obtained from $\Phi_{R\,i}$ for each motion similarly with added mass; however, the integrand is imaginary part of $\Phi_{R\,i}$ in the damping coefficient;

$$C_{R\,ij} = \rho \iint_{SB} \mathrm{Im}\{\Phi_{Ri} \cdot n_j\} ds \tag{2.15}$$

The results of floating quay are obtained as shown in Fig. 2.6 for 6 DOF pure motions. The results from the coupled motions are also omitted based on the same reason as plotting the added mass.

Physically, the radiation damping represents energy dissipation by generating waves through 6 DOF motions of certain body. In general, a well-known week point of numerical analysis is underestimated radiation damping coefficient of roll motion.

In this frequency domain analysis, the intact C_R of roll motion is used. And then, on time domain external linear damping coefficient is applied for the roll motion.

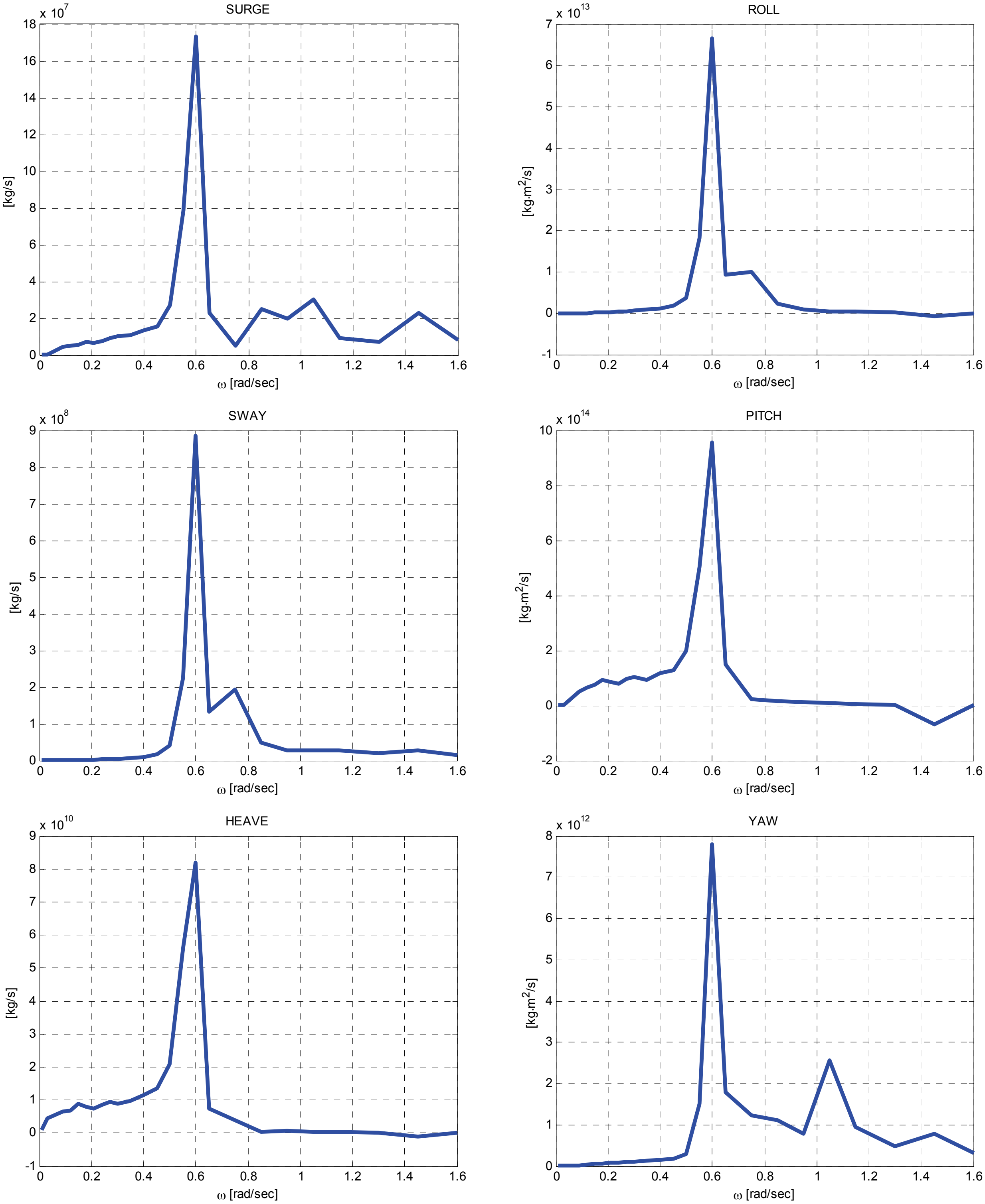

Figure 2.6 Radiation Damping Coefficients of Floating Quay, 2-body Case

2.2.4.3 First Order Wave Force/ Moment

Unlike added mass and damping coefficient by Φ_{Ri}, first order wave force F_{W1} is calculated from diffraction velocity potential Φ_D;

$$\Phi_D = \Phi_I + \Phi_S \tag{2.16}$$

F_{W1} is usually named as "Wave Exciting Force/Moment", and the formula is obtained by direct integration of hydrodynamic pressure as

$$F_{W1_i} = i\omega\rho A \iint_{SB} \Phi_D n_i dS \tag{2.17}$$

A is amplitude of the incident wave and assumed to be 1m here, and the results are shown in Fig. 2.7; the real parts of the wave exiting force/moment are plotted.

2.2.4.4 Mean Drift Force/Moment

From the equation 2.3, we can recognize this frequency domain analysis deals with only linear wave effects; however, to analyze the wave effects more accurately, the velocity potential need to be calculated by extension of the boundary condition from first order to second order. From the extension, the most remarkable change is an additional force term F_{W2}, which consists of functions of two variables: difference frequencies and sum frequencies.

In general, the difference frequency component is named as Drift Force/Moment, and the sum frequency component is called as Springing Force/Moment. Except for the Tension Leg Platform (TLP), the effect of the springing force is usually neglected; in the meantime, the drift force is generally applied to the system since the drift force can be a significant excitation force in low frequency region, where natural frequencies of general floating bodies are placed. Thus, to clarify the resonance phenomena, the drift force should be applied to the numerical analysis.

Nevertheless, cost to calculate the exact drift force is too expensive related to the calculation of other properties based on the linear wave theory. Thus, an alternative is usually adopted using the mean drift force. The mean drift force is a main component of the exact drift force; at the same time, it can be obtained by linear velocity potential. Furthermore, since the main purpose is to examine resonance, the magnitude can have somewhat tolerance. Thus, an approximation method applicable in time domain analysis, Newman's Approximation, is used in a general numerical analysis. The method approximates the drift force directly from the mean drift force.

Therefore, in this study, mean drift force is obtained from frequency domain analysis as shown in Fig. 2.8 and the approximation method is implemented in time domain analysis; the results plotted in Fig. 2.8 are the real parts of the mean drift force/moment. Theoretically, mean drift force F_{Dii} is drift force of mono-chromatic wave and obtained by boundary surface integral of pressure p normal to the surface;

$$F_{Dii} = \overline{\iint_{SB} (\vec{N}p)ds} \quad , \quad M_{Dii} = \overline{\iint_{SB} (\vec{X} \times \vec{N})pds} \tag{2.18}$$

$\vec{N}$ is normal vector at the center of each panel and $\vec{X}$ represent the position vector. The bar means time averaging and M_{Dii} is mean drift moment for rotational motion; the pressures are obtained from the linear velocity potential.

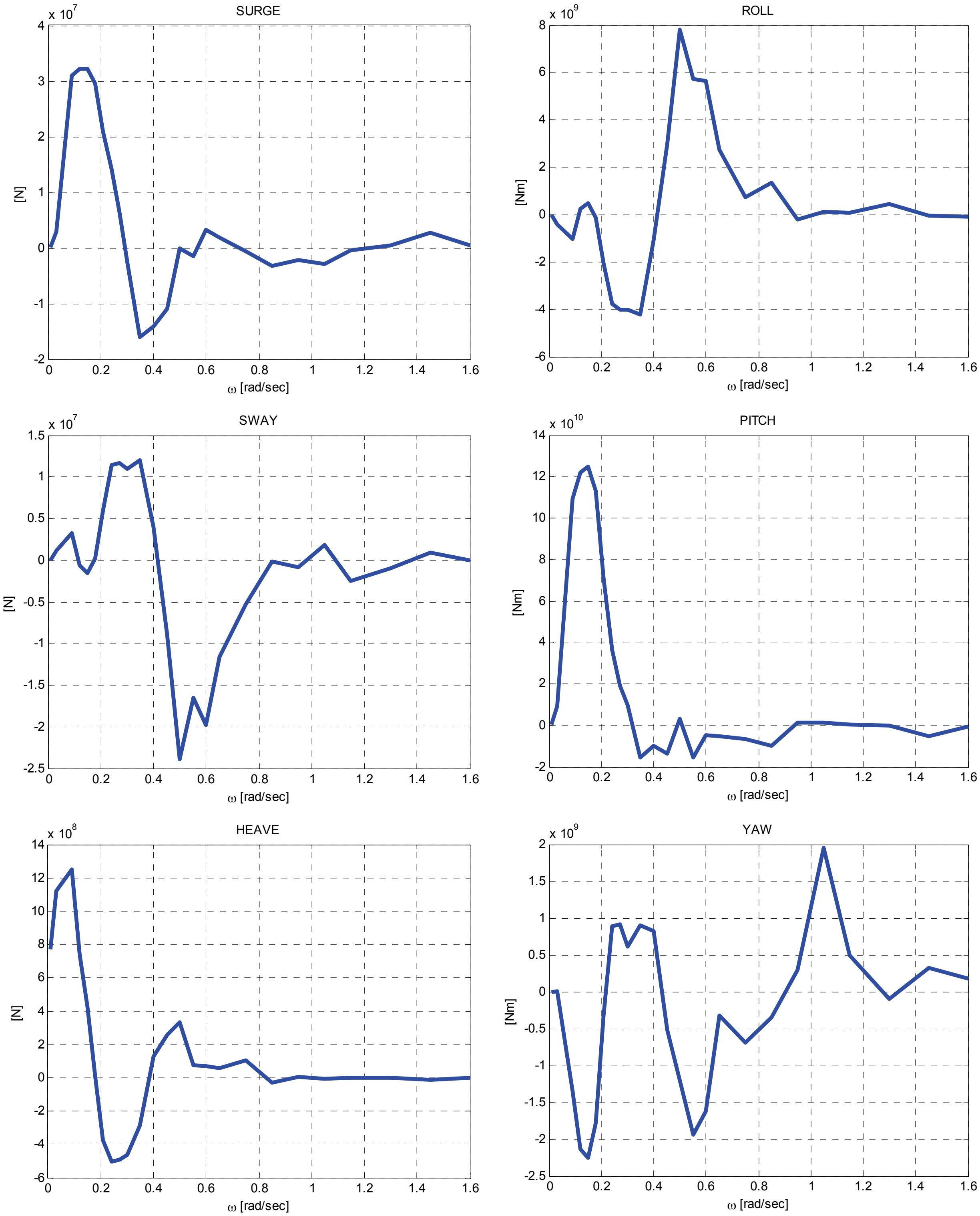

Figure 2.7 First Order Wave Force of Floating Quay, 2-body Case

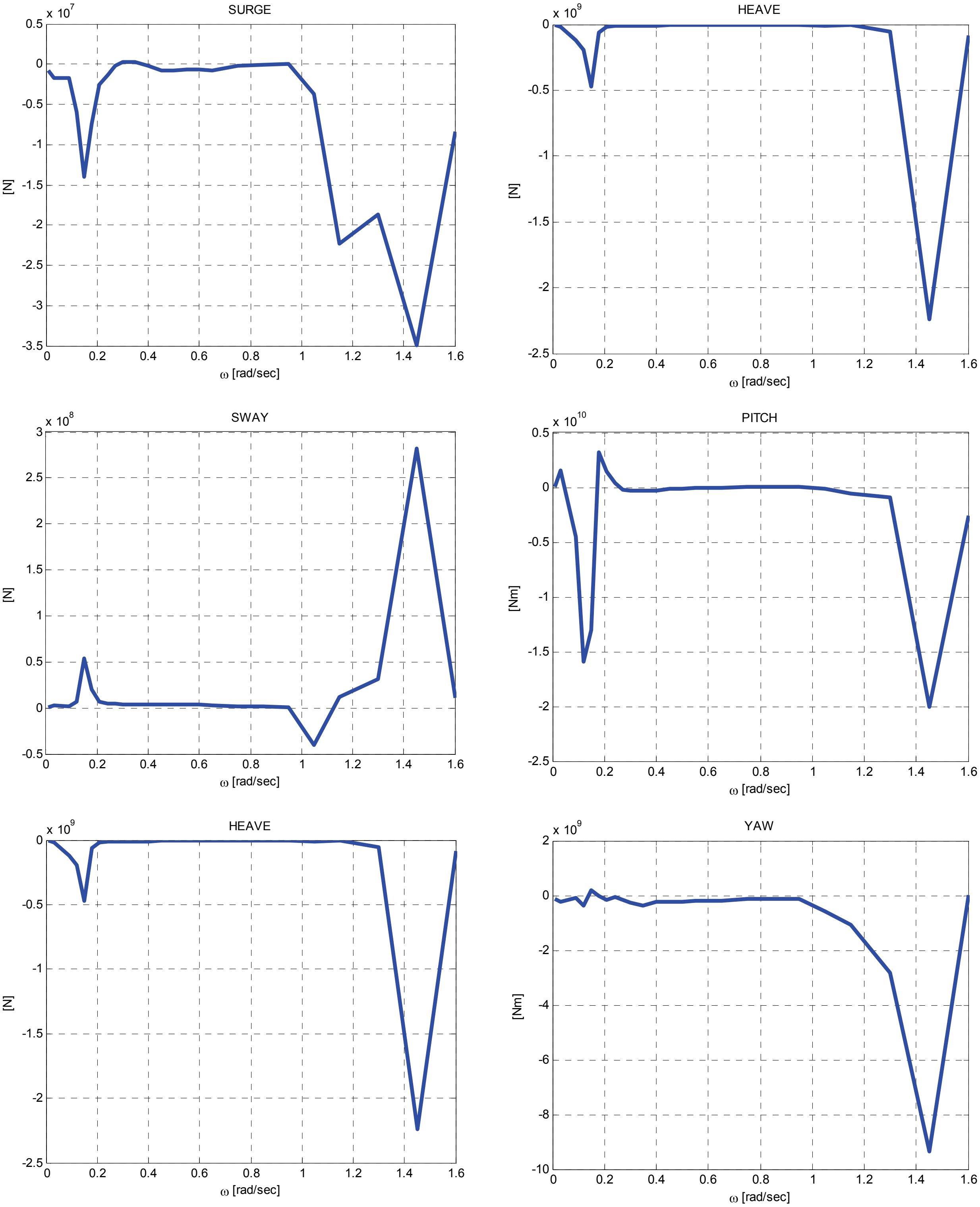

Figure 2.8 Mean Drift Force of Floating Quay, 2-body Case

2.2.5 RAO Comparison

Substituting the external dynamic information and hydrodynamic properties into equation (2.3) for each frequency, the response X_ω is calculated, which represents floating quay's responses to the first order wave load, exciting force/moment, at each wave frequency ω. In other words, X_ω is responses to regular wave test of wave frequency ω.

In this regard, the experimental results of regular wave tests are compared with sets of X_ω in terms of RAO as

$$RAO = \frac{X_\omega}{A_{Incident}} \tag{2.19}$$

In the comparisons of RAO's, RAO calculated by WAMIT, which is indicated as "WAMIT RAO", is plotted with three sets of experimental data: first one is linear response indicated as "Linear Response" that has same frequency of motion as frequency of incident wave, the next is nonlinear response indicated as "Nonlinear Response" that has offset between motion frequency and incident wave frequency, and the last is experimental spectrum RAO indicated as "Experiment Spectrum RAO", which is calculated from the time series of incident wave elevation and responses to the experimental irregular wave test.

Spectrum RAO is the RAO calculated from two sets of power spectrum: one is incident wave power spectrum $S_{incident}$ and the other is response power spectrum $S_{reponse}$, which are transformed from wave elevation and responses on time domain by Fast Fourier Transform (FFT), respectively;

$$SpectrumRAO = \sqrt{\frac{S_{reponse}}{S_{incident}}} \tag{2.20}$$

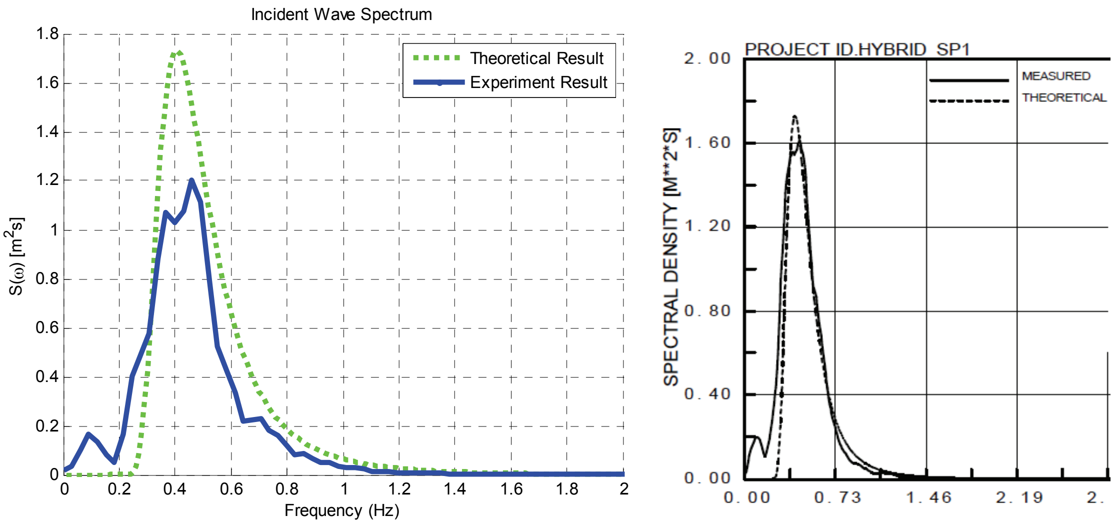

Figure 2.9 Comparison of Incident Wave Spectra in Experiment

Since power spectrum transformed from time series tends to be variant with various FFT techniques, in the present study the FFT is standardized to make identical incident wave spectrum to incident wave power spectrum given by KORDI; in Fig. 2.9 the blue line is the power spectrum transformed from wave elevation data of experiment.

The reasons that the experimental one (blue line) is different from theoretical one (green line) are, at first, the experimental wave elevation history used for FFT is data measured around floating quay, which includes noise, as an alternative to absence of exact experimental wave elevation data, and secondly the exact spectrum of incident wave given by KORDI as a figure on the right has similar trend to the blue line above: energy in low frequencies and a cave-in at peak frequency.

From Fig. 2.10, the linear/nonlinear responses of the experiments are generally matched well with WAMIT RAO. And to confirm the natural frequency between simulation and experiment, Experiment Spectrum RAO is compared with WAMIT RAO based on a viewpoint that natural frequency is usually presented by peaks in a low frequency region. The general natural frequencies of simulation show good agreement with those of experiment as well. Therefore, the first calibrating process given in Fig. 1.2 is abridged in this 2-body case.

The correspondences represent reliability of both results in numerical analysis on frequency domain and experimental results from regular/irregular wave tests. The small differences between the two result sets would be generated by four aspects: uncertainties of experimental process, filtering process to get Linear/Nonlinear Response from sets of response histories of experiments, assuming that wave is harmonic, and the absence of viscous effect. However, the differences between the numerical analysis and experiment on frequency domain seem acceptable; accordingly, the hydrodynamic properties are exported to time domain analysis with mean drift force.

In addition, focusing on the linear and nonlinear responses of experiments in 6 DOF motions almost responses shown in translational motions are linear; in the meantime, rotational motions show nonlinear responses more, which represent rotational motions are more affected by nonlinear phenomenon.

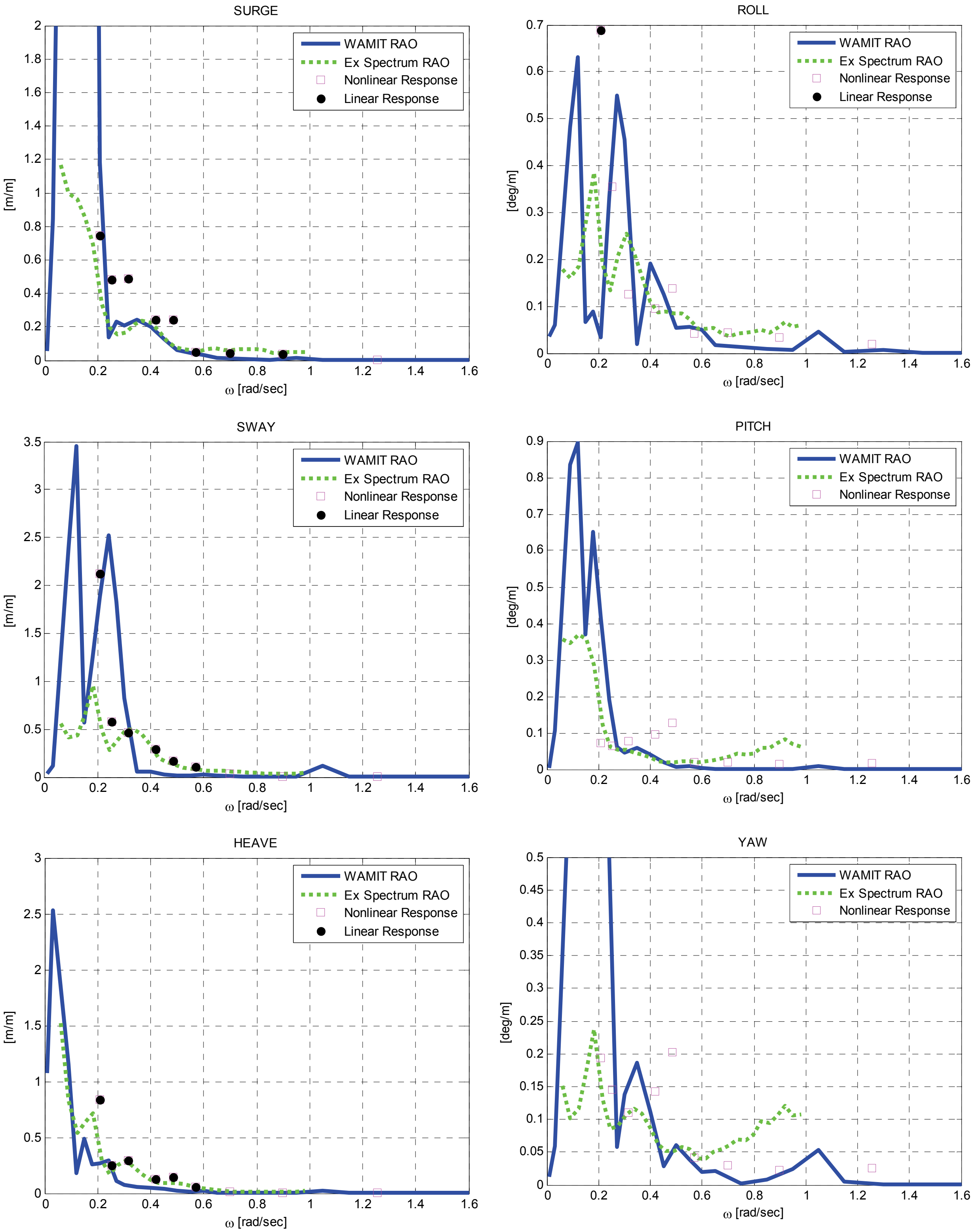

Figure 2.10 RAO Comparison of Floating Quay

2.2.6 Free Surface Elevation Comparison

As second comparative results set, free surface elevation is drawn. The measuring points are given in Fig. 2.11 as assigned in the experiment.

In experiment, free surface elevation is measured by a series of regular wave tests at each point. The measured data is filtered and averaged per frequency; afterward, the experimental results are compared with the numerical results calculated from the WAMIT on frequency domain.

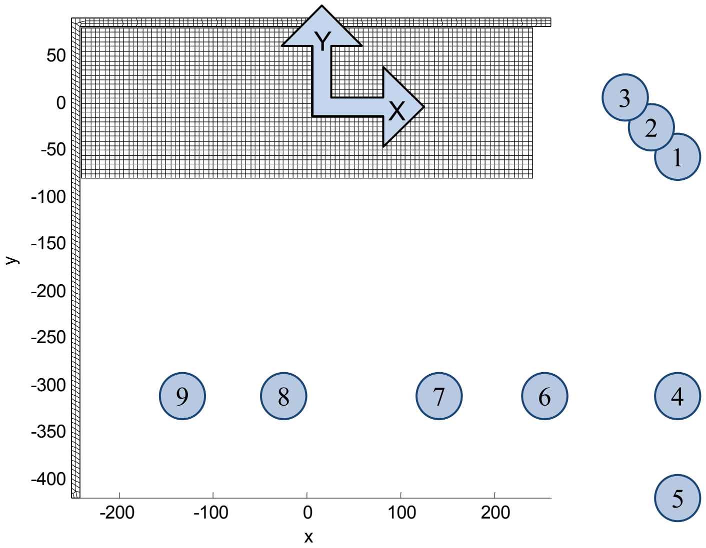

Figure 2.11 Measuring Points of Free Surface Elevation

Coordinates of the measuring points are given with respect to global coordinate system in Table 2.6.

The free surface elevation is derived from total velocity potential by dynamic free surface boundary condition;

$$\eta = -\frac{1}{g}\left(\frac{\partial \Phi_T}{\partial t}\right)_{z=0} \tag{2.21}$$

Table 2.6 Coordinates of Measuring Points

Measuring Points	*Coordinates*
1	378.7, -38.7, 0
2	343.7, -3.7, 0
3	308.7, 31.3, 0
4	358.7, -218.7, 0
5	358.7, -318.7, 0
6	158.7, -218.7, 0
7	58.7, -218.7, 0
8	-41.3, -218.7, 0
9	-141.3, -218.7, 0

The results are presented as non-dimensional wave elevation generated by unit wave amplitude in Fig. 2.12.

In the figures, blue line represents free surface elevation of ideal fluid and magenta square is the results of virtual ocean fluid expressed as Newtonian fluid with viscosity and incompressibility, theoretically. Despite the fact that the mainly different factor is viscosity in the two result sets, the trend of numerical free surface elevation along wave frequency generally shows good agreement with experimental one except for the results as measuring point #2. In the case of measuring point #2, we can expect certain erroneous of the experiment.

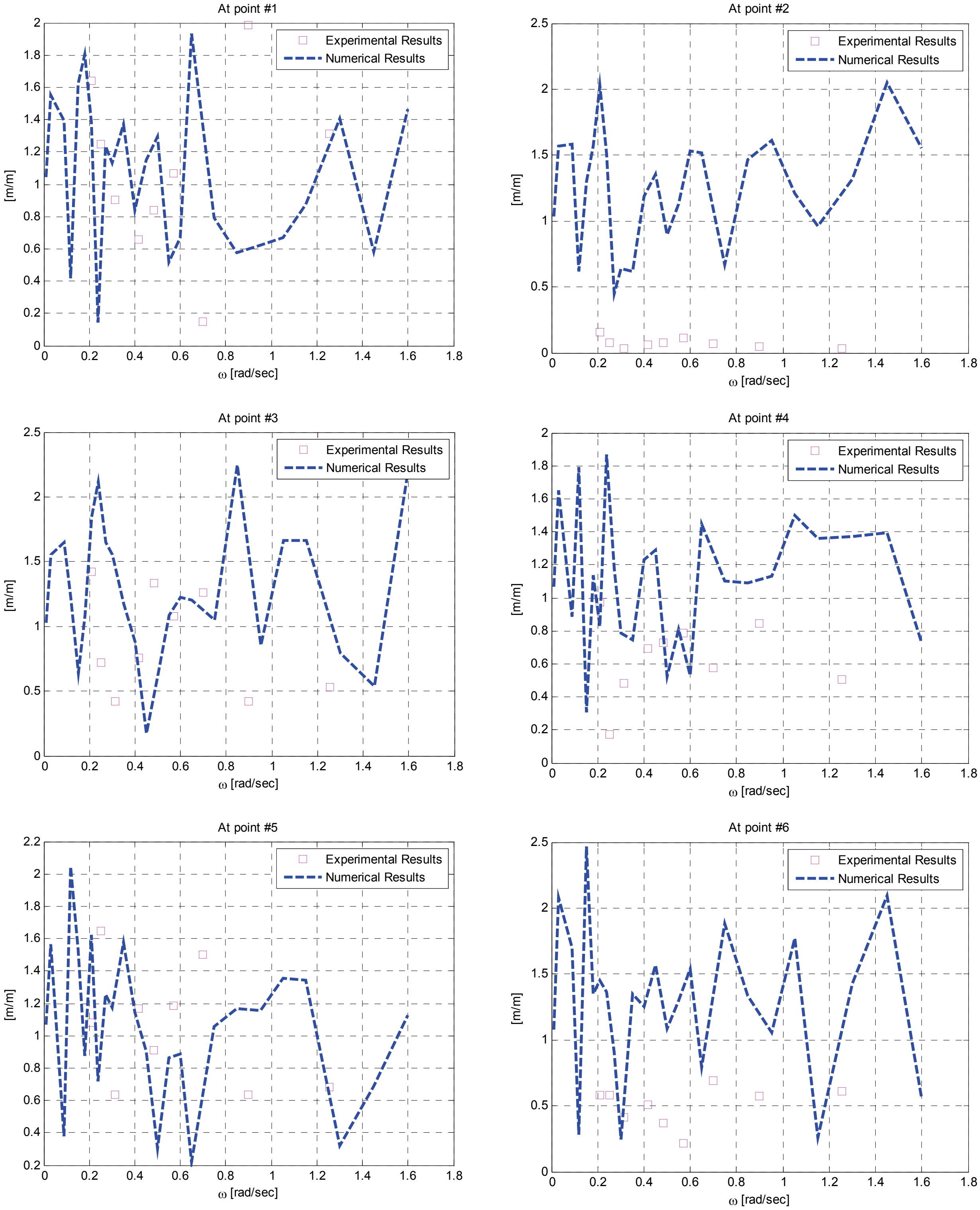

Figure 2.12 Free Surface Elevation Comparison, 2-body Case

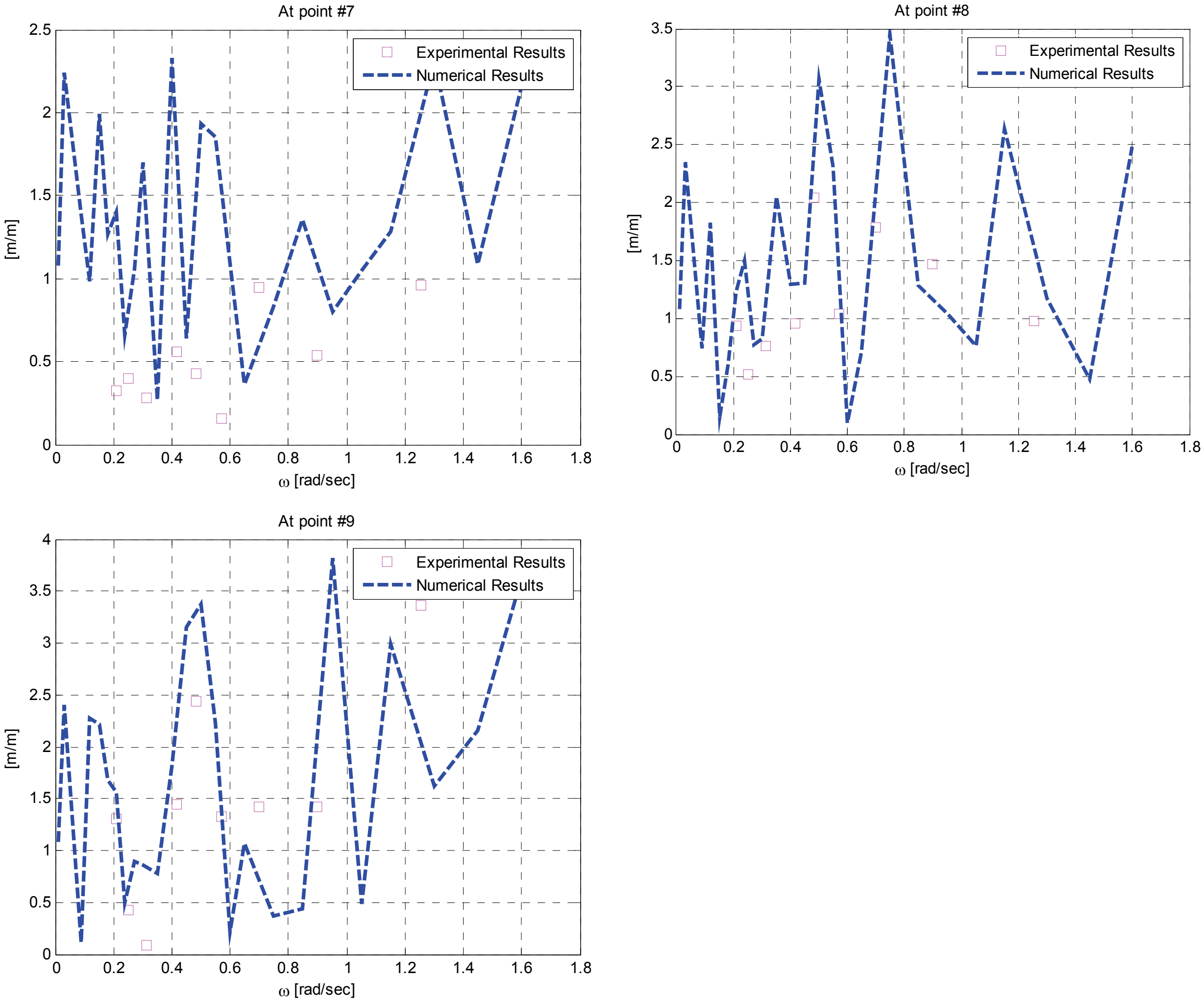

Figure 2.12 Continued

2.2.7 Alternative Modeling of Fixed Quay: Infinite Walls

In this section, an alternative to the modeling of the fixed quay is introduced. In terms of interaction between two bodies' motions, the fixed quay makes only reflected waves not radiated waves. To design such a fixed structure in numerical modeling, there are three methods using WAMIT: setting not to solve radiation velocity potential of the fixed structure, assigning extremely large mass and stiffness, and adopting infinite wall.

In the present research, two methods, the second and the third, are adopted. While the second method was used in the previous sections, the third method is given in this section to confirm the hydrodynamic properties. As the third, infinite wall option case as shown in Fig. 2.13 is implemented and the results are compared with the previous results set.

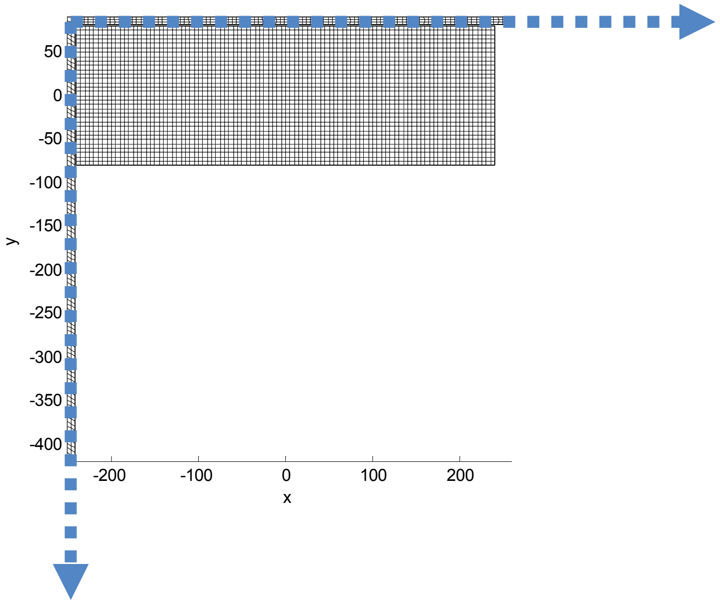

Figure 2.13 Schematic of Infinite Walls

In the infinite wall case, the floating quay is assumed to be located around two orthogonal infinite walls indicated as dotted blue arrows. Using this option in WAMIT, the two-body case is considered as single body case, and thus the advantage is reducing the computing time.

On the other hand, disadvantage is overestimated wave reflection owing to the infinitely extended walls. As a reference, a set of six hydrodynamic properties from added mass/moment of inertia to measurements of free surface elevations are compared with those of the previous two-body case as shown in Fig. 2.14 to Fig. 2.19.

In the comparisons, the unmatched peaks can be seen for all the hydrodynamic properties, which represent possible differences for resonance phenomenon for each motion.

From the relatively remarkable dissimilarities between the previous two-body case and the current single body case, the second modeling of the fixed quay is considered as the better option in this research; moreover, the second option is used for further study like time domain analysis.

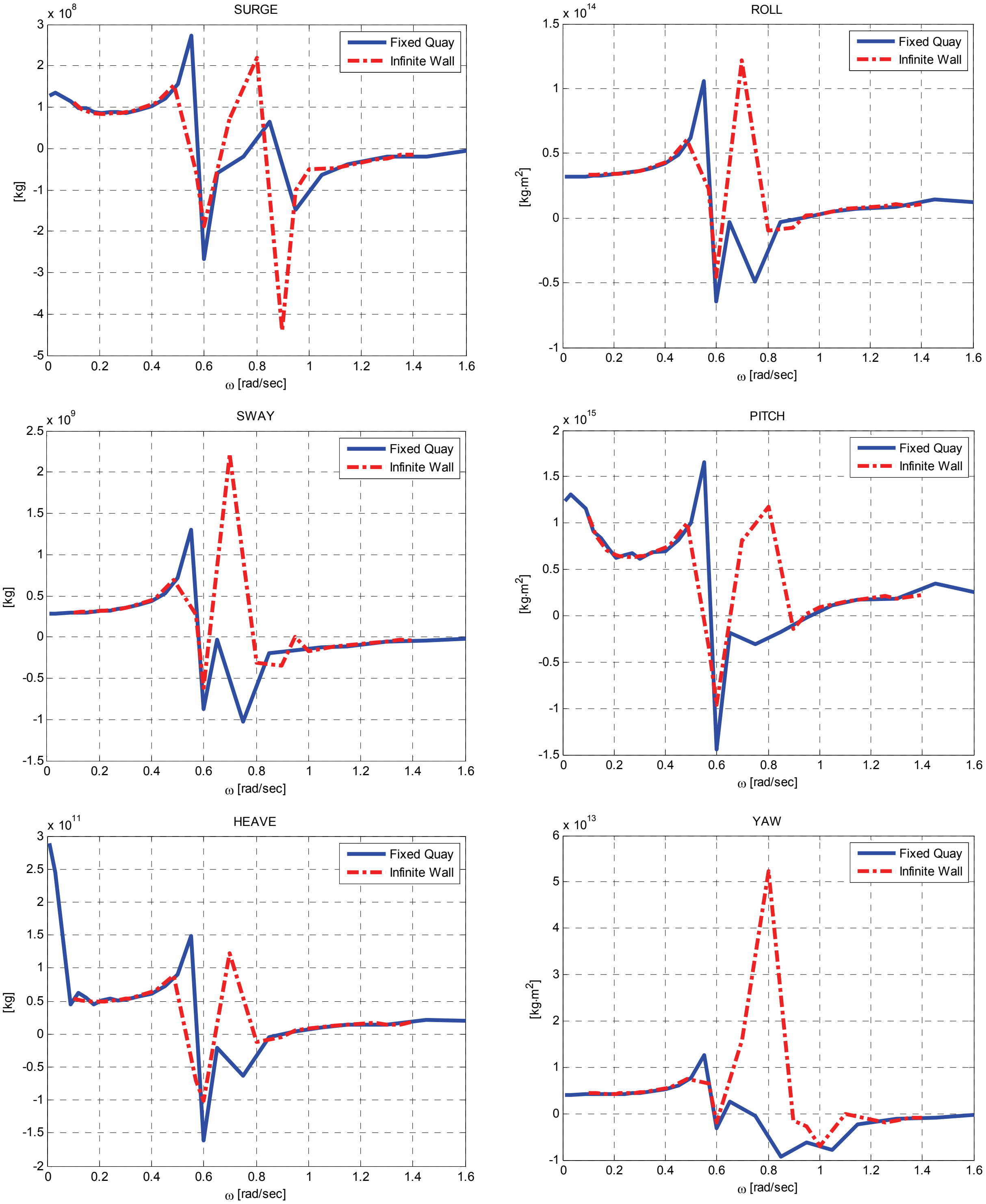

Figure 2.14 Comparison of Added Mass/Moment of Inertia

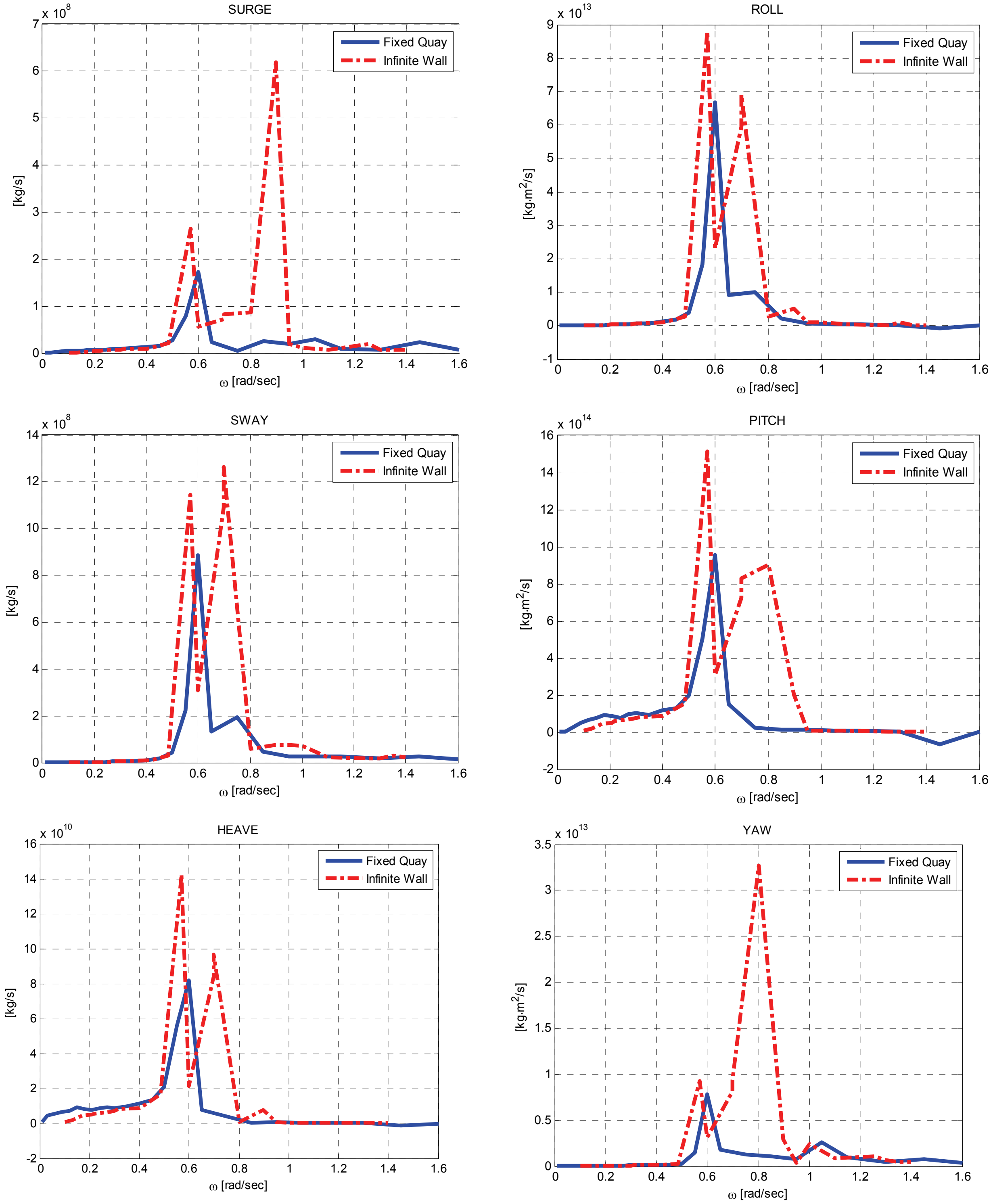

Figure 2.15 Comparison of Damping Coefficients

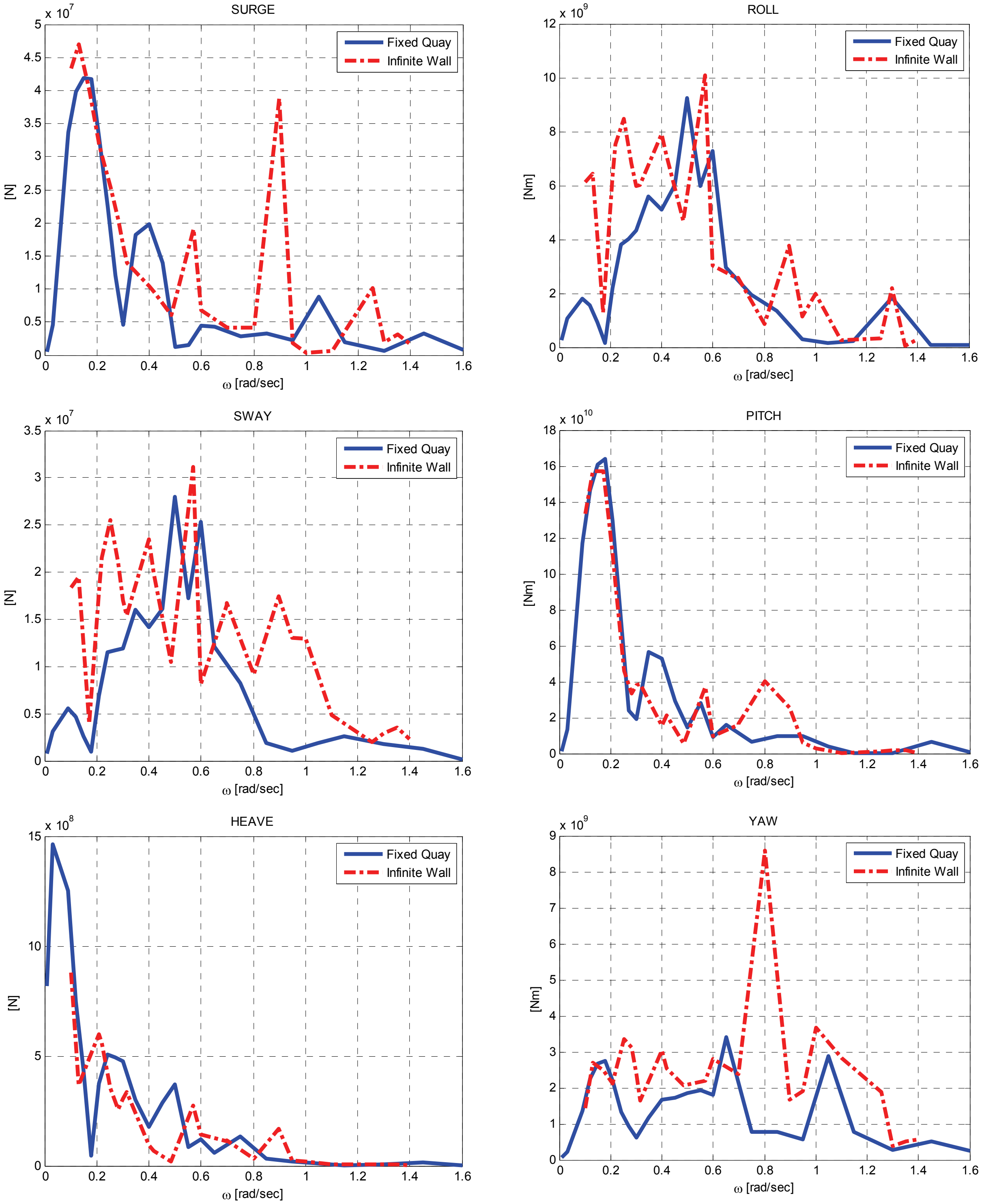

Figure 2.16 Comparison of Wave Exciting Forces/Moments

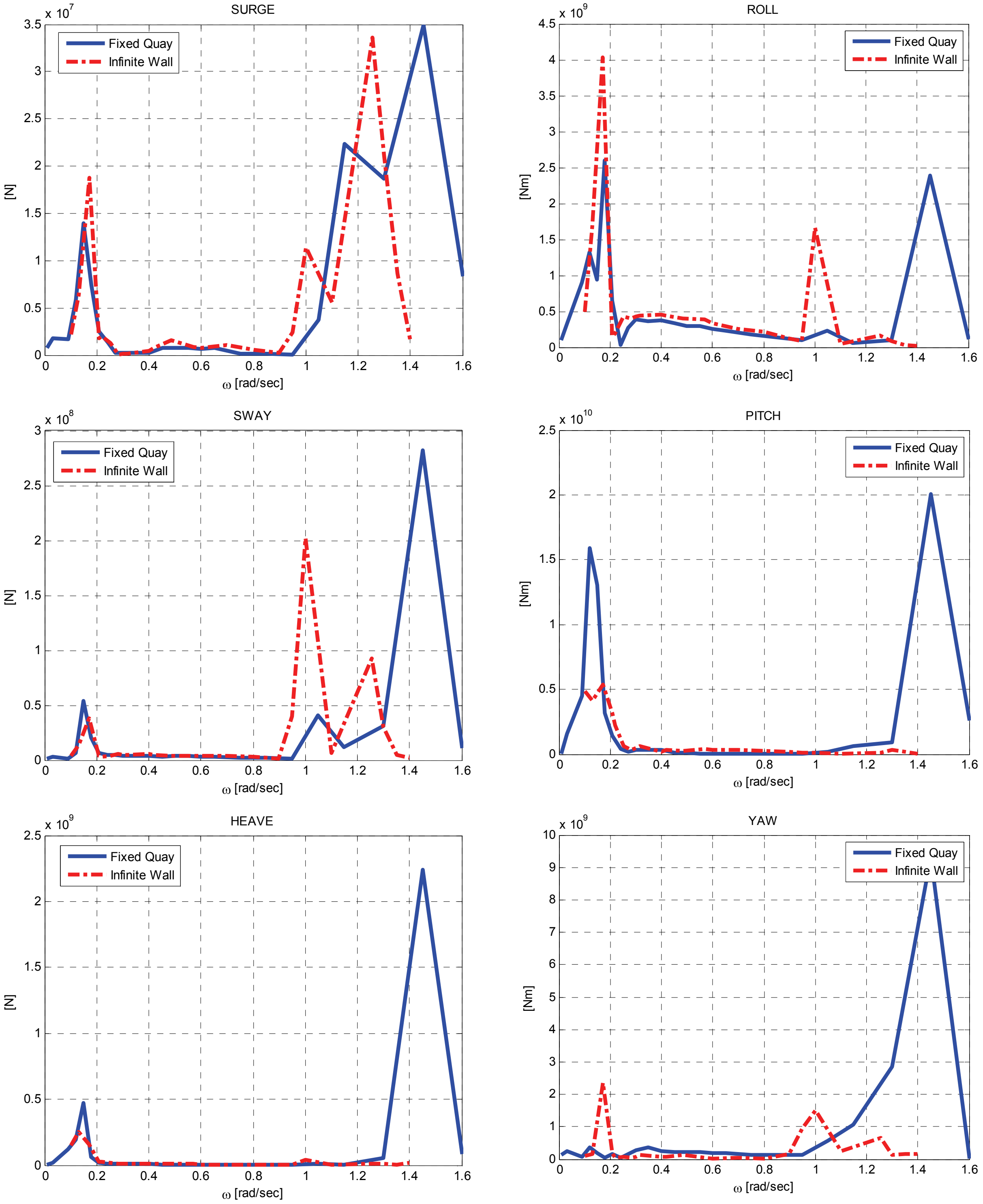

Figure 2.17 Comparison of Mean Drift Forces/Moments

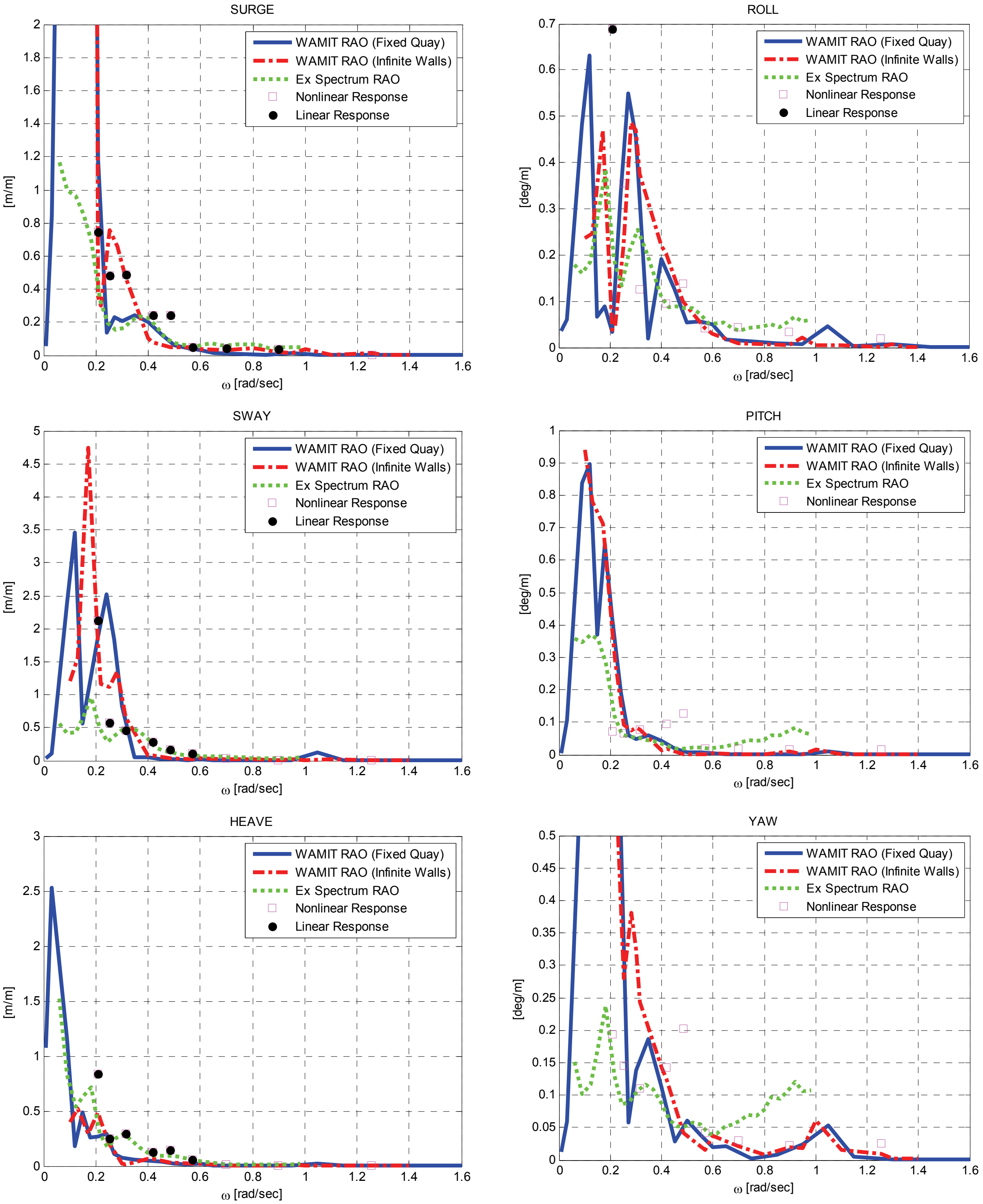

Figure 2.18 Comparison of RAO

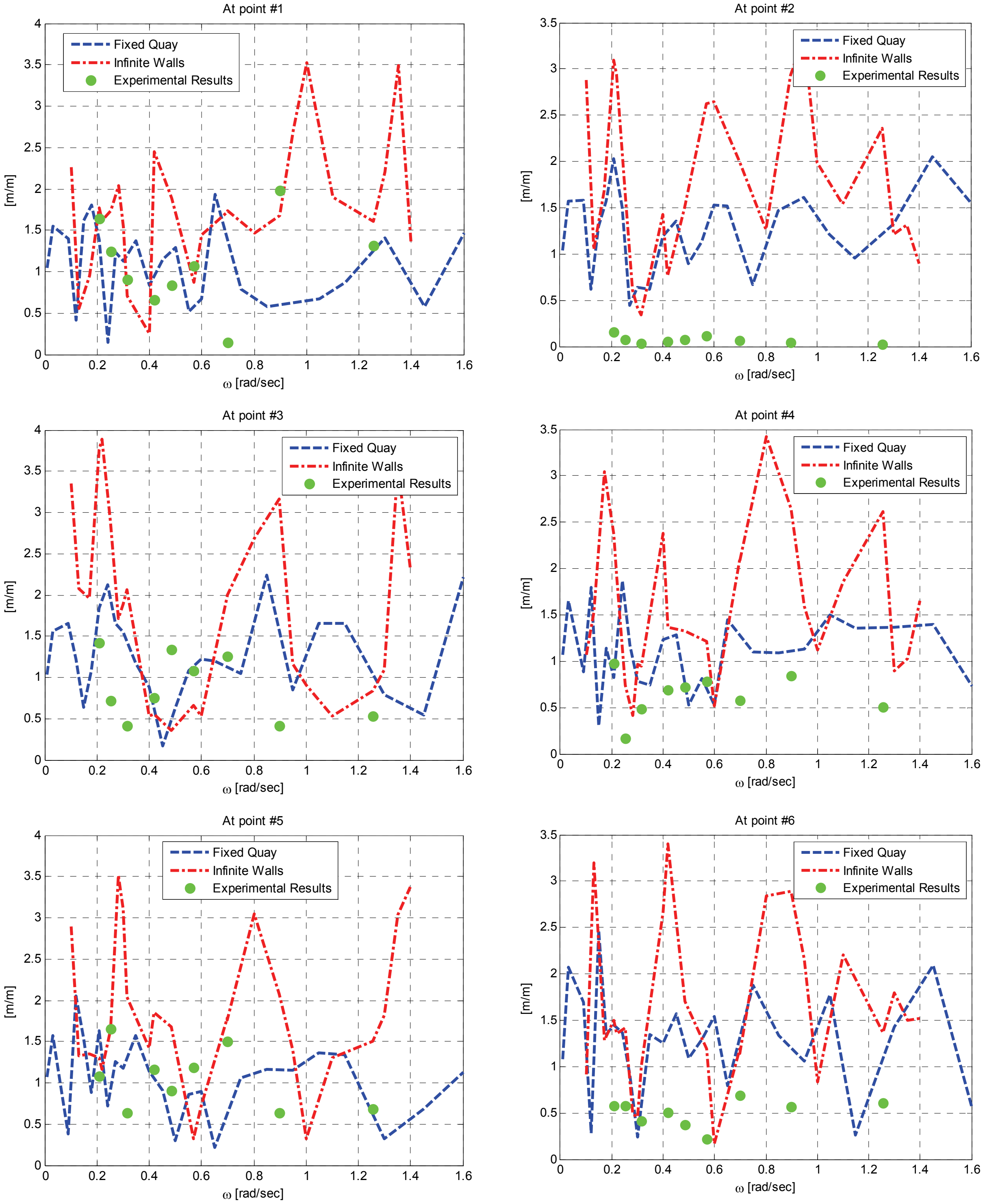

Figure 2.19 Comparison of Free Surface Elevation

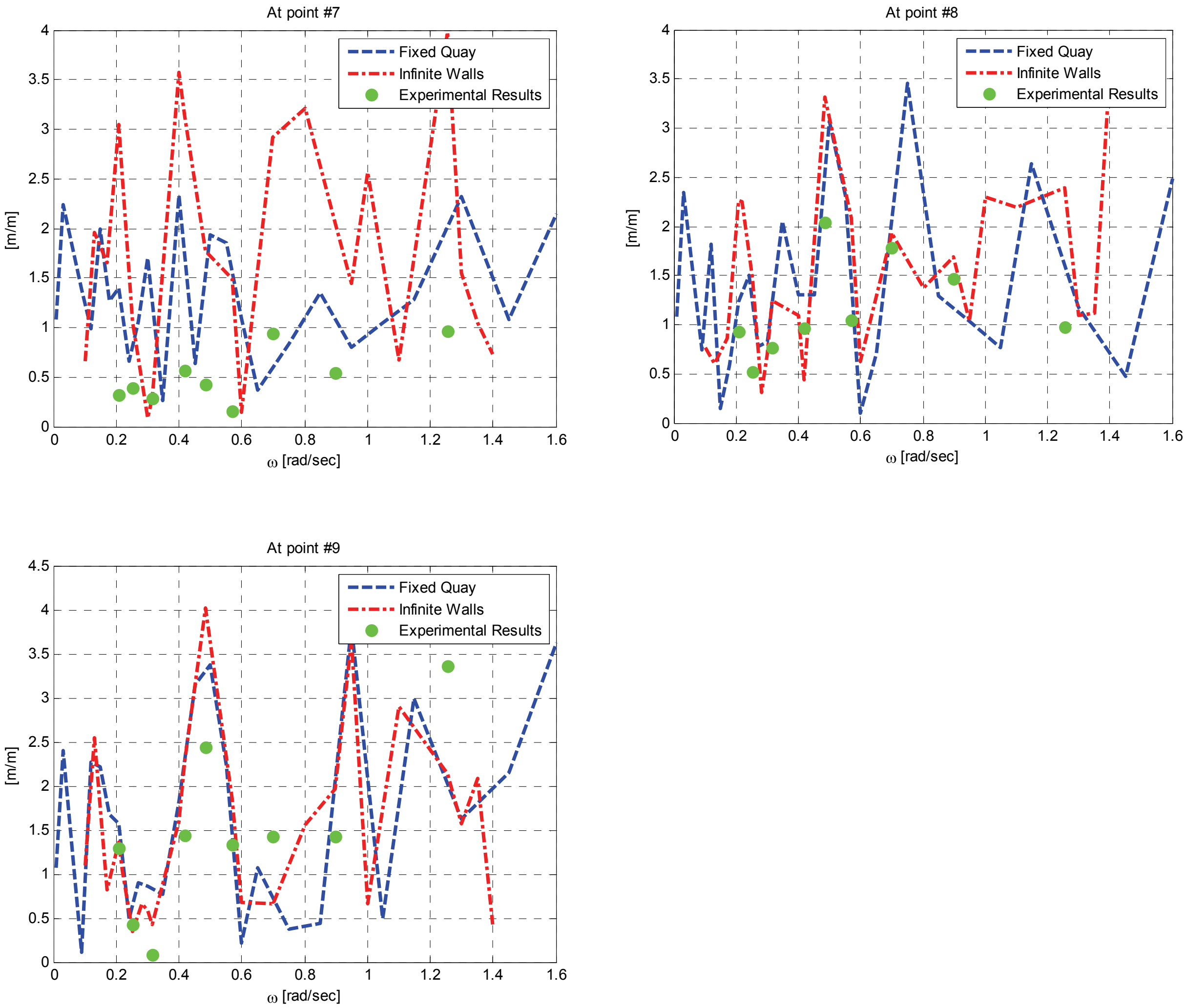

Figure 2.19 Continued

2.3 Time Domain Analysis

In time domain analysis, a regular wave test or an irregular wave test can be implemented from the results obtained in the frequency domain analysis. At first, the regular wave test can be easily carried out by substituting variable t at each step into the solution to equation (2.3); however, the irregular wave test give rise to a set of more advanced processes based on the *stokes wave theory* such that an irregular wave can be made of a series of regular waves.

From the stokes wave theory and characteristics of time domain analysis, the equation (2.3) is reformed as

$$(M + \Delta M_{\infty})\ddot{X}_t + (K_E + K_H)X_t = F_{W1_t} + F_{W2_t} + F_{Ct} + F_{Dt} \tag{2.22}$$

Briefly speaking the reformed terms, an additional wave excitation force F_{W2t}, drift force, is at first applied as mentioned in Section 2.2.4.4. To reduce the computing time, Newman's Approximation is adopted, as described in Section 2.3.1. Next, the added mass and damping coefficient terms are reformed to infinite frequency added mass ΔM_{∞} as equation (2.23), and radiation damping force F_{Ct} as equation (2.24), which includes retardation function $R(t)$, based on the *Commins Equation* (Commins 1962).

$$\begin{gathered} \Delta M_{\infty} = \Delta M(\omega_{\max}) + \int_0^{\infty} R(t)\frac{\sin(\omega_{\max})}{\omega_{\max}}dt\,, \\ where\ \ R(t) = \frac{2}{\pi}\int_0^{\infty} C_R(\omega)\cos(\omega t)d\omega \end{gathered} \tag{2.23}$$

$$F_{Ct} = -\int_{-\infty}^{t} R(t-\tau)\dot{X}(\tau)d\tau\,,$$
$$\text{where } R(t) = \frac{2}{\pi}\int_{0}^{\infty} C_R(\omega)\cos(\omega t)d\omega \tag{2.24}$$

C_R represents the radiation damping coefficients from WAMIT, and thus $R(t)$ can be referred to as the Inverse Fourier Transform of C_R. F_{Ct} represents the memory effect of fluid, and $\omega_{\max}$ is the max wave frequency of the set of regular waves used in time domain analysis to make an irregular wave.

After that, two excitation forces, exciting force and drift force, are superposed with respect to the set of wave frequencies based on the stokes wave theory;

$$F_{W1t} = \mathrm{Re}\left[\sum_{k=1}^{N} A_k L_{W1}(\omega)e^{i\omega_k t}\right]$$
$$F_{W2t} = \mathrm{Re}\left[\sum_{j=1}^{N}\sum_{k=1}^{N} A_j A_k^{*} Q_{W2}(\omega_j,\omega_k)e^{i(\omega_j-\omega_k)t}\right] \tag{2.25}$$

At this step, notice is that the sum frequency second order force is omitted since the effect is negligible except for a TLP case. A presents an amplitude of the wave at each frequency, and A^{*} represents the complex conjugate. $L_{W1}(\omega)$ and $Q_{W2}(\omega)$ are the complex value of the wave exciting force and the drift force at each wave frequency, respectively.

As the last of the reformed components, nonlinear drag force F_{Dt} is applied into the system to account for the various effects of viscosity and energy dissipation, which are not easy to clarify analytically, as described in Section (2.3.2). In addition, K_{Total}, sum of the external stiffness K_E and hydrostatic stiffness K_H, represents one of the *Total Dynamic Information* shown in Fig. 1.2. K_H is calculated from WAMIT and it is a set of static stiffness for heave, roll, and pitch motions, which are dominantly affected by the gravity. We can also categorize the external mass matrix also into the *Total Dynamic Information*. Shortly, the external dynamic information with the K_H is presented as *Total Dynamic Information* in the present study.

Finally, to solve the equation (2.22) at each step, two schemes, Adams-Moulton scheme and Adams-Bashfort scheme, are used in CHARM3D (Ran, 2000).

2.3.1 Second Order Wave Force

As mentioned in the previous sections about mean drift, the second order wave forces, drift force and springing force, are usually applied to the system to get more accurate responses in terms of resonance. And in this study, only drift force is applied to the system.

Considering methods to calculate the drift force, there exists three ways to calculate the drift force; first one is solving second order velocity potential problem to get complete formula of the drift force, the next is calculating it without a term of integral along free surface in the complete formula, and the third one is using an approximate method such that the drift force is calculated directly from mean drift force using Newman's approximation as equation (2.26).

$$Q_{W2}(\omega_i, \omega_j) = Q_{W2}(\omega_j, \omega_i) = \frac{1}{2}\left(Q_{W2}(\omega_i, \omega_i) + Q_{W2}(\omega_j, \omega_j)\right) \tag{2.26}$$

$Q_{W2}(\omega_i, \omega_i)$ is the mean drift force at frequency ω_i. The drift force by ω_i and ω_j $Q_{W2}(\omega_i, \omega_j)$ can be referred to as an averaged mean drift force of $Q_{W2}(\omega_i, \omega_i)$ and $Q_{W2}(\omega_j, \omega_j)$.

In comparison of three methods above, first one is the most accurate especially at scale. However, in terms of demanding time to calculate and importance to identify drift force with respect to frequency the third approximated method is adopted in this research.

2.3.2 Drag Plate Information

As mentioned in Section 2.2, one of the most different characters between ideal fluid and real ocean flow is viscosity. To account for the viscosity effect, Morison formula's damping force term F_D is taken up;

$$F_D = \frac{1}{2}\rho A C_D U|U| \tag{2.27}$$

ρ is water density, A is projected area with respect to the plane of motion direction; for instance, to input F_D for surge motion, A is projected area of an object to y-z plane. C_D is drag coefficient, and U is relative velocity of fluid.

Before input of viscous effect, there is one point to be recognized. In various characters of fluid, viscous effect is one of the most difficult things to figure out accurately by analytical method. In this regard, a set of experiments is in general conducted, and corresponding simulations are carried out and compared with the experiments as one of design processes for a floating structure or system. Thus, in the present study viscous effect is estimated in terms of “damping force F_D” by response comparison on time domain between CHARM3D and experimental results, which is the process indicated as *Calibration II* in Fig. 1.2.

Using CHARM3D in time domain analysis, A and C_D are supposed to be input by user. In this case, F_D is adopted for surge and sway motions of the floating quay, and A is input as shown in Fig. 2.20; C_D is input as 2 as an initial value of the second calibration. Since the fixed quay is assumed to be immovable, there is no input for the damping force of the fixed quay. Moreover, as mentioned above damping force is estimated based on the comparison of response histories; for example, if certain responses of simulation are larger than those of experiments, the damping forces of the relevant motions get increased. For the equation (2.27), inputs are given in Table 2.7.

(a) Drag plates to x-z plane for sway

(b) Drag plates to y-z plane for surge

Figure 2.20 Drag Plates of Floating Quay

Table 2.7 Drag Plate Information of Floating Quay

Plate number	$\frac{1}{2}\rho A C_D$	*Center Coordinates of each drag plate*	*Unit Normal Vector*
1	738000	-180, 0, -3	0, 1, 0
2	738000	-60, 0, -3	0, 1, 0
3	738000	60, 0, -3	0, 1, 0
4	738000	180, 0, -3	0, 1, 0
5	984000	0, 0, -3	1, 0, 0

2.3.3 Sea State

In this section, a set of information for sea state is defined to specify incident wave conditions and extra environmental conditions. At first, incident wave frequencies and heights are assigned in terms of a type of wave spectrum, a significant wave height, and a peak period with a certain wave frequency region. After that, extra environmental conditions like current, wind force are specified. All the sea state conditions are based on the experimental irregular wave test.

From the sea state information given by the KORDI, the sea state is assigned as Table 2.8; since the KORDI conducted only one test of irregular incident wave, which is severe sea state condition to examine the survivability, the simulation also take up the only one sea state at this step.

Table 2.8 Sea State Conditions of 2-body Case

Sea state	*Identified Values*
Wave Spectrum Type	Bretschneider-Mitsuyatsu Spectrum
Significant Wave Height (H_S) [m]	2.8
Peak Period (T_P) [sec]	15.5
Wave Frequency Region [rad/sec]	0.25 ~ 1.5
The Number of Incident Waves	126

The sea state inputs are identical to those of experiment except for the wave frequency region. Owing to the unclear data about the region of incident wave frequency, we assumed that the minimum frequency is 0.25 rad/sec.

For the extra environmental conditions, there is no current, but wind force is applied as a pair of static forces as shown in Fig. 2.21; the experiments had been carried out in a indoor three dimensional shallow water tank,

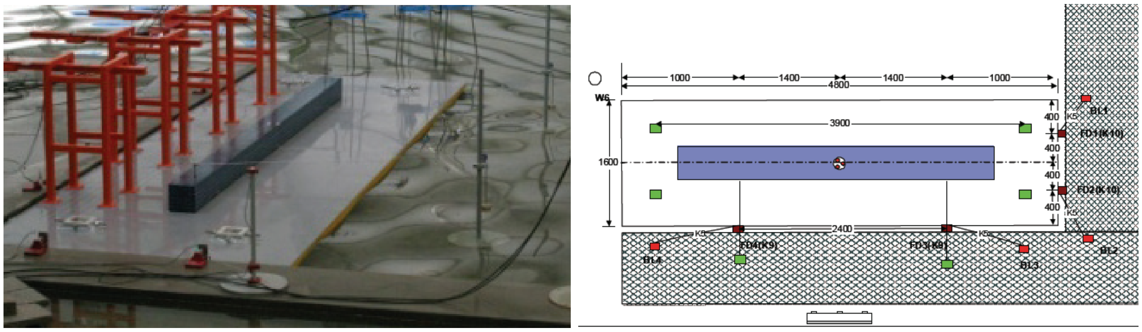

Figure 2.21 Static Wind Force in Experiment

The exquipment of static wind force is presented as a weight connected to floating quay by a line through a pulley as shown on the left picture in Fig. 2.21; in addition, it is indicated as green box on the fixed quay of the right figure.

The force magitude is given as 17032400N and the height of the line's connection point on the fixed quay is assumed as 20 m. Considering coupled effect in 6 DOF motions by the static force, static force of sway and static moment of roll are input as Table 2.9.

Table 2.9 Effects of Static Wind

Motion	*External Static Force/Moment*
Sway [N]	17032400
Roll [Nm]	-340648000

2.3.4 Response History Comparison

Using CHARM3D, an irregular wave test of numerical analysis on time domain is conducted based on the equation (2.22) and the sea state conditions.

As results of the irregular test simulation, response histories of 6 DOF motions, surge, sway, heave, roll, pitch, and yaw, of the floating quay are obtained. Time domain analysis is implemented for about 1hour 40mins, and time interval is assigned as 0.05sec.

Before the comparison of irregular test wave results, a checking process should be carried out to examine reliability of the whole process of the numerical analysis. From a characteristic between frequency domain analysis and time domain analysis, the responses to time domain analysis are Inverse Fourier Transform (IFT) of those to frequency domain analysis; conversely, the responses to frequency domain analysis are the Fourier Transform of those to time domain analysis.

Thus, the time domain results are compared with the frequency domain results in terms of *Spectrum RAO* described in Section 2.2.5 by FFT.

2.3.4.1 Confirmation of Time Domain Results

To examine feasibility of time domain results, CHARM3D Spectrum RAO is compared with WAMIT RAO in Fig. 2.23; CHARM3D Spectrum RAO is the results of FFT from the responses to the irregular wave test using CHARM3D, and indicated as CHARM3D RAO in the figures. The irregular wave test should have certain conditions identical to WAMIT’s linear motion equation such that the excitation force is only wave exciting force, and there is no viscous effect.

As described in Section 2.2.5, the FFT is standardized with reference to comparison of incident wave spectrums such that the theoretical wave spectrum and CHARM3D wave spectrum should be matched each other, because the wave elevation history is IFT of the theoretical wave spectrum. The comparison is shown in Fig. 2.22; the CHARM3D Spectrum RAO is obtained from 0.1 rad/sec to 1.0 rad/sec since the incident wave energy, a denominator in the formula of the spectrum RAO, is close to zero out of the region. From Fig. 2.23, we can see the correspondence between CHARM3D Spectrum RAO and WAMIT RAO, which represents the reliability of the time domain analysis using CHARM3D.

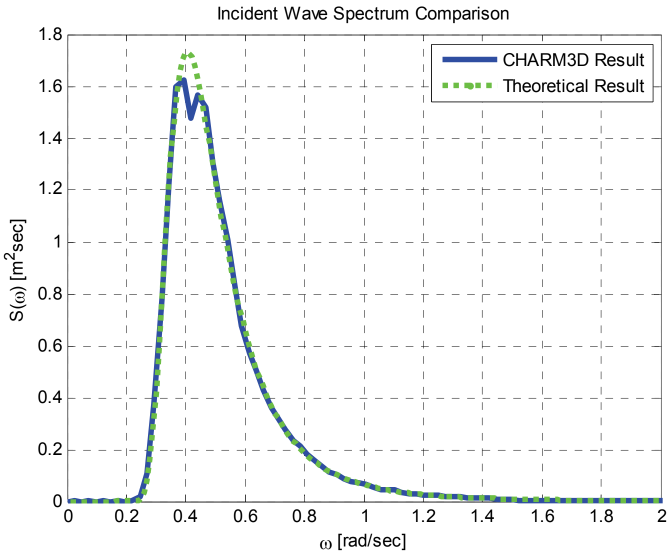

Figure 2.22 Comparison of Incident Wave Spectra in Simulation, 2-body Case

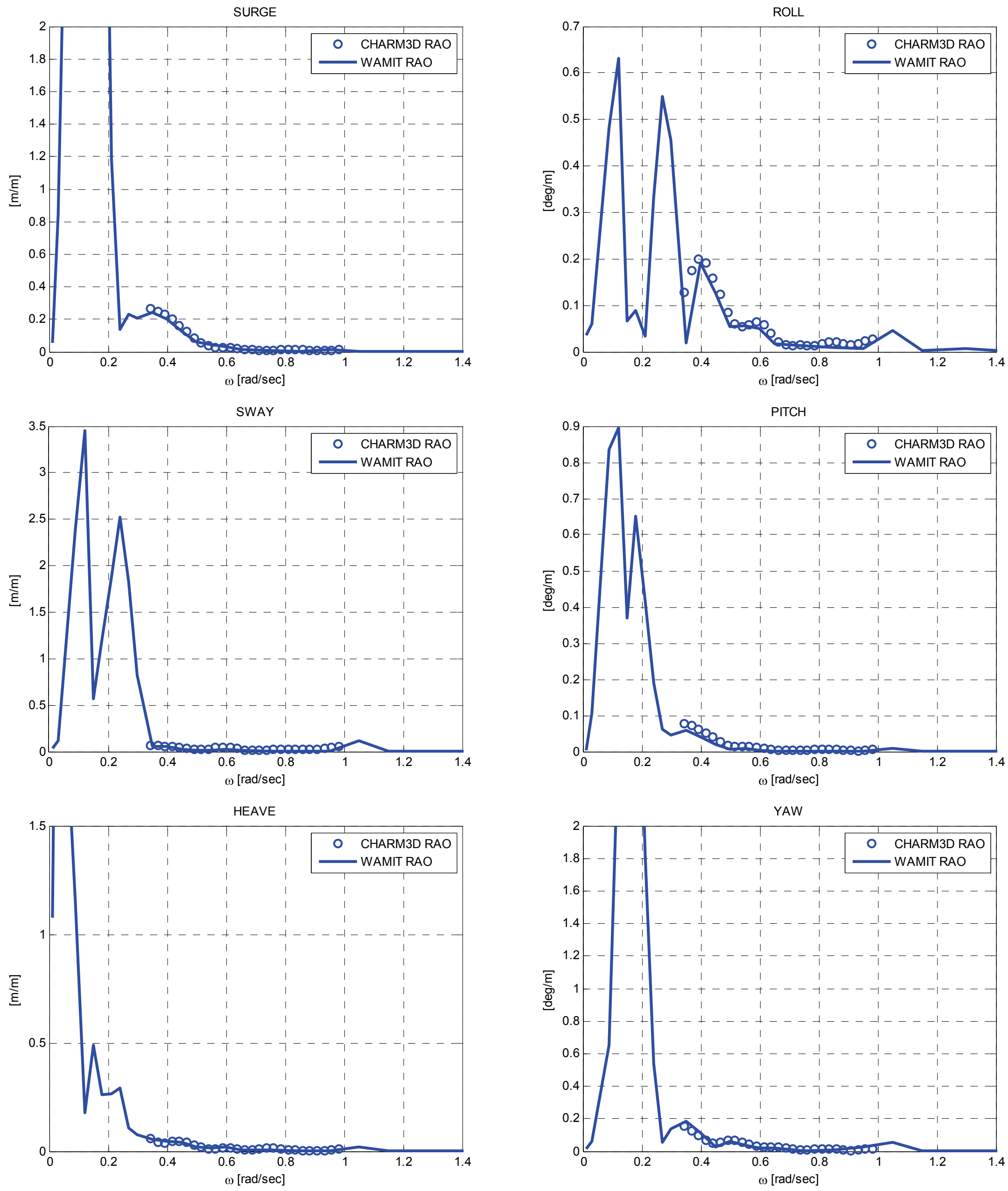

Figure 2.23 RAO Comparison between Time Domain and Frequency Domain, 2-body Case

2.3.4.2 Comparison of Responses with Experiment

As a prerequisite for comparison between experiment and simulation, it is required to identify coordinate systems between them.

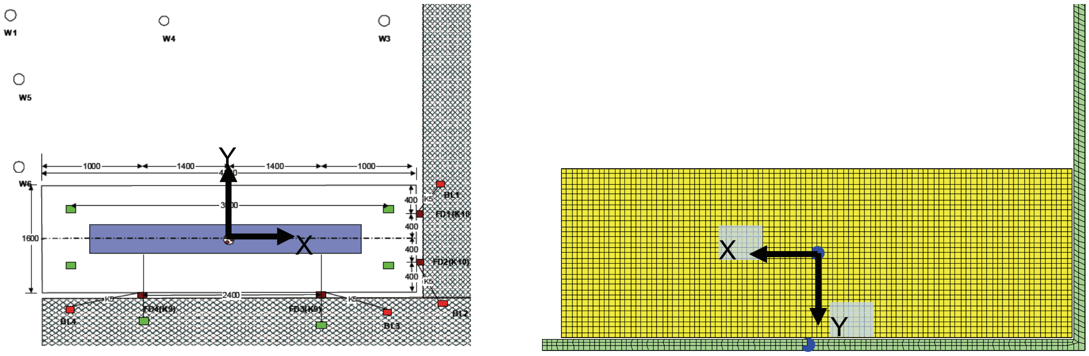

Figure 2.24 Coordinate System Comparison between Experiment and Simulation, 2-body Case

From Fig. 2.24 experimental coordinate system has opposite x and y axis and the origins are placed at an identical horizontal position. Meanwhile, numerical modeling places origins of each body coordinate system on mean water line, but experimental body coordinate system is placed on the origin at center of gravity.

In the present study, the coordinate system of experiment is transformed to that of simulation; consequently, a couple of coordinate transformations are processed as follows;

$$\begin{bmatrix} X_1 \\ Y_1 \\ \theta_{X1} \\ \theta_{Y1} \end{bmatrix} = \begin{bmatrix} -x \\ -y \\ -\theta_x \\ -\theta_y \end{bmatrix} \tag{2.28}$$

$(x, y, z, \theta_x, \theta_y, \theta_z)$ represents original coordinate system of experiment, and directions of x and y axis are changed at first; not only for surge and sway signs but also signs of roll and pitch are changed by right-hand rule.

For the difference of z coordinate, transformation of translational motions is required owing to a coupled motion; for instance, sway and heave coordinates are changed by roll motion, and surge and heave coordinates are changed by pitch motion as shown in Fig. 2.25.

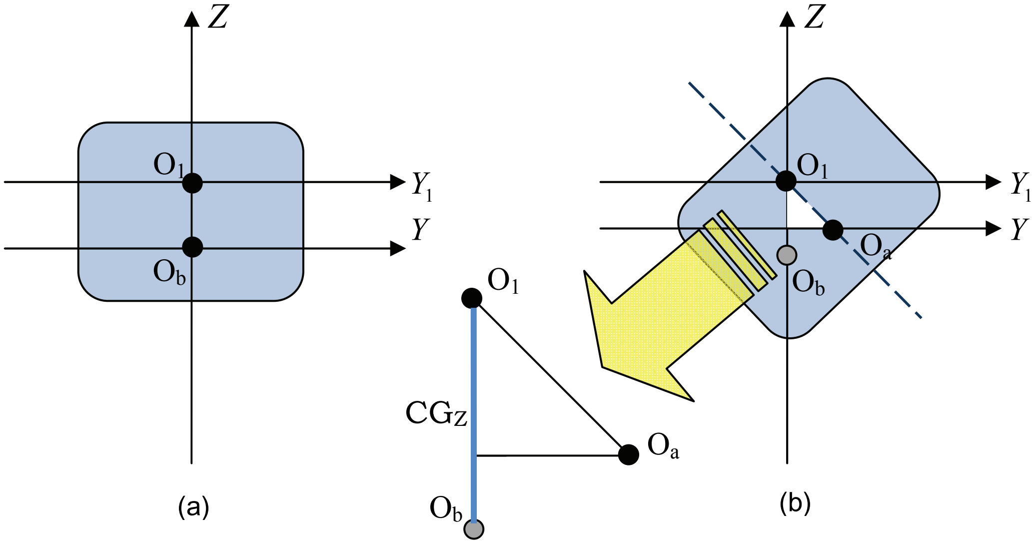

Figure 2.25 Coordinate Transformation for Roll motion: (a) before roll (b) after roll

Consider the origin of the experiment as “O_1” and that of simulation as “O_b” before roll motion. And “O_a” indicates the moved origin of simulation after roll motion “θ_{X1}”, which is the roll angle with respect to experimental coordinate system.

The distance between two origins O_1 and O_b is the z coordinate of center of gravity (CG_Z) with respect to O_b, and the rolling moves the O_b to O_a, which gives rise to additional positive surge and heave displacements of the simulation's origin, as described by an enlarged triangle figure above. In the meantime, the roll angle is invariant.

For pitch motion, the additional displacements of surge and heave are influenced; the positive pitch motion come with the negative displacement of surge and positive displacement of heave according to the right-hand rule.

Thus, the second coordinate transformation is given by

$$\begin{bmatrix} X \\ Y \\ Z \\ \theta_X \\ \theta_Y \\ \theta_Z \end{bmatrix} = \begin{bmatrix} X_1 - CG_Z \cdot \sin(\theta_{Y1}) \\ Y_1 + CG_Z \cdot \sin(\theta_{X1}) \\ Z_1 + CG_Z \cdot \left[2 - \cos(\theta_{X1}) - \cos(\theta_{Y1})\right] \\ \theta_{X1} \\ \theta_{Y1} \\ \theta_{Z1} \end{bmatrix} \tag{2.29}$$

The converted results of experiment, which are displacements with respect to the body coordinate system of simulation, presented in Fig. 2.26.

After the identification of the body coordinate system, CHARM3D responses histories are compared with the experimental results in Fig. 2.27.

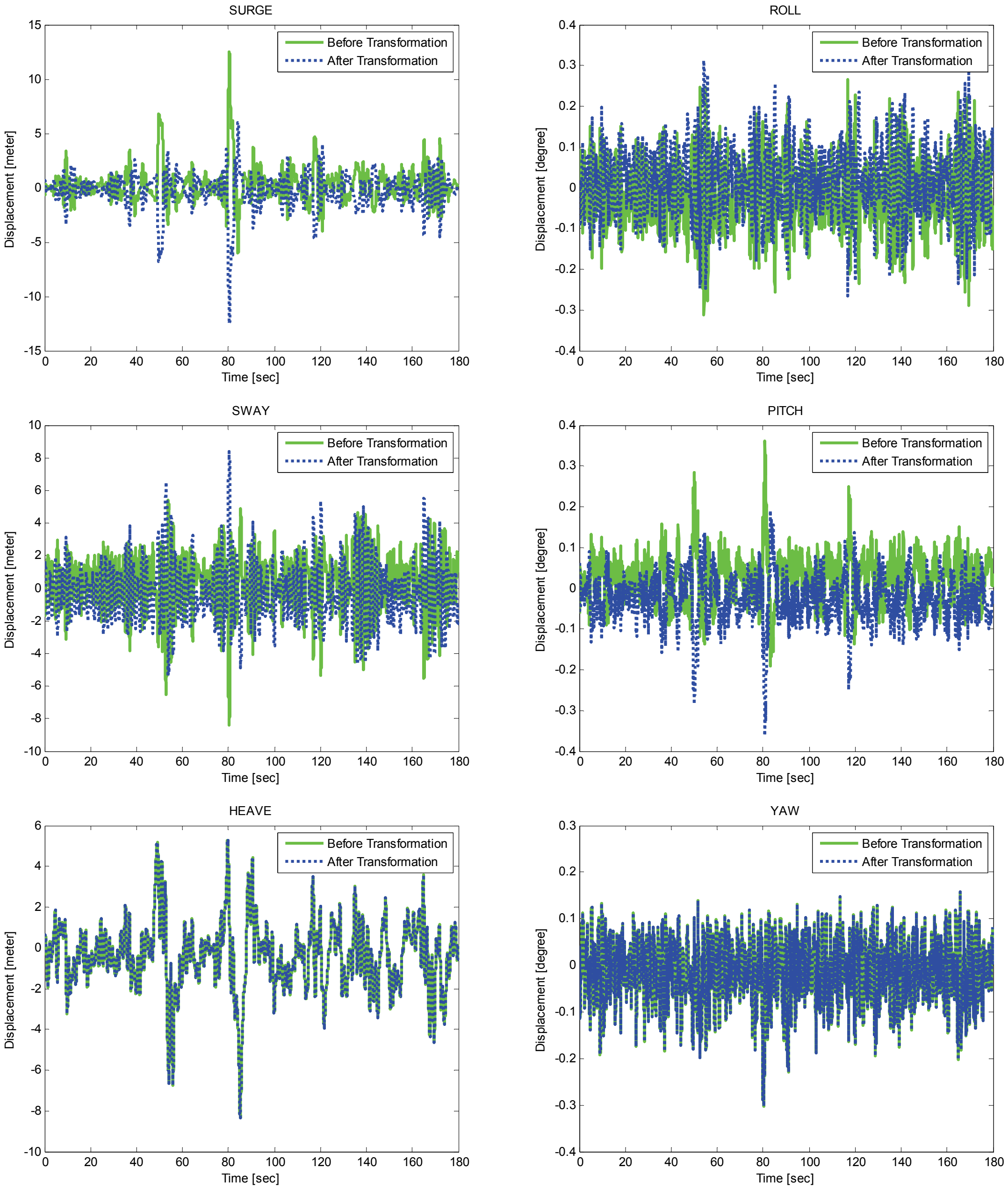

Figure 2.26 Floating Quay's Responses of Experiment after Coordinate Transformation, 2-body Case

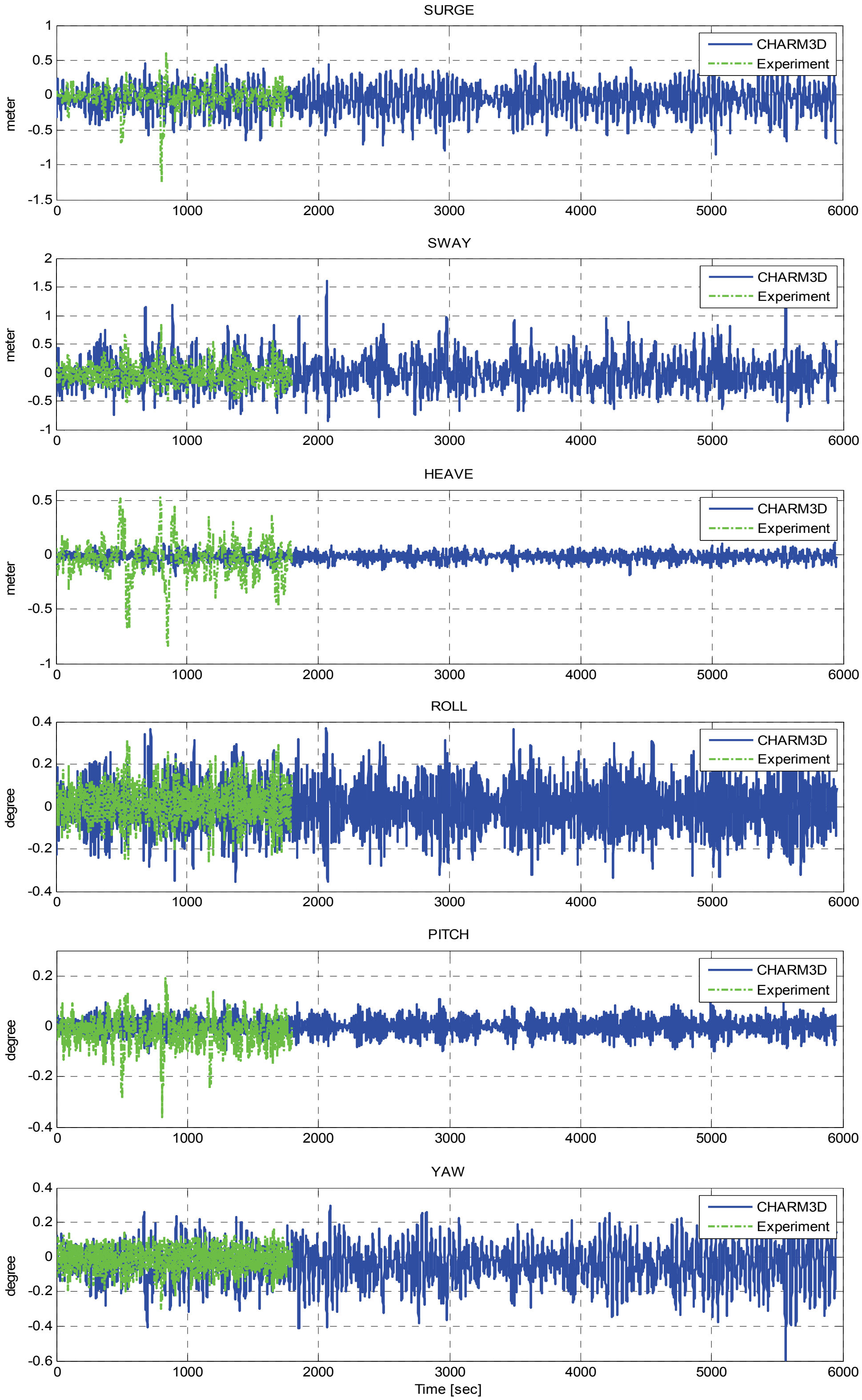

Figure 2.27 Comparison of Response Histories for Floating Quay, 2-body Case

From the comparison of response histories, the motions such as surge, sway, and yaw, which have dominant effects of the horizontal external stiffness, present slightly overestimated simulation responses as much as about one tenth larger than responses of the experiment. It is largely due to the underestimated damping forces/moments given as $C_D = 2$ for surge and sway directions. According to a research about a floating structure next to a wall by Buchner, the effects of damping force in this case are increased than a single body case (Buchner et al. 2004).

For roll motion, the response of the simulation is also a little bit overestimated; this is a well-known phenomenon of general numerical analysis caused by underestimated roll radiation damping.

Thus, to account for larger effects of damping force/moment for surge, sway, and roll motions, the damping force/moment are revised in the next section.

In the meantime, the heave and pitch motions have opposite responses to other motions such that the responses of the simulation are underestimated. Based on the fact that the motions are dominantly affected by the hydrostatic stiffness, the motions are not dependent the external stiffness, which is a variable of natural frequency and main factor to determine the dynamics. In other words, the motions are generally invariant with numerical modeling. Thus, it would be rational to expect that there are uncertain differences between experiment and simulation such as measuring process or unexpected disturbance in the experiment.

2.3.4.3 Calibration II: Damping Force Estimation

At this point, the second calibrating process is implemented, as described in Fig. 1.2. From the schematic of this two-body case, the present system has remarkably narrow gap, 1.3m, with two vertical walls in 18m-depth shallow water; therefore, the effects of damping force/moment are increased by effects from the narrow gap and shallow water depth.

To account for the increased damping effects, the C_D of surge and sway of the floating quay is amplified to 6 as summarized in Table 2.10.

Table 2.10 Calibration of Damping Force Inputs; Floating Quay

Plate number	$\frac{1}{2}\rho A C_D$, $C_D = 2$	$\frac{1}{2}\rho A C_D$, $C_D = 6$
1	984000	2952000
2	738000	2214000
3	738000	2214000
4	738000	2214000
5	738000	2214000

And to solve the overestimated roll motion, linear roll damping coefficient is applied to the system.

The linear roll damping coefficient C_L is given by a certain percentage α of critical roll damping coefficient C_{cri}. And the damping force F_D is calculated by

$$F_D = C_L \cdot U = \frac{\alpha}{100} \cdot C_{cri} \cdot U, \quad where \quad C_{cri} = 2\omega_{roll}(I_{roll} + \Delta I_{roll}) \tag{2.30}$$

The damping force is calculated by multiplying the angular velocity of the roll U by C_L. And the sum of mass moment of inertia I_{roll} and added moment of inertia ΔI_{roll} for the roll motion represents virtual mass moment of inertia. Using CHARM3D, the α and natural frequency of roll ω_{roll} are supposed to be input as shown in Table 2.11; the ω_{roll} is obtained from the RAO comparison from a viewpoint of that the ω_{roll} is a peak of the two peaks, which is not coincide with the peak frequency of sway in the roll RAO comparison.

Table 2.11 Roll Damping Coefficient; Floating Quay

α	ω_{roll} [rad/sec]
5%	0.38

With the damping inputs revised, the irregular wave test is newly carried out, and the responses are given in Fig. 2.28 and Fig. 2.29. And statistic comparison of the responses is obtained as shown in Table 2.12 by three rows of each motion: the first row is for the results from the initial damping coefficients, the next is for the results from the revised damping coefficients, and the final is for the results of the experiment. In addition, total RAO comparison, which includes the CHARM3D RAO updated after the damping revision, are plotted in Fig. 2.30.

From the figures of comparison and statistics, the responses are somewhat decreased and closer to those of the experiment after the revision of the damping coefficients. Not only surge, sway, and roll, but also the other motions are also influenced by coupling effects between the motions.

In addition, the sway motion of the simulation is generally overestimated than the experiment because of a difference of mooring system design; in the simulation, the mooring system is designed as simple linear springs while the experiment applied real fenders directly contacted to the two bodies. Thus, in experiment, we can expect there exist more energy dissipations than the simulation if the floating quay has large sway response; for example, deformation of contacted surface on the two bodies or various frictions on the fenders. Therefore, the sway motion of the simulations shows larger response than the experiment, and it can be considered that the larger response of the simulation would be altered to the energy dissipation if the real fender system is adopted.

Finally, considering limits of each motion response, the critical values are given by the KORDI: 0.48 meter for surge and sway motions, 0.8 meter for heave motion, 3 degree for roll motion, and 1 degree for pitch and yaw motions. The values for surge and sway are critical values to be in elastic region of the fenders. The other values are referred from the reference for motions of very large structures based on Japan's rules. From Fig. 2.28 and Fig. 2.29, surge and sway are out of the limit not only for experiment but for simulation. For heave motion, there is a peak out of the limit around 800 sec in the response of the experiment. The responses of the other motions, roll, pitch and yaw, are even smaller than the limit in both of the experiment and simulation. The main reason that there are certain values over the limit is that the sea state condition is severe sea state to examine the survivability not operability.

To conclude, in the severe sea state condition the two-body system can be out of the region that fenders act elastically in terms of surge and sway motions, but the other motions can be considered as safe despite the severe sea state.

Table 2.12 Statistics of Responses; Floating Quay, 2-Body Case

Motion	*Mean*	*Root mean square*	*Standard deviation*	*Max*	*Min*
Surge [m]	-0.06111 -0.06133 (-0.03116)	0.2086 0.1734 (0.1684)	0.1995 0.1839 (0.1655)	0.5119 0.4516 (0.6007)	-0.8512 -0.7871 (-1.247)
Sway [m]	0.0 0.0 (-0.01792)	0.2803 0.2623 (0.1876)	0.2803 0.2623 (0.1867)	1.604 1.45 (0.8383)	-0.8567 -0.7568 (-0.5412)
Heave [m]	-0.01567 -0.0156 (-0.04173)	0.04264 0.03521 (0.1768)	0.03966 0.03851 (0.1718)	0.1108 0.1094 (0.5298)	-0.1941 -0.1775 (-0.834)
Roll [deg]	0.0 -0.0001 (0.01787)	0.1085 0.0871 (0.0863)	0.1085 0.08714 (0.0844)	0.3673 0.3145 (0.313)	-0.3572 -0.3029 (-0.266)
Pitch [deg]	0.0 -0.0008 (-0.0232)	0.03189 0.03121 (0.0607)	0.03189 0.03122 (0.05607)	0.1067 0.1059 (0.19)	-0.1066 -0.1067 (-0.361)
Yaw [deg]	-0.04479 -0.04517 (-0.01049)	0.12509 0.09212 (0.0607)	0.1168 0.1026 (0.05976)	0.3494 0.2544 (0.158)	-0.5972 -0.5735 (-0.302)

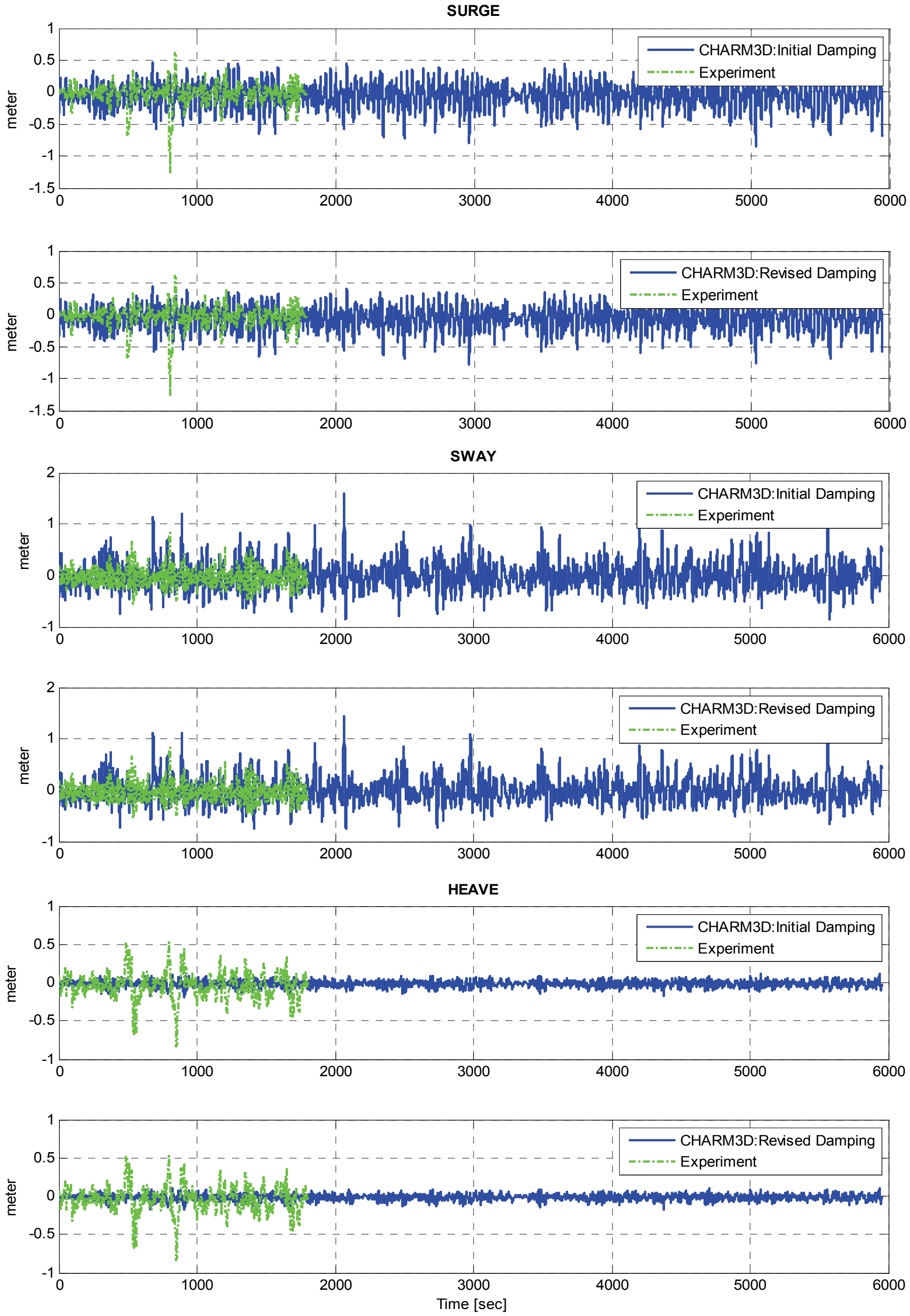

Figure 2.28 Comparison of Response Histories after Damping Estimation: Surge, Sway, Heave of Floating Quay, 2-body Case

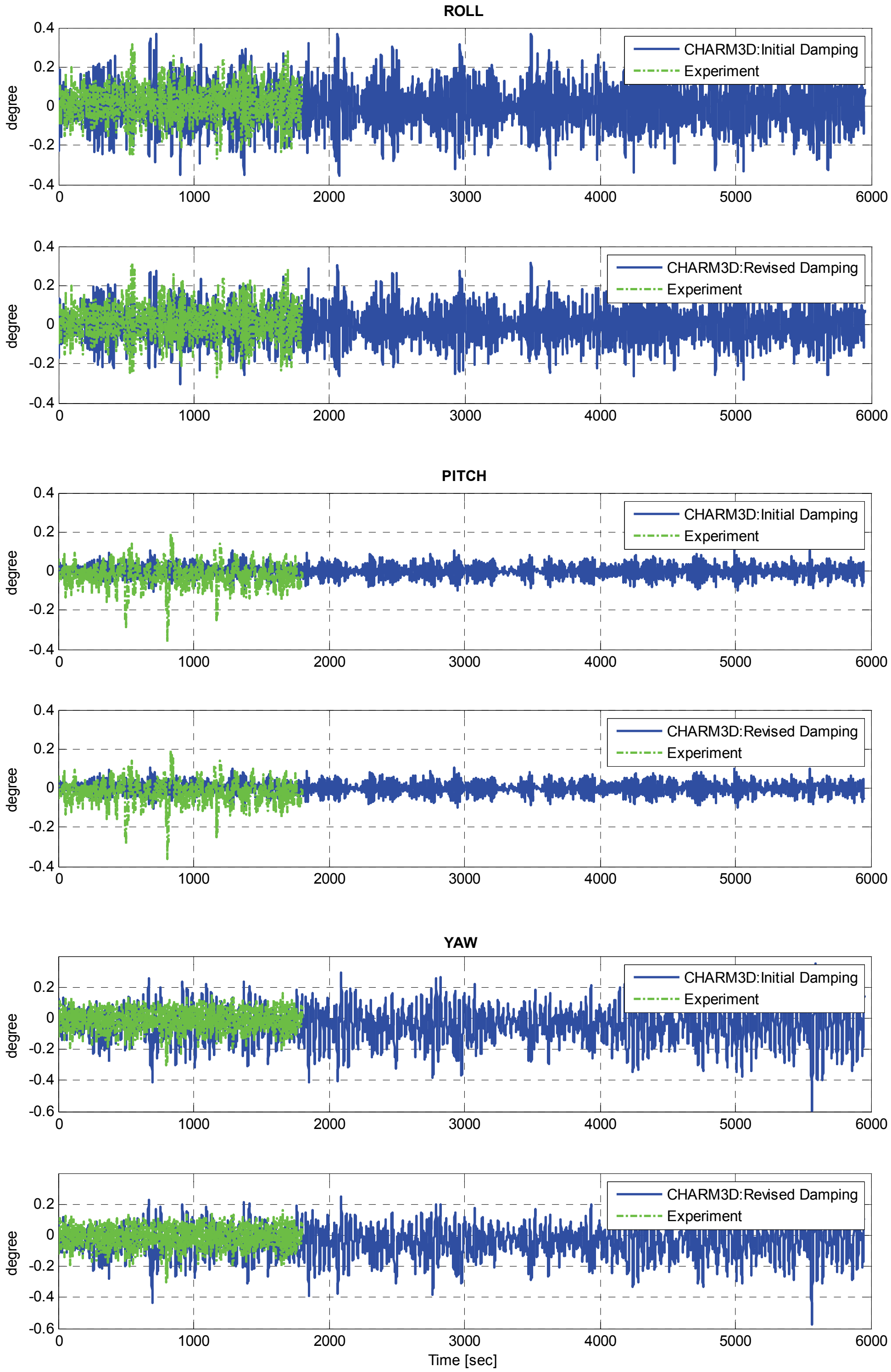

Figure 2.29 Comparison of Response Histories after Damping Estimation: Roll, Pitch, Yaw of Floating Quay, 2-body Case

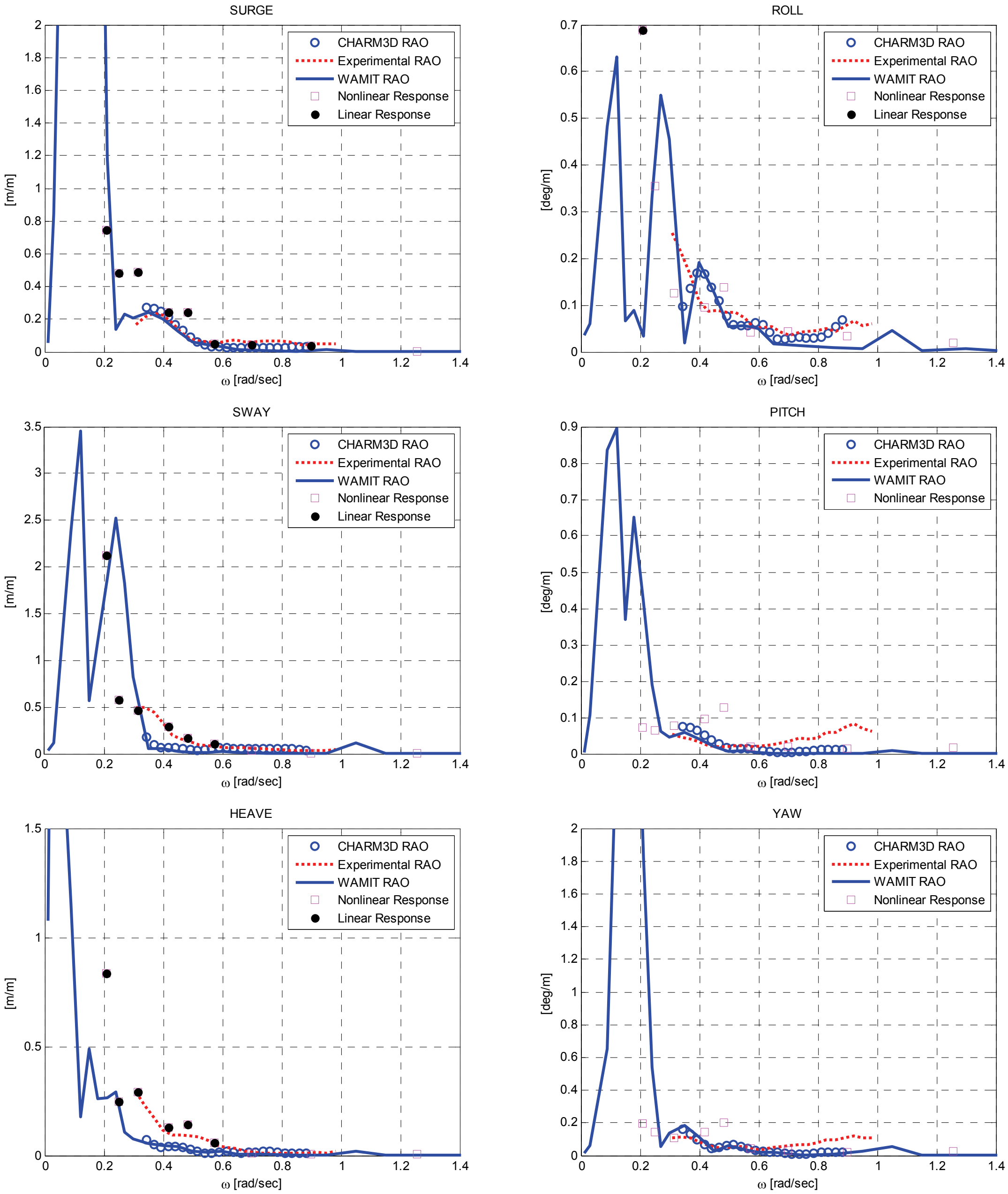

Figure 2.30 Total RAO Comparisons, 2-body Case

CHAPTER III

THREE BODY ANALYSIS: CONTAINER SHIP BETWEEN FLOATING QUAY AND FIXED QUAY

3.1 Introduction

This three-body case is taken up to investigate operability and survivability of the floating harbor system in case that a container ship operates on/off loading on both of starboard and port to the floating quay and the fixed quay simultaneously. The container ship is modeled as a 15000TEU class container ship and the floating quay and the fixed quay are identical to the previous two-body case. Experimental results are given by sets of responses to a series of regular wave tests and one irregular wave test from KORDI.

To implement the numerical analysis of this three-body case, we follow general processes identical to those of the two-body case; based on the same theoretical background, the WAMIT and CHARM3D are used. In addition, two calibrating processes are adopted as mentioned in Fig. 1.2: stiffness revision based on natural frequency comparison and damping estimation from response history comparison.

After optimization of the simulation, a series of results from experimental regular wave tests are compared with the results from simulation in terms of RAO on frequency domain, and the results from irregular wave test in experiment is compared with the results from the irregular wave test of simulation using CHARM3D.

Furthermore, motions of the container ship in the present floating harbor system are compared with that in a conventional harbor system, which does not have the floating quay but have a normal harbor, the fixed quay.

3.2 Frequency Domain Analysis

Based on the same theoretical backgrounds as previous, a set of input information for the numerical analysis is specified from the experiments; for example, the boundary condition to assign general boundary information, geometric information to specify the body surface boundary condition, and external dynamic information to solve the motion equations of the ship and the floating quay.

At first, boundary information is obtained from the previous case as shown in Table 3.1 in view of the fact that both of the experimental two-body and three-body cases are conducted in the same shallow water basin.

Table 3.1 Boundary Information

Water Depth [m]	18
Wave Heading [deg]	135
Wave Frequency region [rad/sec]	0.01~1.6
Number of discrete frequencies	25

3.2.1 Geometric Information

A set of coordinates is input to WAMIT, which present the wetted surfaces of the three bodies. Compared to the two-body case, this case has one more large-scaled structure, the 15000TEU container ship, next to the fixed quay, and the gaps are 1.6 m for longitudinal sides between the three bodies and a transverse side between the floating quay and the fixed quay as shown in Fig. 3.1.

In that the large scale two floating structures can be more sensitive to pumping effect, finer panels are used. And geometric particulars of the floating quay and the 15000TEU container ship are given from the KORDI as Table 3.2.

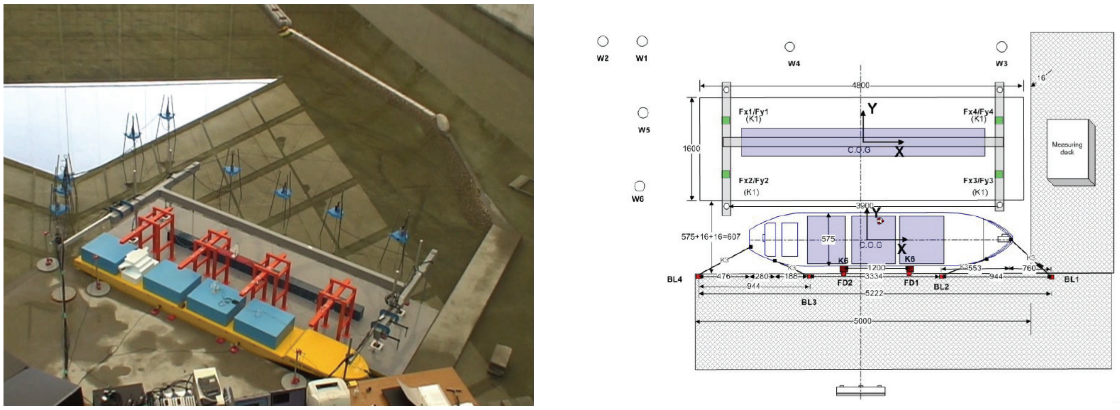

Figure 3.1 Experimental Schematic of Three-body Case

Table 3.2 Geometric Particulars of Floating Quay and Container Ship

	Floating Quay	*15000TEU Container Ship*
Length [meter]	480	400
Breadth [meter]	160	57.5
Draft [meter]	6	14
Shape of Submerged Part	Simple box barge type	Normal container ship hull

For the floating quay, the number of panels is increased to 5440 due to the smaller size of panels on the identical body shape to the two-body case.

In case of the 15000TEU container ship, it is not an existing ship, and thus the offset data is given by a virtual ship modeled by linear expansion of an existing maximum container ship. Based on the offset data, wetted surface of the ship is modeled by a set of 3304 panels as shown in Fig. 3.2.

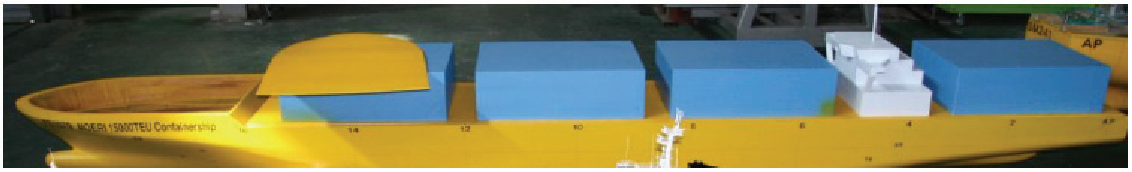

(a) Experimental Modeling

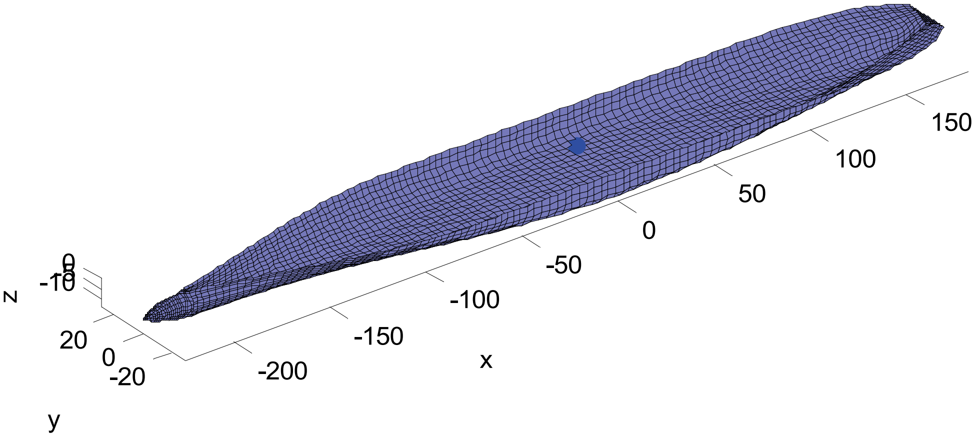

(b) Numerical Modeling

Figure 3.2 Panel Modeling of 15000TEU Container Ship

In the concrete, two parts of the ship demand caution in modeling the panels. The hull shape from one part between stem and stern can be regarded as a box barge with edge rounded off. In the stern and stem parts, however, there exist smoothly curved surface like a bulbous bow close to the mean water level and almost horizontal surface around the mean water level respectively. To make clearly perpendicular panels along mean water line, it is required to cut off the smoothly curved surface and replace them with discontinuous vertices to make vertical panels as shown in Fig. 3.3.

In the cases with hull panels identical to the original curved surface in stern and stem parts, the responses on time domain are diverged because of abnormal added mass and damping coefficient.

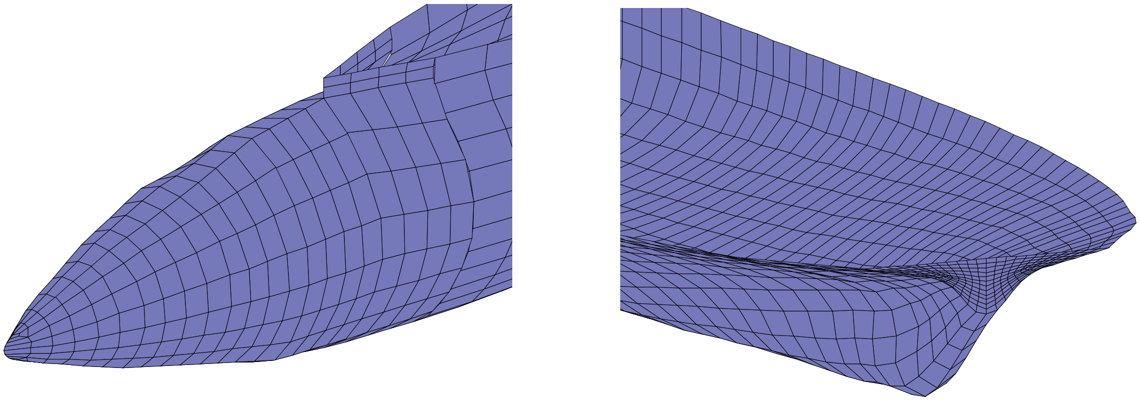
(a) stem (b) stern

Figure 3.3 Panel Modeling in Stern and Stem Parts of the Container Ship

Based on the experimental arrangement as shown in Fig. 3.1, origins of body coordinate system of each body are fixed as shown in Fig. 3.4. Body coordinate system of the floating quay coincides with a global coordinate system of the three-body case. As same as two-body case, origins of each body coordinate system are on mean water line with right-hand rule.

In case of the fixed quay, 2560 panels are used without bottom panels. Since the fixed quay is assumed to be fixed on sea floor, the panels on the bottom are dispensable.

By contrast with the previous two-body case, the gap distance for longitudinal and transverse sides is 1.6m; and even though there is increment of gap as much as 0.3m, the gap is still remarkably narrow relative to the scale of structures.

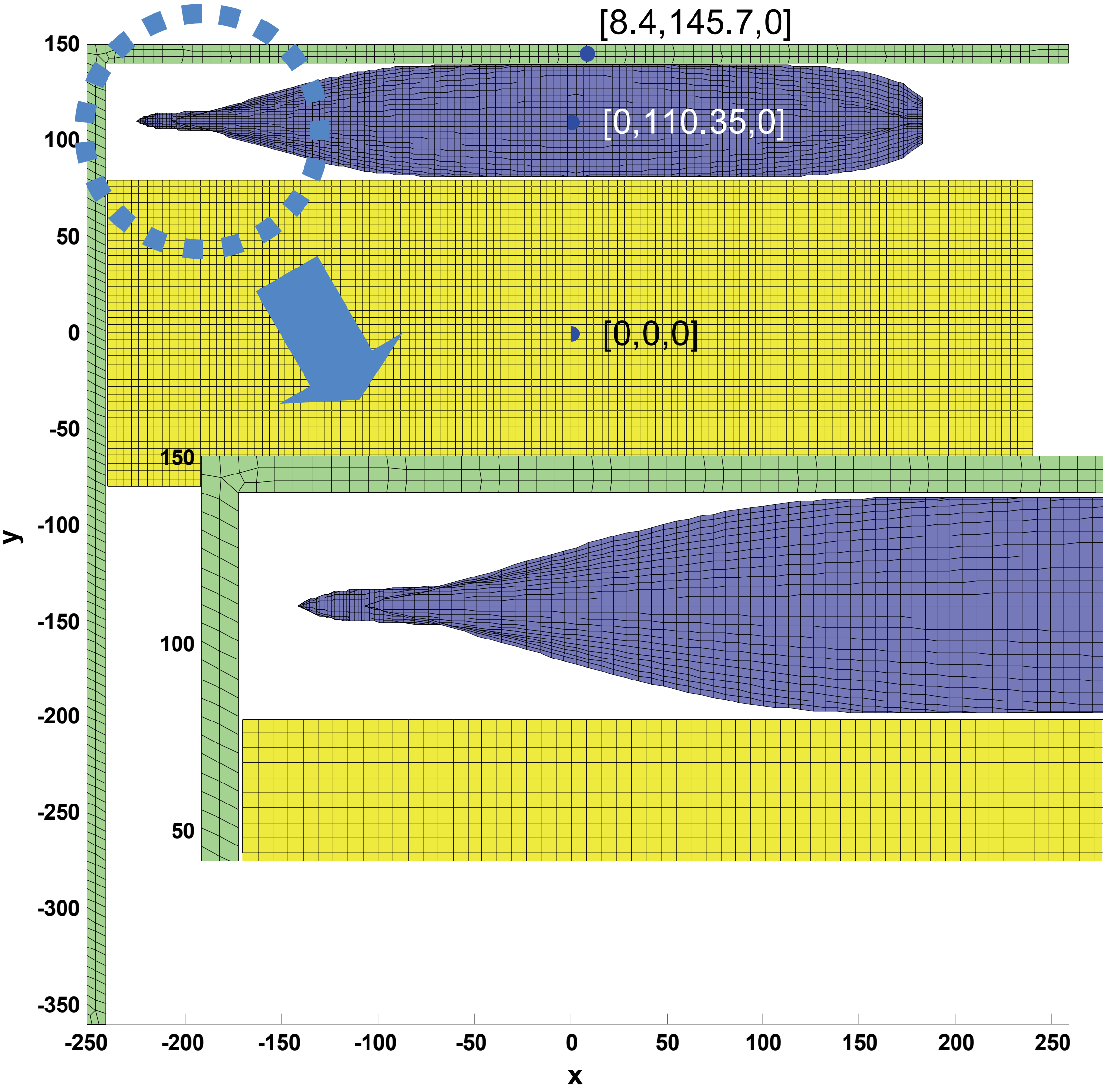

Figure 3.4 General Schematic of 3-body Case for Simulation

3.2.2 External Dynamic Information

To solve the motion equations of the two floating structures, the container ship and the floating quay, external mass, stiffness and damping coefficient are input. Main difference is the external dynamic information is given by 12×12 matrices since two bodies are analyzed in terms of 6 DOF motions of each body including full interaction between motions.

3.2.2.1 External Mass Matrix

Two 6×6 matrices of the floating quay and the container ship are calculated from the particulars as given in Table 3.3; the matrix of floating quay is identical to the previous case.

Table 3.3 Inertia Particulars of 15000TEU Container Ship

	15000TEU Container Ship
Mass	2.1370E+008 kg
C.G.	[0 , 0 , 9.2]
$[I^B_{XX}, I^B_{YY}, I^B_{ZZ}]$	[1.4873E+011, 2.5107E+012, 2.4926E+012]
$[I^B_{XY}, I^B_{YZ}, I^B_{ZX}]$	[0 , 0 , 0]

I_{XX}, I_{YY}, I_{ZZ} are calculated from the conventional equations;

$$\begin{aligned} I_{XX} &= K_{XX}{}^2 \times m, \quad K_{XX} = 0.42 \times Breadth \\ I_{YY} &= K_{YY}{}^2 \times m, \quad K_{YY} = 0.25 \times Length \\ I_{ZZ} &\approx I_{YY} \end{aligned} \tag{3.1}$$

Thus the external mass matrix of the ship is

$$M_{CS} = \begin{bmatrix} 2.1370\mathrm{E}+8 & 0 & 0 & 0 & 1.9661\mathrm{E}+9 & 0 \\ 0 & 2.1370\mathrm{E}+8 & 0 & -1.9661\mathrm{E}+9 & 0 & 0 \\ 0 & 0 & 2.1370\mathrm{E}+8 & 0 & 0 & 0 \\ 0 & -1.9661\mathrm{E}+9 & 0 & 1.4873\mathrm{E}+11 & 0 & 0 \\ 1.9661\mathrm{E}+9 & 0 & 0 & 0 & 2.5107\mathrm{E}+12 & 0 \\ 0 & 0 & 0 & 0 & 0 & 2.4926\mathrm{E}+12 \end{bmatrix} \quad (3.2)$$

Two mass matrices of the floating quay and container ship are composed as

$$M_{E\_Total} = \begin{bmatrix} M_{FQ} & 6\times 6 \ \ zero\,matrix \\ 6\times 6 \ \ zero\,matrix & M_{CS} \end{bmatrix} \quad (3.3)$$

Total external mass matrix M_{E_Total} consists of four 6×6 matrices: mass matrix of floating quay M_{FQ} as equation (2.5), that of the container ship M_{CS}, and two 6×6 zero matrices.

3.2.2.2 External Stiffness Matrix

In the same manner as the two-body case, we at first estimate the linear spring stiffness for translational motions based on the schematic of a real mooring system as shown in Fig. 3.5. And then the external stiffness matrix of each body is calculated with the coupled stiffness in 6 DOF motions.

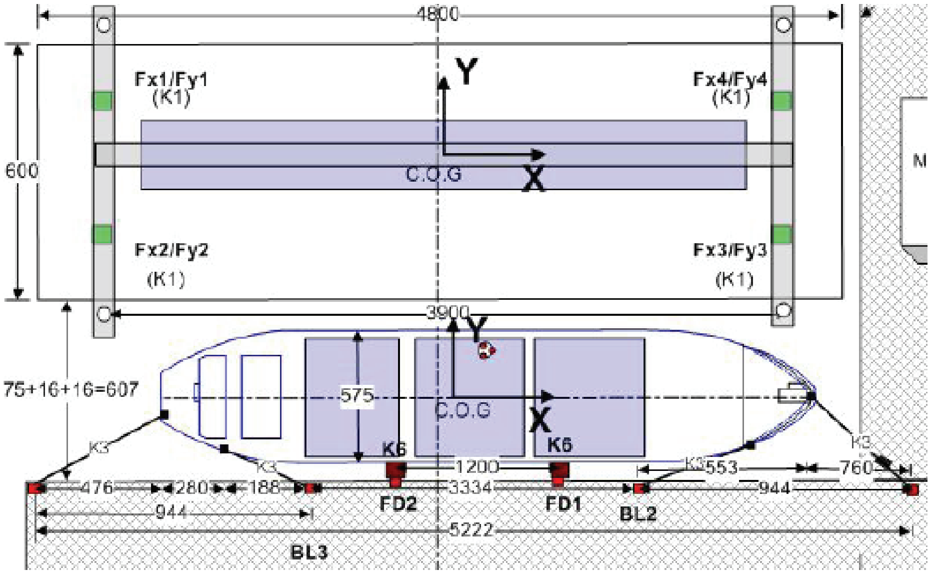

Figure 3.5 Schematic of Mooring System for Three Body Case

From the figure above, the floating quay is moored by four dolphin fenders at points indicated as K1, and the container ship is moored by four hawsers indicated as K3 and two fenders presented as K6.

Considering stiffness of positive and negative motions, stiffness of the floating quay can be considered as symmetric since dolphin fender is equipped with four linear springs in the experiment, as shown in Fig. 3.6; however stiffness of ship is asymmetric.

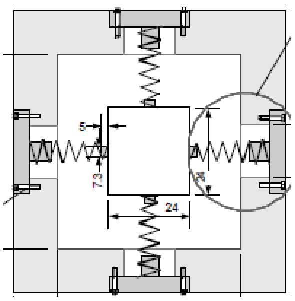

Figure 3.6 Experimental Dolphin Fender

Thus, in case of the floating quay original stiffness of dolphin fender is used as stiffness for the linear spring, and mooring system of the container ship is simplified as stiffness estimated from experimental reaction forces of fenders and hawsers, as described in Section 2.2.3.2. The stiffness of each linear spring of both bodies is given in Table 3.4.

Table 3.4 Stiffness of Linear Springs of Three-body Case

Motion	Floating Quay Stiffness [N/m]	Container Ship Stiffness [N/m]
SURGE	3.92E+7	4.1921E+5
SWAY	3.92E+7	10.1856E+5
HEAVE	0.4482E+7	0.61856E+5

For both of the floating quay and the container ship, each one forth stiffness of surge, sway, and heave are assumed to act on four points, which are positions same as dolphin fenders and connecting points of hawser lines/fenders respectively. Coordinates of the acting points are given in Table 3.5 with respect to each body coordinate system.

Table 3.5 Spring Positions of Three-body Case

Point Number	Floating Quay	Container Ship
P1	-195, -40, 0.1	-225.26 , 0.0 , 30
P2	-195, 40, 0.1	-170.6 , 14.0 , 30
P3	195, -40, 0.1	175.3 , 17,41 , 30
P4	195, 40, 0.1	190.5 , 6.3 , 30

From these two sets of information, the external stiffness matrix is calculated for each body using the formulas same as described in Section 2.2.3.2

$$K_{EFQ} = \begin{bmatrix} 3.92\text{E}+7 & 0 & 0 & 0 & 3.92\text{E}+006 & 0 \\ 0 & 3.92\text{E}+7 & 0 & -3.92\text{E}+006 & 0 & 0 \\ 0 & 0 & 4.482\text{E}+6 & 0 & 0 & 0 \\ 0 & -3.92\text{E}+6 & 0 & 7.1716\text{E}+009 & 0 & 0 \\ 3.92\text{E}+6 & 0 & 0 & 0 & 1.7043\text{E}+011 & 0 \\ 0 & 0 & 0 & 0 & 0 & 15.533\text{E}+011 \end{bmatrix} \tag{3.4}$$

$$K_{ECS} = \begin{bmatrix} 4.1921\text{E}+5 & 0 & 0 & 0 & 1.258\text{E}+7 & 0 \\ 0 & 10.1856\text{E}+05 & 0 & -3.056\text{E}+7 & 0 & 0 \\ 0 & 0 & 6.1856\text{E}+4 & 583148 & 383012 & 0 \\ 0 & -3.056\text{E}+07 & 583148 & 9.2504\text{E}+8 & 0 & 0 \\ 1.258\text{E}+7 & 0 & 383012 & 0 & 2.6789\text{E}+9 & 0 \\ 0 & 0 & 0 & 0 & 0 & 3.8125\text{E}+10 \end{bmatrix} \tag{3.5}$$

In terms of two moving structures, total external stiffness K_{E_Total} is composes as

$$K_{E\_Total} = \begin{bmatrix} K_{EFQ} & 6\times 6 \ \textit{zero matrix} \\ 6\times 6 \ \textit{zero matrix} & K_{ECS} \end{bmatrix} \tag{3.6}$$

In same order as external mass matrix, 6×6 external stiffness matrix of the floating quay K_{EFQ} and that of the container ship K_{ECS} are placed.

In case that two floating structures are moored to each other, the coupled stiffness, which is indicated as 6×6 zero matrix in the equation (3.6), should be calculated. The present three-body case, however, have a separate mooring system; the floating quay is moored to the sea floor by the dolphin fender system, and the ship is moored to the fixed quay by fenders and hawser lines. Thus there is no effect of the coupled stiffness between each body.

3.2.2.3 External Damping Coefficient Matrix

As same as the two-body case, viscosity effect of real fluid is ignored in the frequency domain analysis; therefore, the external damping coefficient matrix is zero since there is no even an additional external damper in this three-body case. In time domain analysis, viscous effect is included into total damping force, which represents uncertain damping mechanism in the floating harbor system; in example, energy dissipation can be caused by a nonlinear deformation of fenders or collapse between structures.

3.2.3 Results of Hydrodynamic Properties

Based on the same theoretical backgrounds as mentioned in Section 2.2.4, four hydrodynamic properties and responses are obtained for the two floating structures, the 15000TEU container ship and the floating quay, using WAMIT: added mass/ moment of inertia, radiation damping coefficient, wave exciting force/moment, mean drift force/moment, RAO. Added mass and damping coefficients are plotted only for diagonal terms in the 12×12 matrix. Wave exciting force and mean drift force are the results of real values. From Fig. 3.7 to Fig. 3.11 the results of the floating quay are shown. And Fig. 3.12 to Fig. 3.16 show the results of the container ship. Fig. 3.17 shows the comparison of the free surface elevation comparison between experiment and simulation; the comparison show agreement with acceptable differences from experiment and simulation due to the assumptions such as harmonic wave, inviscid fluid.

The hydrodynamic properties have tendency to fluctuate along frequencies, which represent the pumping effects at the gaps and the effect of irregular frequencies in high frequency region; at this point, the irregular frequencies mean a well-known erroneous of the numerical analysis using Green theorem and source formulation (CH Lee, 1995).

The first calibrating process described in Fig. 1.2 is carried out based on the fact that the comparison of RAO shows disagreement such that the peaks in low frequency region, which represent the natural frequency of the system. Therefore, the natural frequency of the simulation should be corrected to be matched with experiment since the natural frequencies of a certain structure are unique characteristic of the structures, which is fixed as long as the mass and stiffness of the structure is fixed.

In the present numerical analysis, it is one of the most essential things to input the mass and stiffness of certain objects as accurate as possible; especially in such a comparative study, the values should be identified to the experimental values.

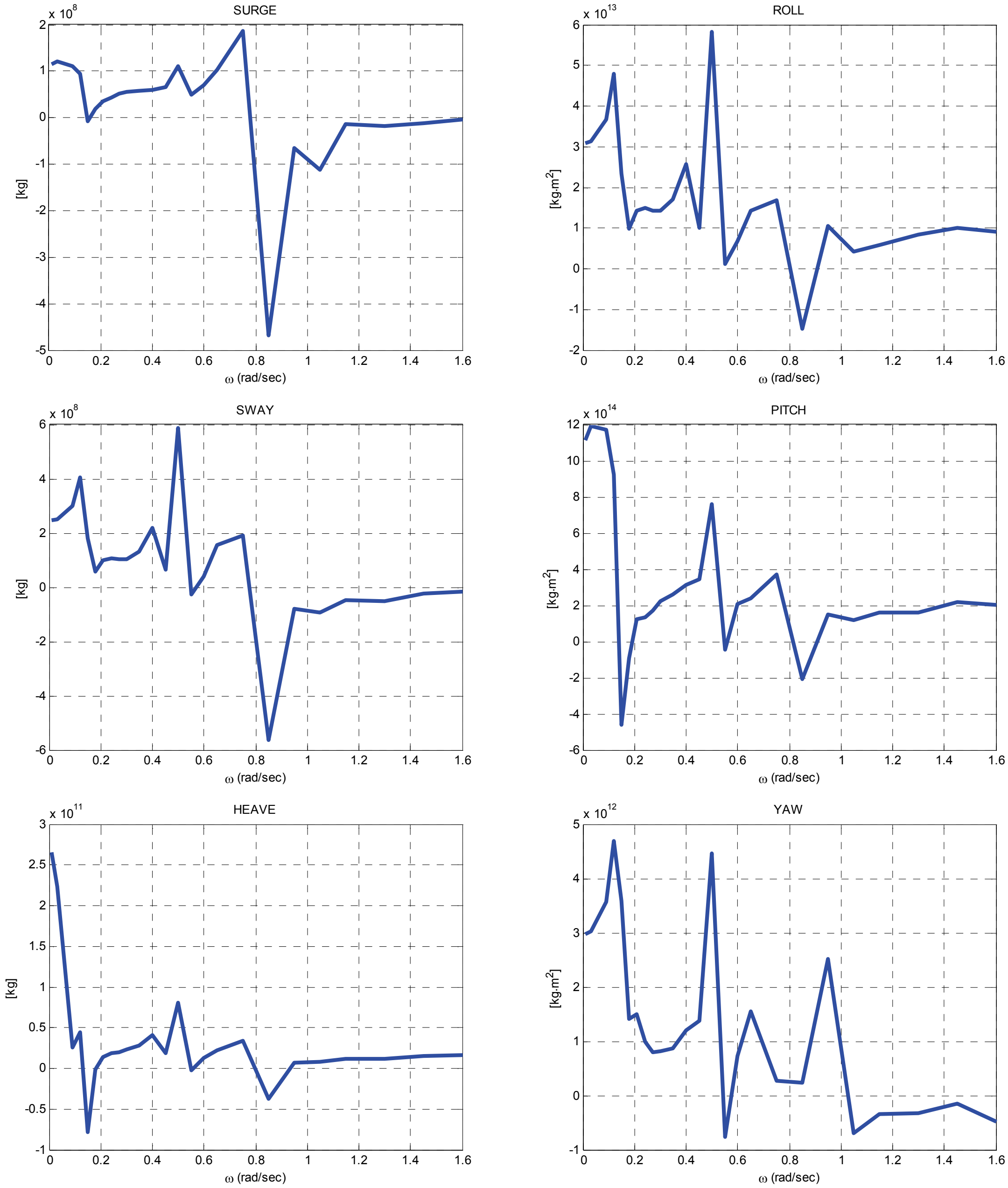

Figure 3.7 Added Mass/Moment of Inertia of Floating Quay, 3-body Case

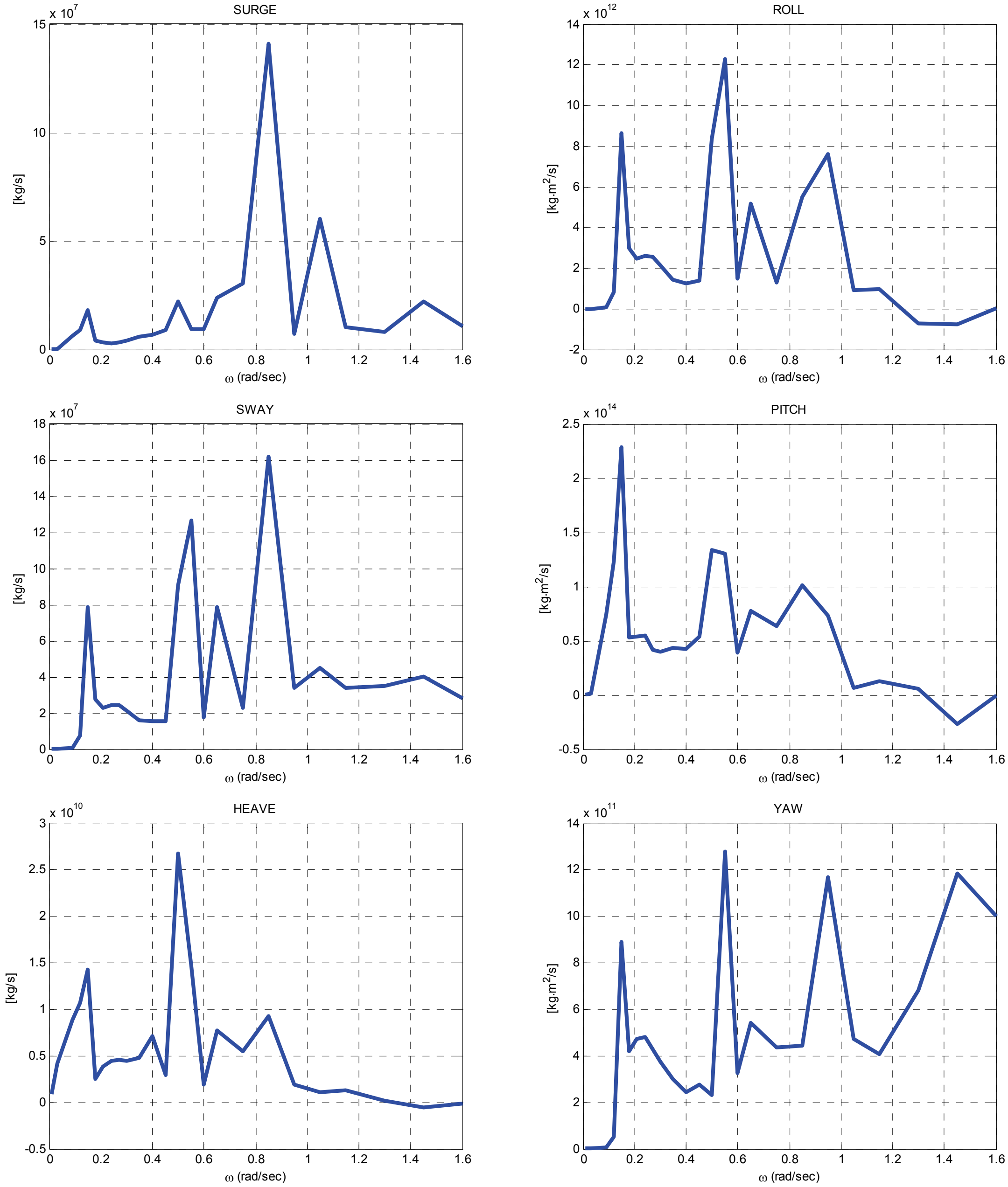

Figure 3.8 Radiation Damping Coefficients of Floating Quay, 3-body Case

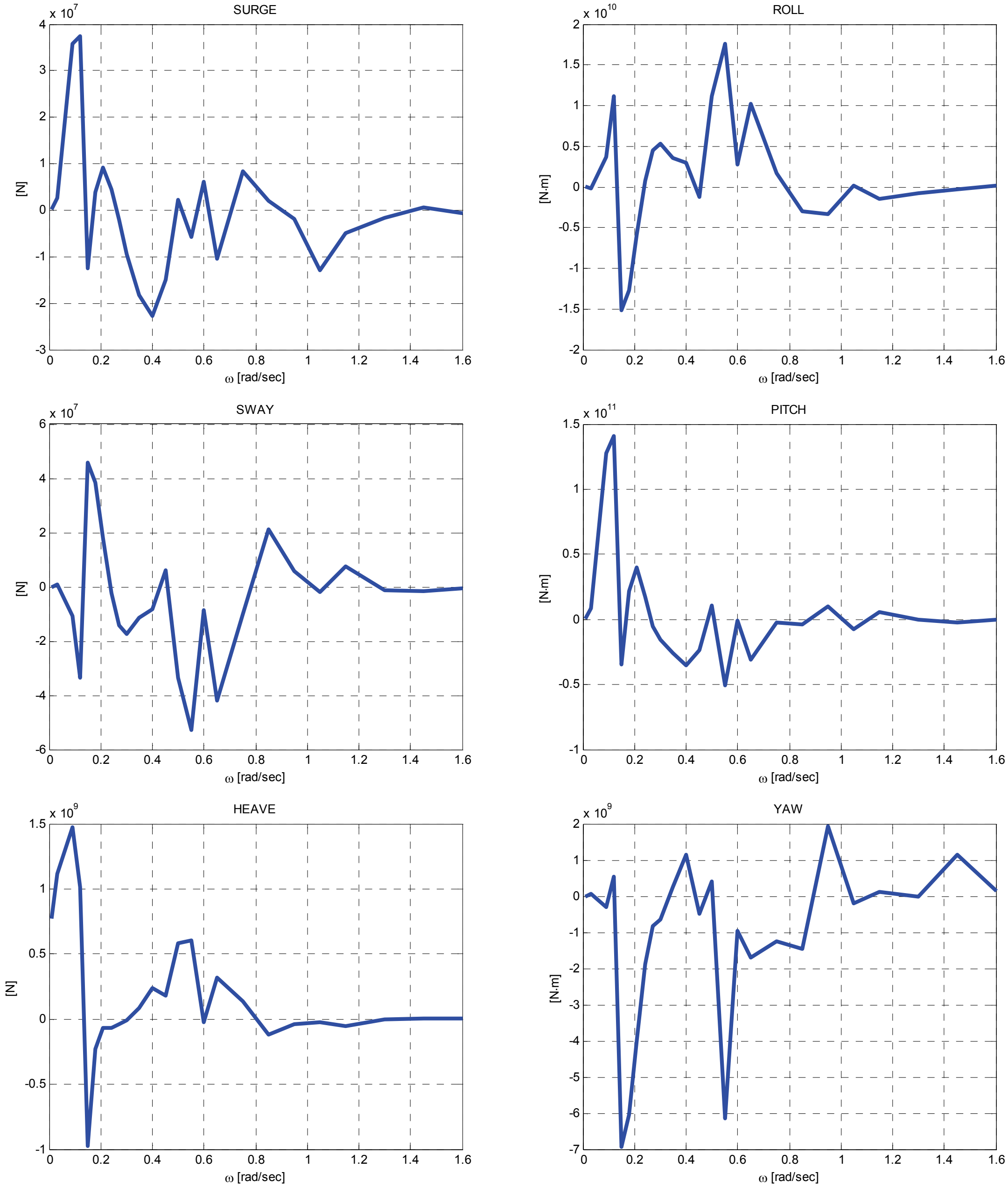

Figure 3.9 First Order Wave Force of Floating Quay, 3-body Case

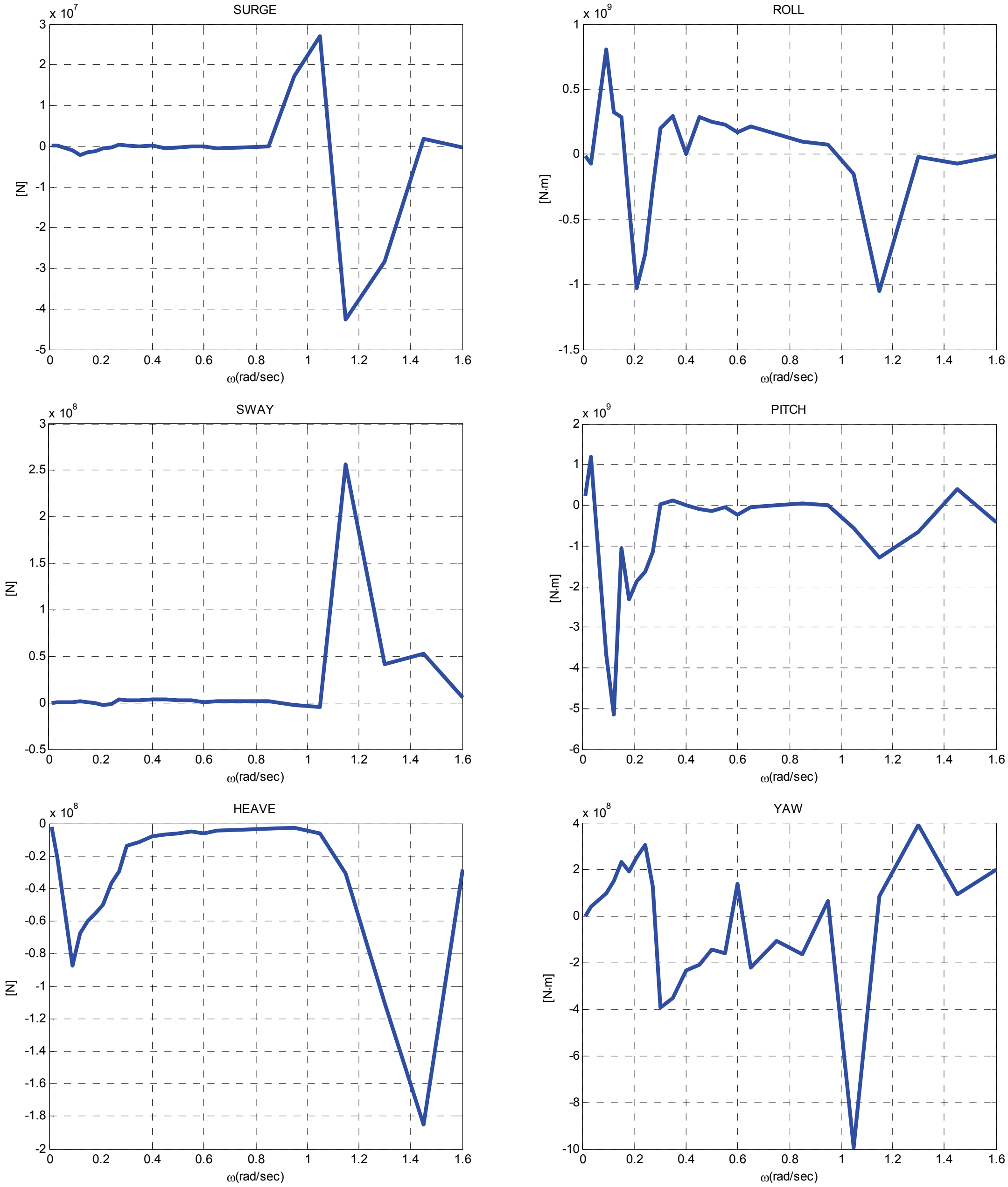

Figure 3.10 Mean Drift Force of Floating Quay, 3-body Case

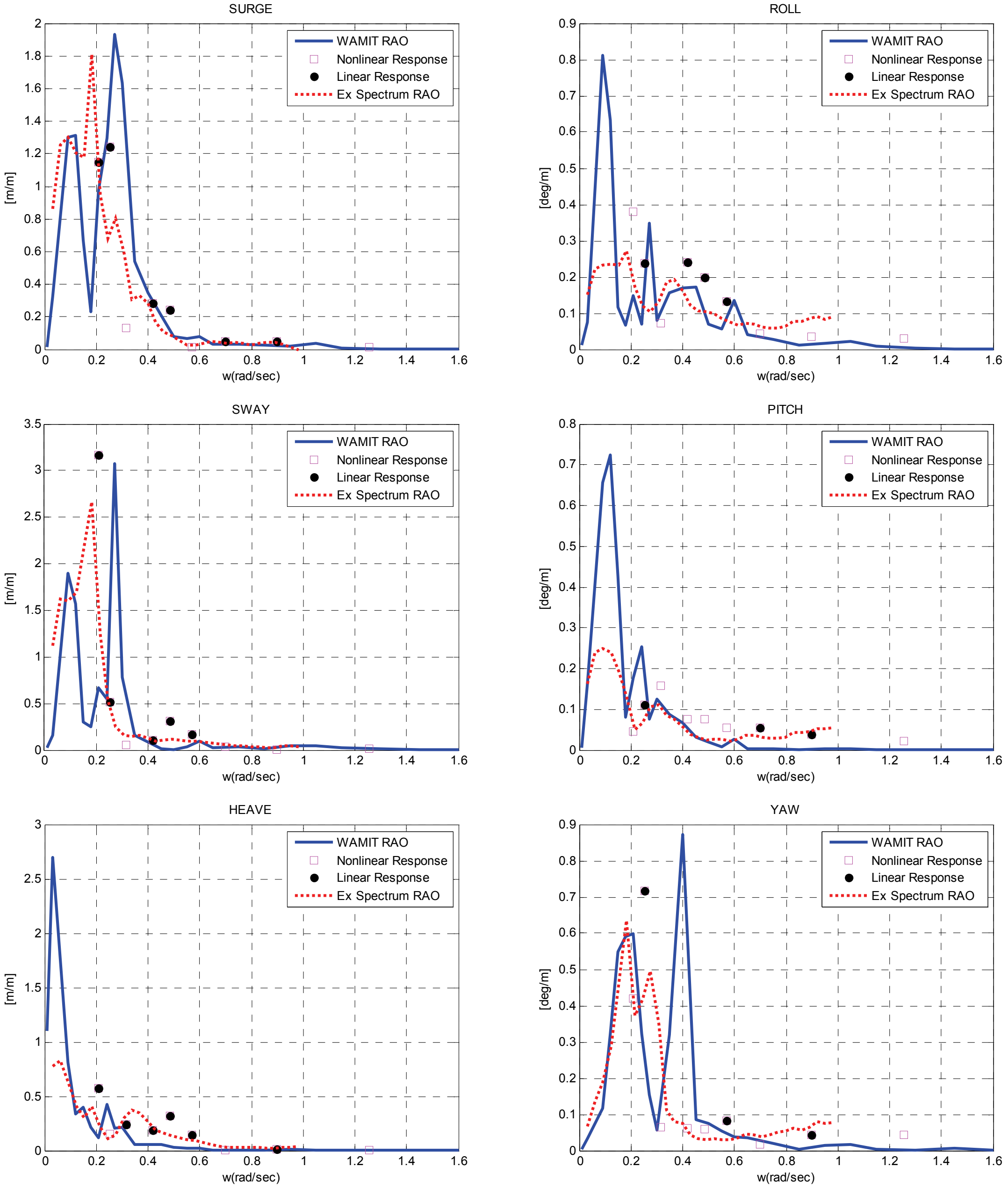

Figure 3.11 RAO Comparison of Floating Quay, 3-body Case

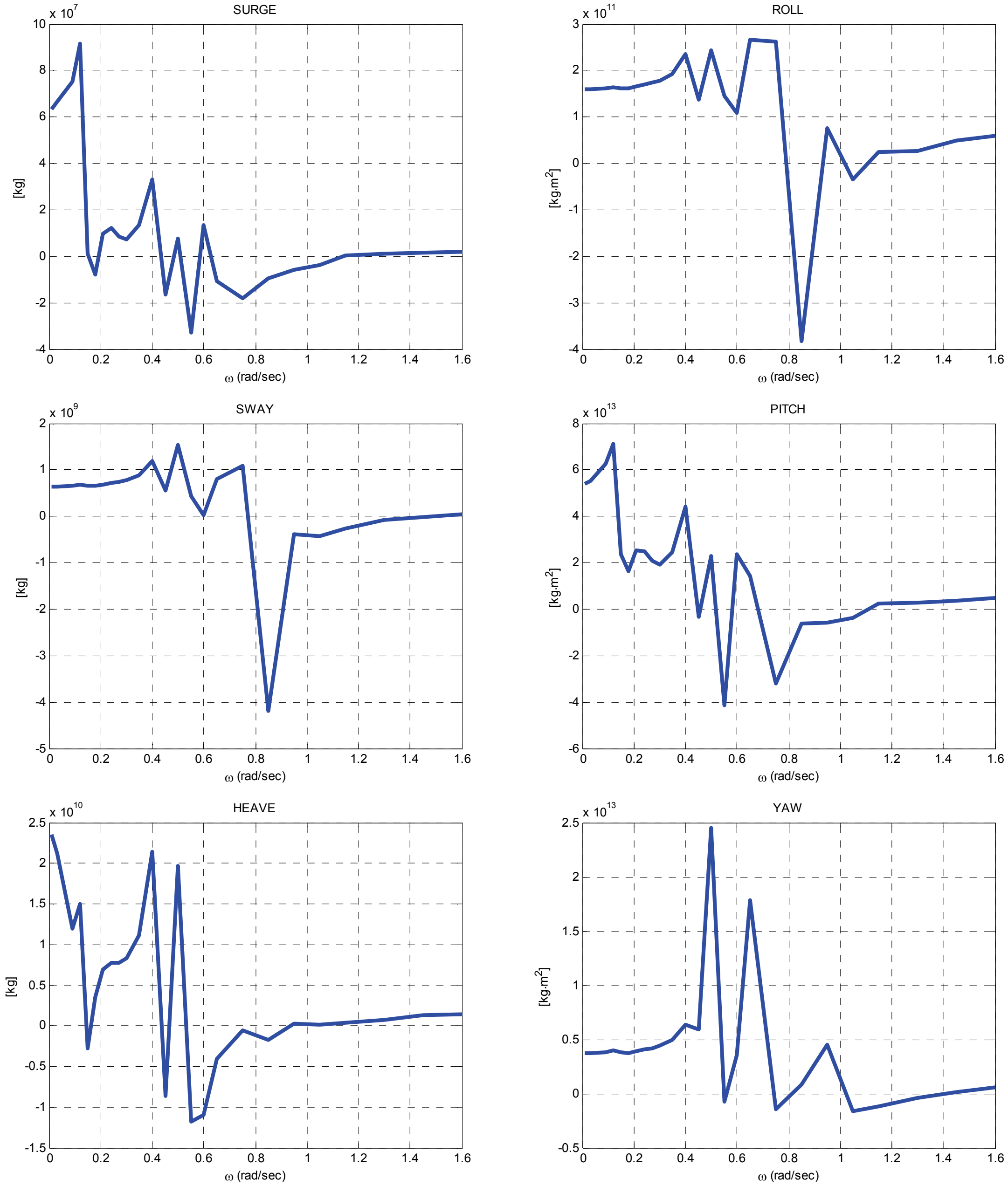

Figure 3.12 Added Mass/Moment of Inertia of the Container Ship, 3-body Case

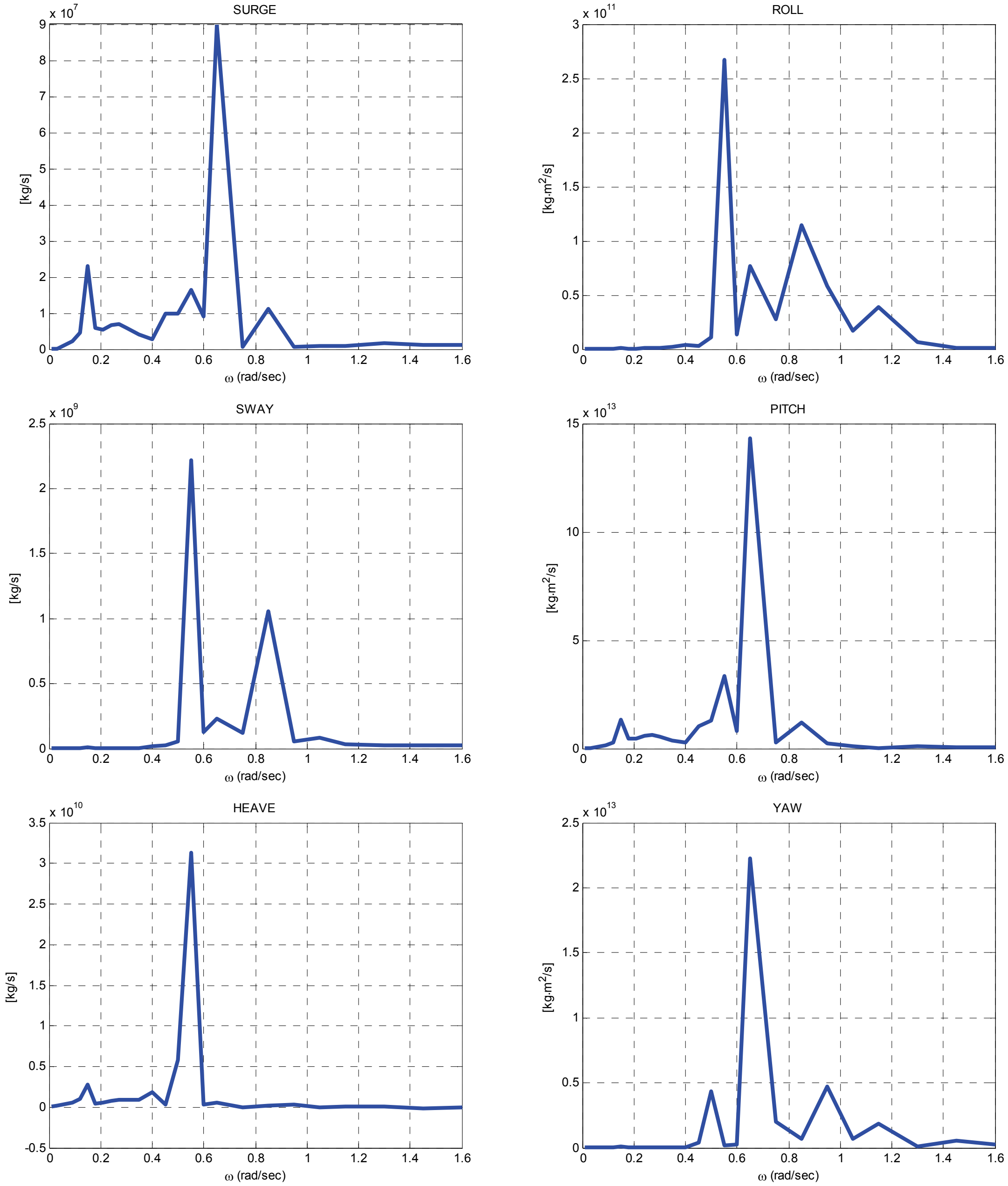

Figure 3.13 Radiation Damping Coefficients of Container Ship, 3-body Case

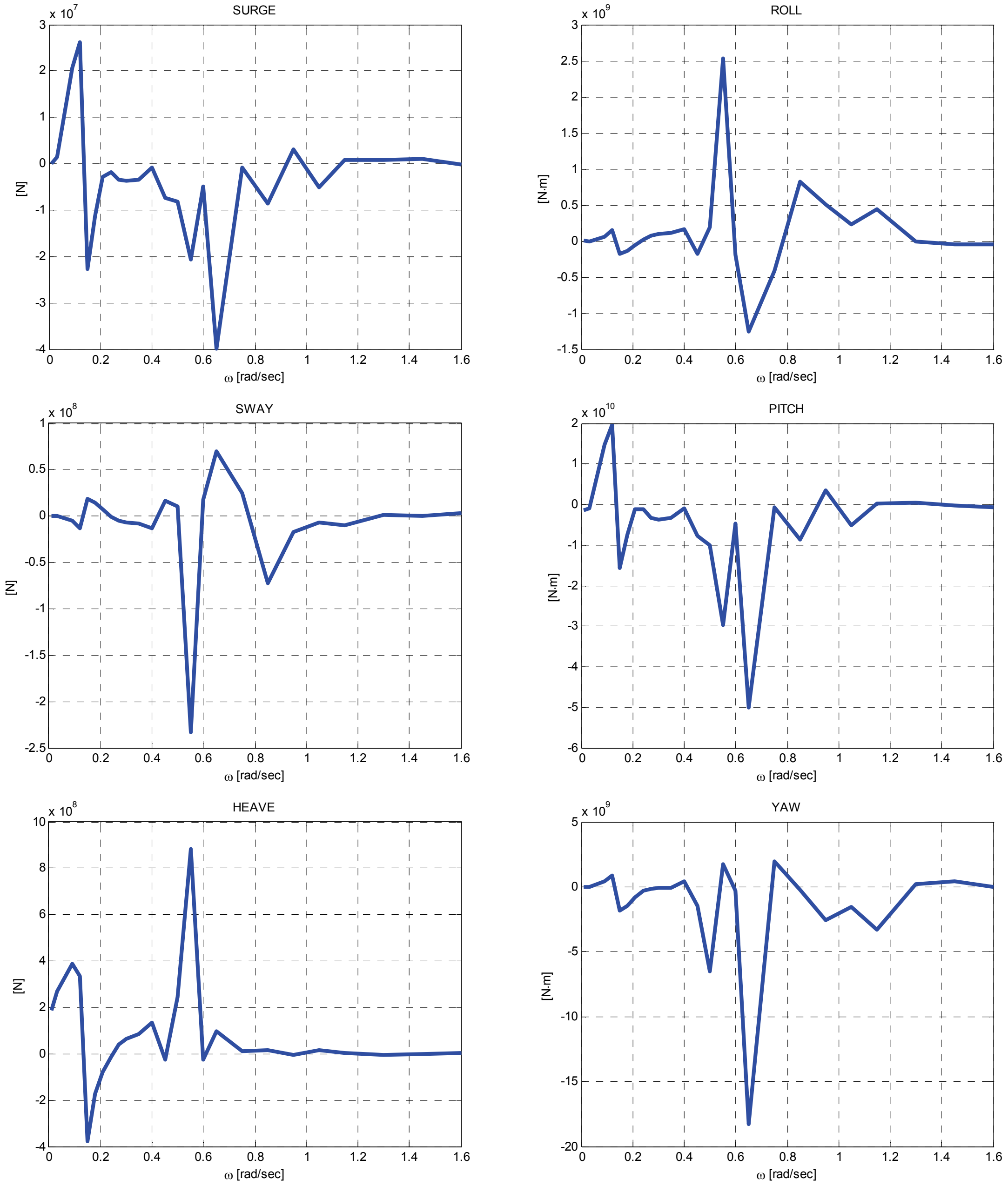

Figure 3.14 First Order Wave Force of Container Ship, 3-body Case

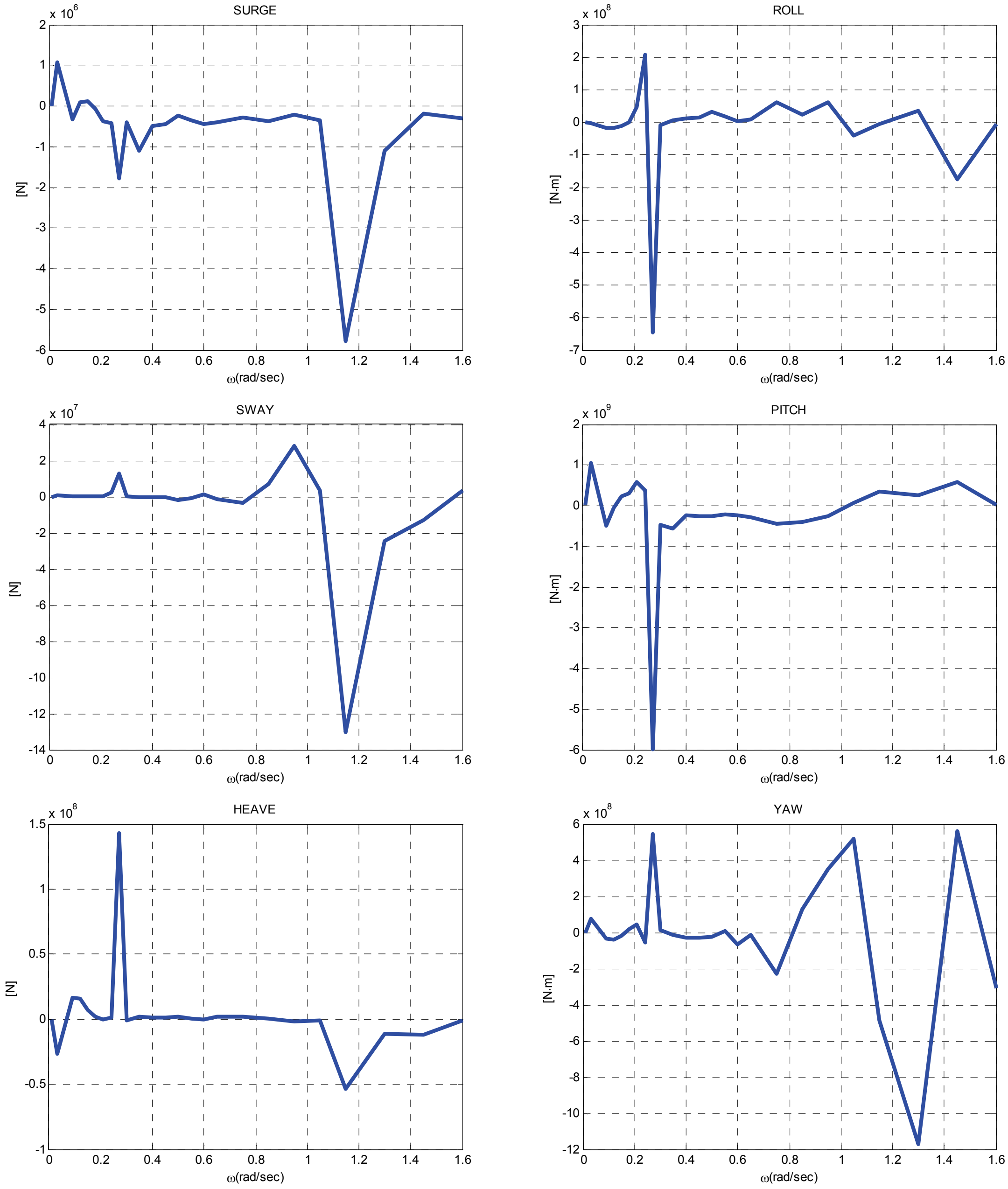

Figure 3.15 Mean Drift Force of Container Ship, 3-body Case

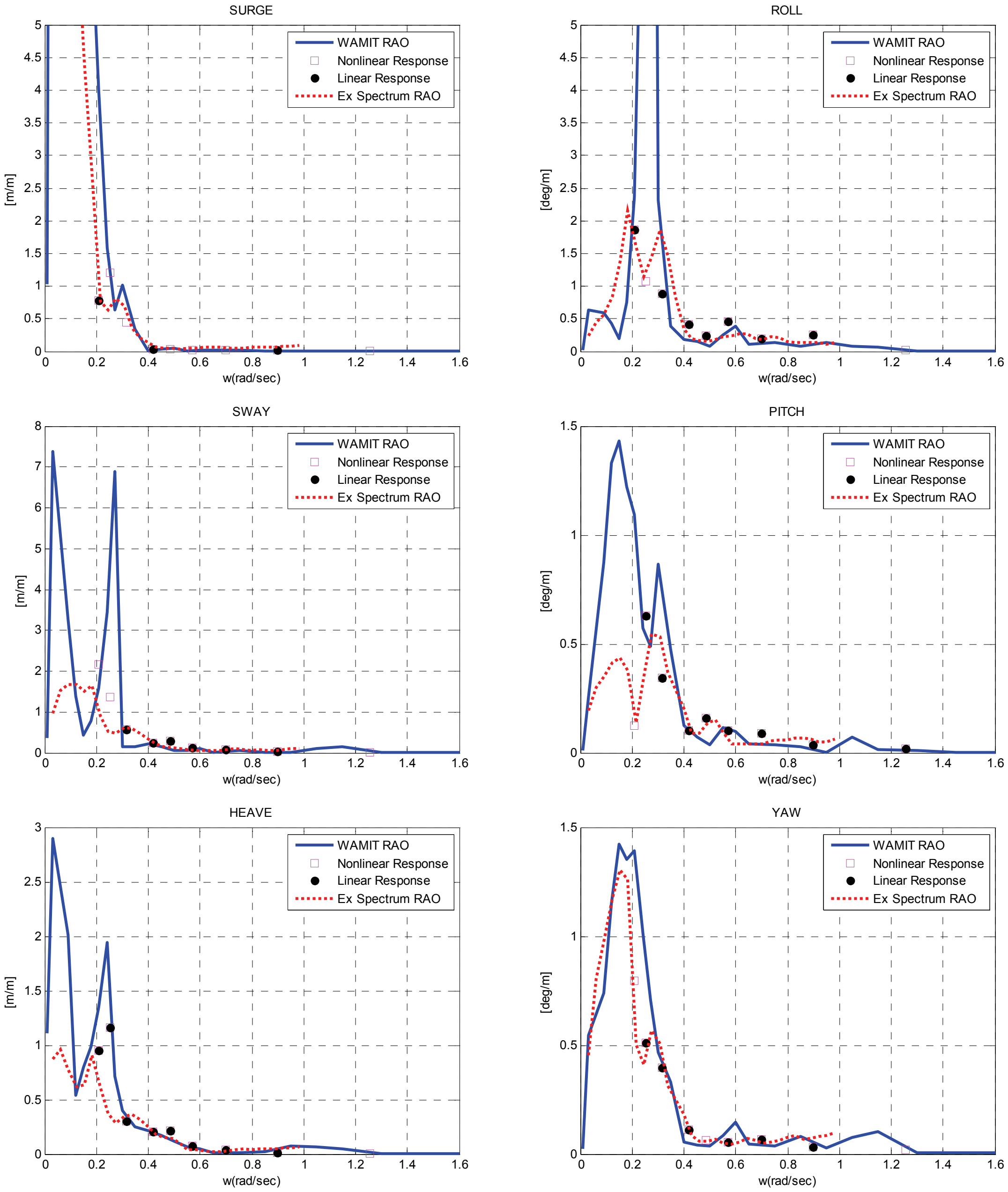

Figure 3.16 RAO Comparison of Container Ship, 3-body Case

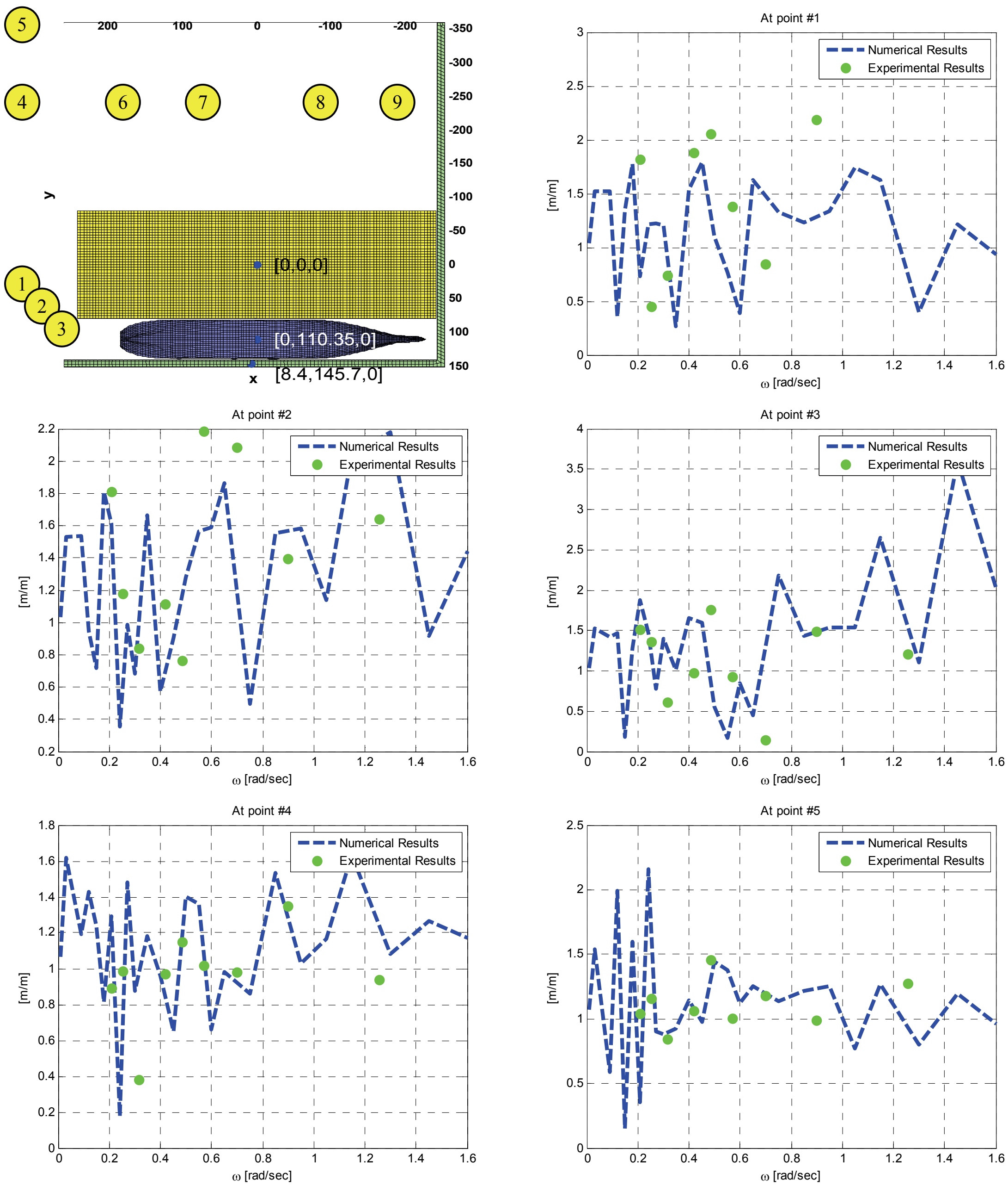

Figure 3.17 Free Surface Elevation Comparison, 3-body Case

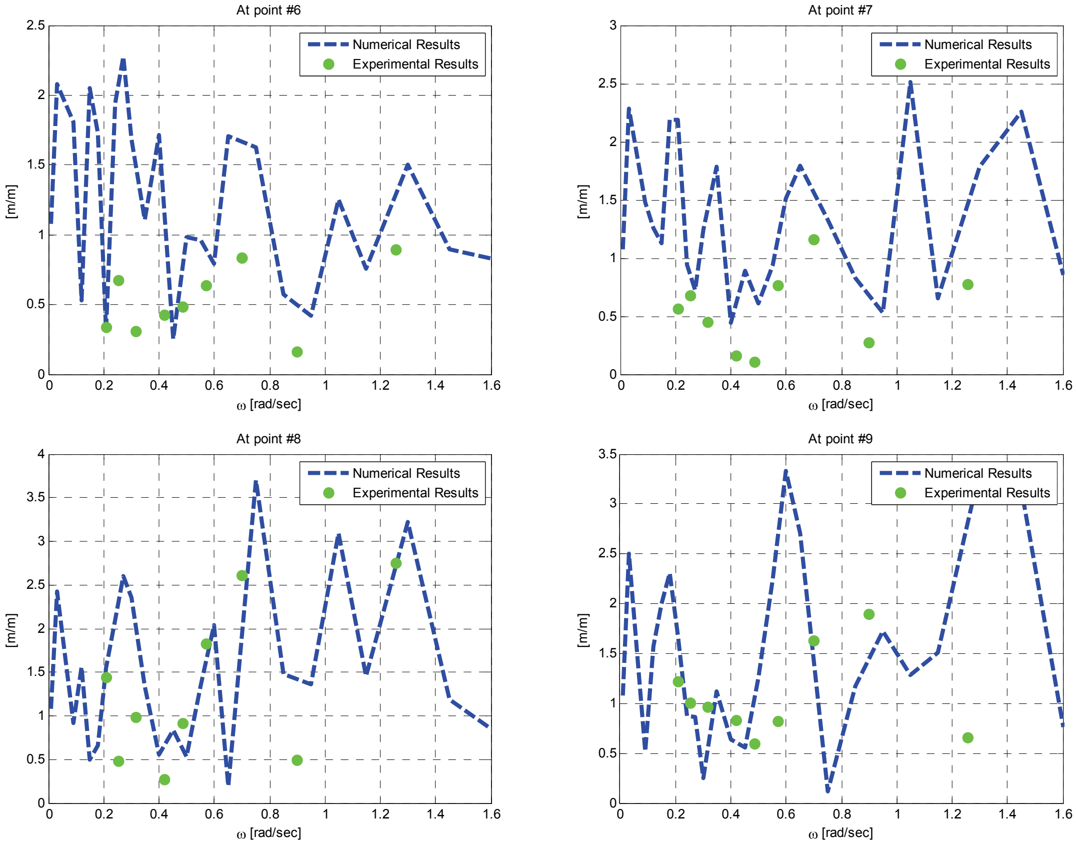

Figure 3.17 Continued

3.2.4 Calibration I: Stiffness Revision

From the comparisons of RAO, we can recognize offsets of peaks in low frequency region between the experiment and simulation, which indicate the difference of natural frequencies in the simulation from those in the experiment. Especially, the differences are found in surge, sway, and yaw motions, which have dominant effect of the external stiffness, as more clearly shown in Fig. 3.18.

Natural frequencies of the simulation are corrected by changing stiffness, one of the variables of the natural frequency; the formula of a natural frequency is given by

$$\omega^2 = \frac{K_{Total}}{M + \Delta M_{\omega}} \tag{3.7}$$

The natural frequency ω is a function of mass of the structure M , the added mass at the frequency ΔM_{ω} , and the total stiffness K_{Total}, which is the sum of the external stiffness K_E and the hydrostatic stiffness K_H. In the variables of the natural frequency, all values are fixed or calculated from WAMIT except for the K_E. And one thing to note is that the K_E is temporally estimated from the measured reaction force data of the fenders and hawser lines; therefore, it is possible to cause the differences in the natural frequencies between the experiment and simulation.

As a first step, natural frequencies of each motion for respect body should be clarified; for example, from the fact that this three-body case consists of two floating structures and one fixed structures, the interactions among them are quite complex than a single body or the previous two-body case. The interactions are also presented in terms of peaks in the RAO's of 6 DOF motions for each body such that certain peak frequencies exist not only in one mode but also in the other modes; for example, the motions, which have strong coupling effects, such as surge and pitch, sway and roll have certain peak frequencies in common. Therefore, to clarify the natural frequency of each motion is not simple.

Considering such a difficulty, we can find the natural frequencies based on a set of criteria as below for the purpose to find natural frequencies only for surge and sway motions of each body;

1. The natural frequency is usually placed in low frequency region.

2. The natural frequency of surge or sway motions also appear in RAO's of pitch and roll motions, respectively.
3. The natural frequency of surge or sway motions of a floating structure also appear in RAO's of the same motions of the other floating structure, respectively.
4. Finally, the natural frequency can be exactly obtained by free decay test of experiment.

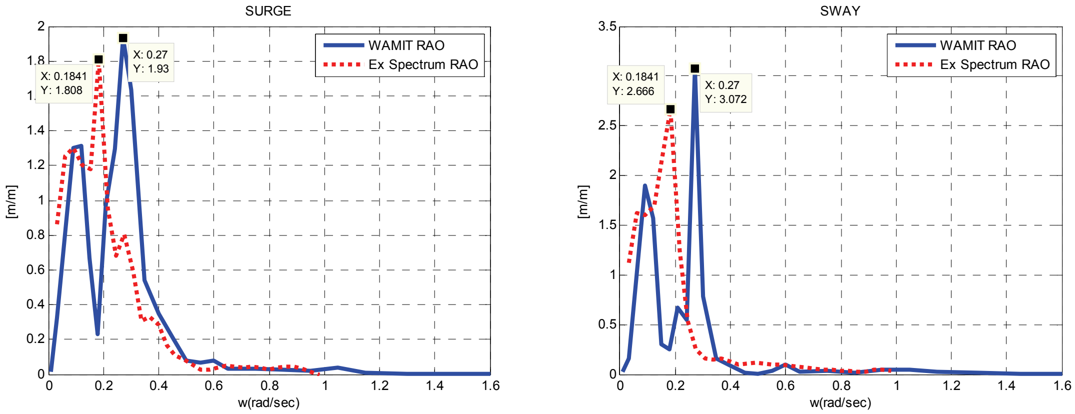

(a) The Floating Quay

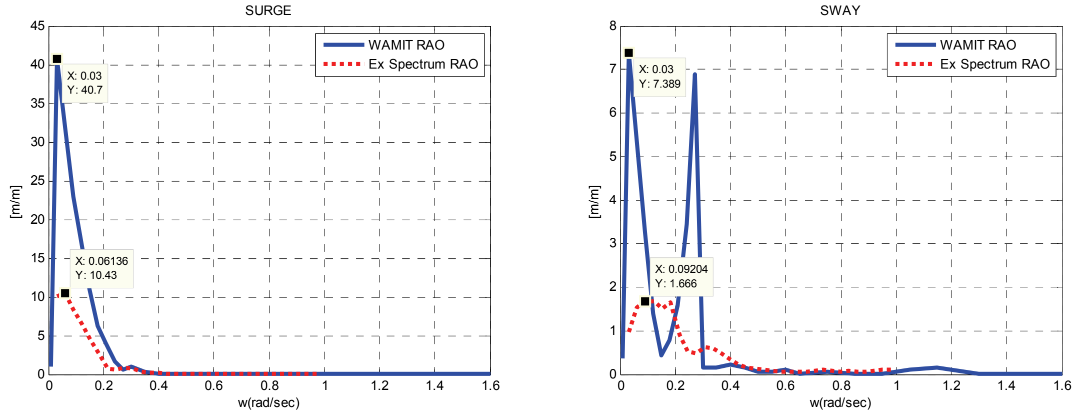

(b) The Container Ship

Figure 3.18 RAO Comparison of Surge and Sway

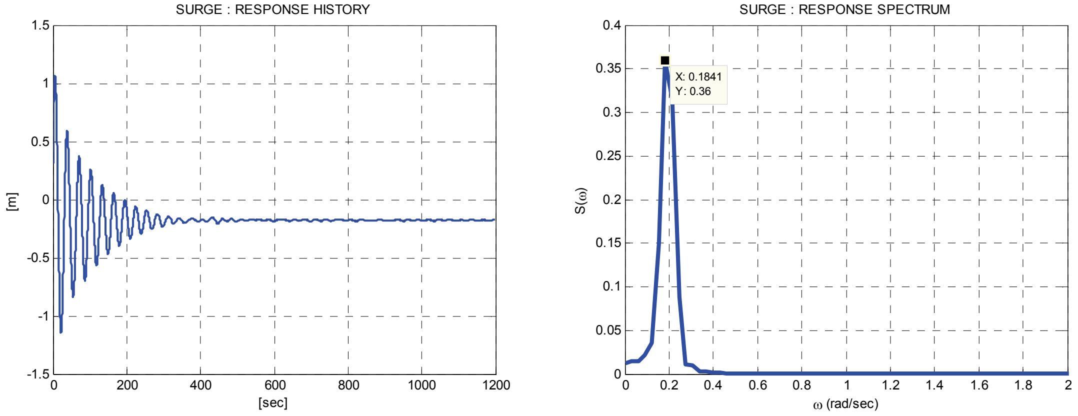

(a) Free Decay Test : Surge

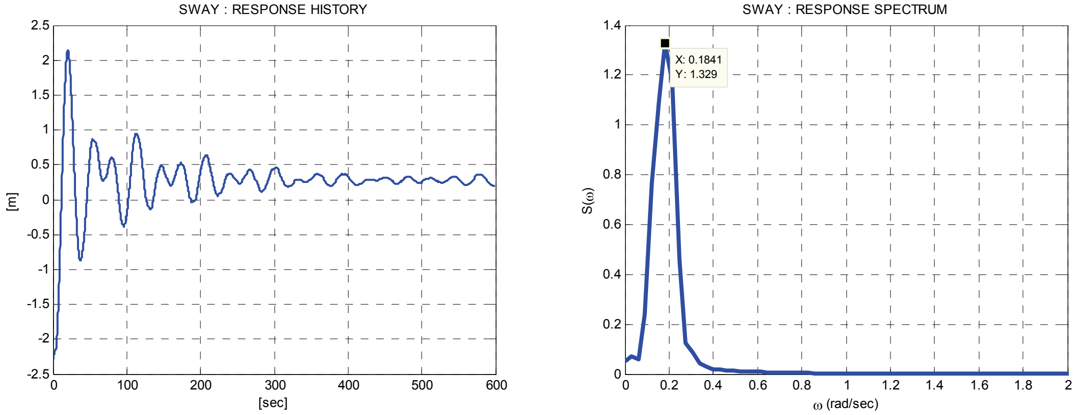

(b) Response Spectrum of Surge Free Decay Test

Figure 3.19 Experimental Free Decay Tests

In the present three-body case, only two free decay tests for the floating quay had obtained from the KORDI: free decay tests for surge and sway motions. Thus, using FFT the natural frequencies of surge and sway motions of the floating quay are obtained as shown in Fig. 3.19. As a result of the four criteria, each natural frequency of surge and sway motions for each body is assumed as given in Table 3.6.

Table 3.6 Natural Frequencies of Three-body Case

Motion		Experiment [rad/sec]	Simulation [rad/sec]
Floating Quay	Surge / Sway	0.1841 / 0.1841	0.27 / 0.27
Container Ship	Surge / Sway	0.06136 / 0.09204	0.03 / 0.03

From the assumed natural frequencies, the external stiffness is revised using the equation (3.8); the added mass at the natural frequencies are obtained from Fig. 3.7 and Fig. 3.12, and the variables are given in Table 3.7.

$$K_{Total} = K_E = \omega^2 \times (M + \Delta M_\omega) \tag{3.8}$$

As mentioned above briefly, the horizontal motions such as surge, sway, and yaw are out of the effect of K_H. Thus K_E is equal to the K_{Total}.

Table 3.7 Revised External Stiffness

Motion		ω [rad/sec]	M [kg]	ΔM_ω [kg]	K_E [N/m]
Floating Quay	Surge	0.1841	4.7273E+08	2.118E+07	1.6726E+07
	Sway	0.1841	4.7273E+08	6.441E+07	1.8191E+07
Container Ship	Surge	0.06136	2.1370E+08	7.097E+07	1.0718E+06
	Sway	0.09204	2.1370E+08	6.648E+08	7.4421E+06

Using the K_E revised as above for surge and sway motions and the external stiffness for heave same as the initial, new external stiffness matrix is calculated. The formulas to calculate the matrix of the external stiffness are based on those in Section 2.2.3.2 with the acting positions identical to the Table 3.4.

Based on the revised external stiffness matrix, three results of frequency domain analysis are updated: RAO, mean drift force, and free surface elevation. The other hydrodynamic properties such as added mass, damping coefficient and wave exciting force are free to motions of the floating.

In Fig. 3.20 and Fig. 3.21, the peak frequencies of the simulation are shifted closer to those of the experiment, especially in surge, sway, yaw motions of each body. The mean drift force/moment shown in Fig. 3.22 and Fig. 3.23 represent the change in natural frequency region. In the comparison of free surface elevation, the results are changed on the frequencies around the natural frequencies of each body, as shown in Fig. 3.24. Focusing on the RAO comparison after the stiffness revision, the results from experiments are well matched with WAMIT RAO. Thus, we can conclude two things in terms of optimization of the numerical analysis;

1. Natural frequencies are generally placed in the low frequency region for a floating structure to avoid the frequency region, where has high energy based on a general ocean wave spectrum; therefore, hydrodynamic properties around the natural frequency, the low frequencies under 0.1 rad/sec, also require to be calculated to analyze the resonance phenomenon more accurately.
2. To make a numerical modeling as exact as possible, free decay tests of experiment is required to find the natural frequency of each motion for each body; if the natural frequency is obtained from the free decay test fully, the external stiffness can be easily and exactly calculated by equation (3.7).

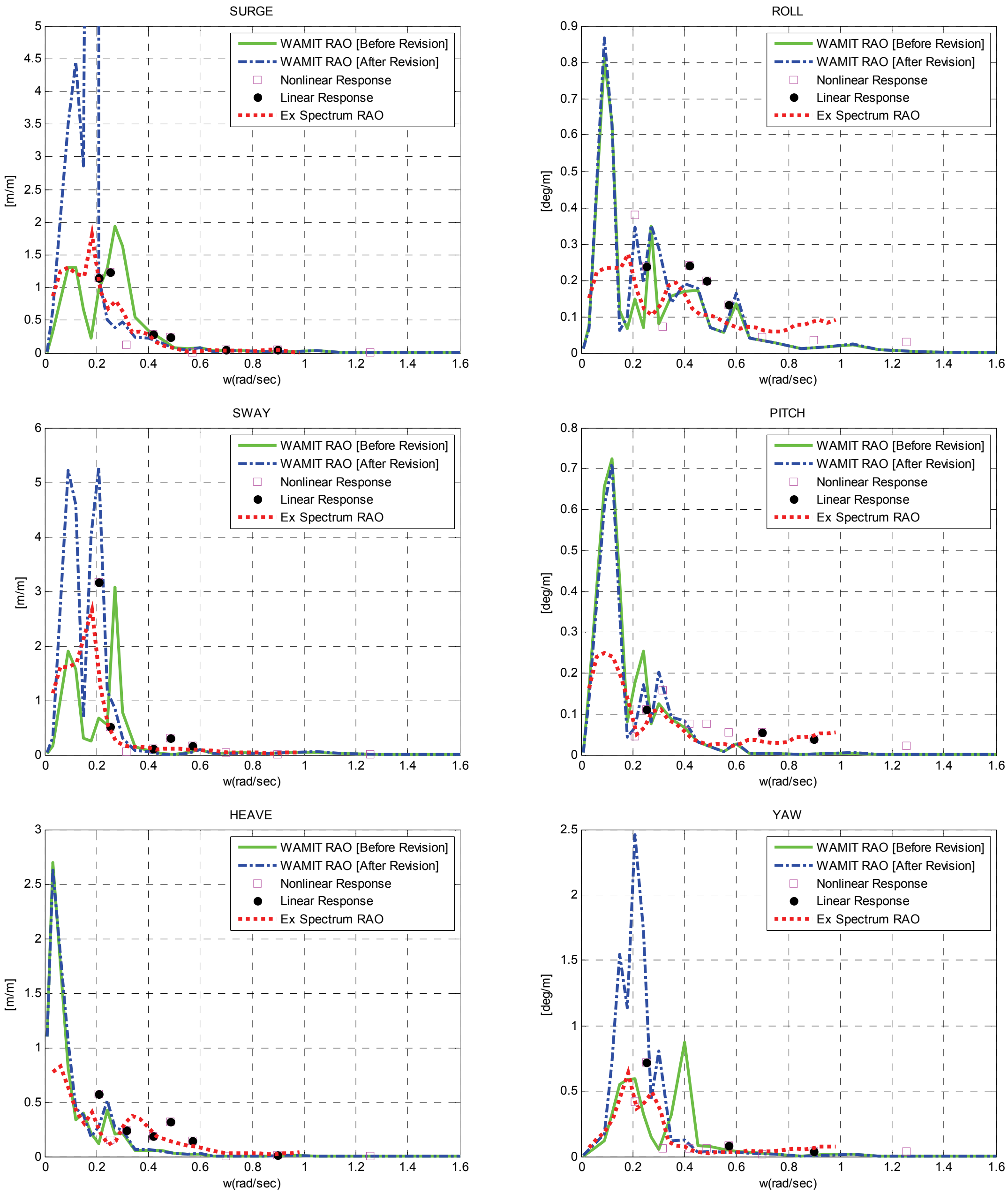

Figure 3.20 RAO Comparison of Floating Quay after Calibration I

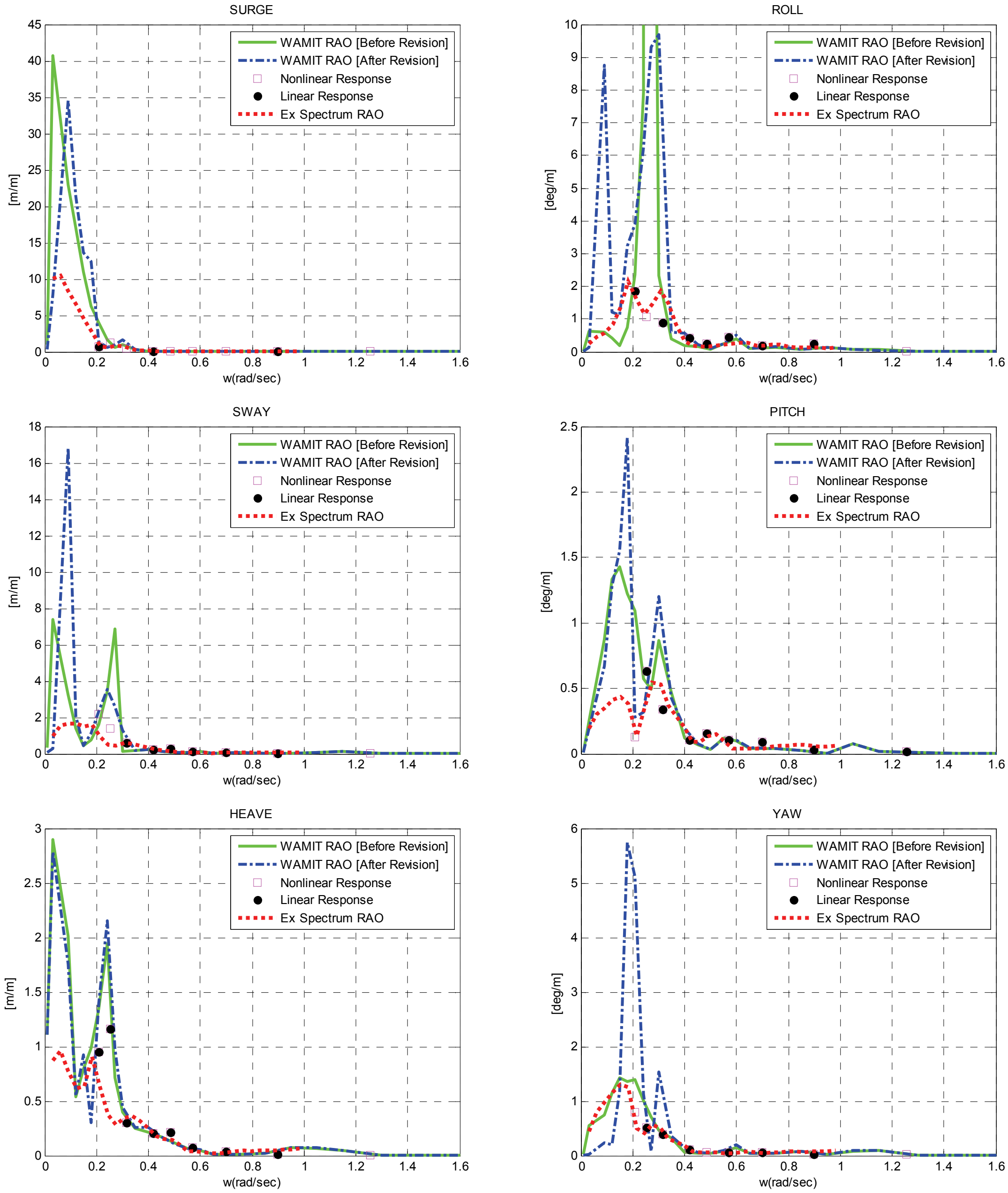

Figure 3.21 RAO Comparison of Container Ship after Calibration I

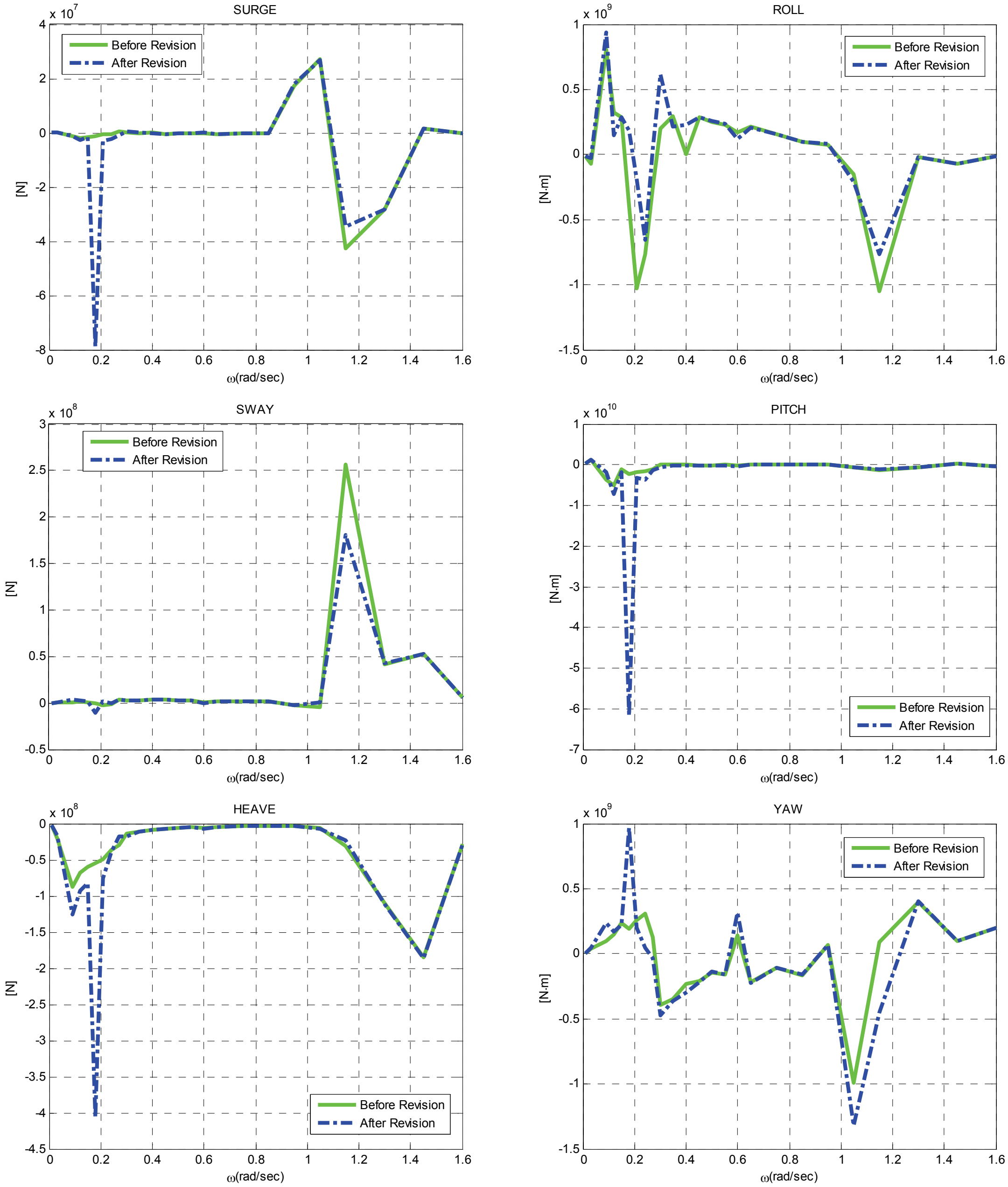

Figure 3.22 Mean Drift Force of Floating Quay after Calibration I

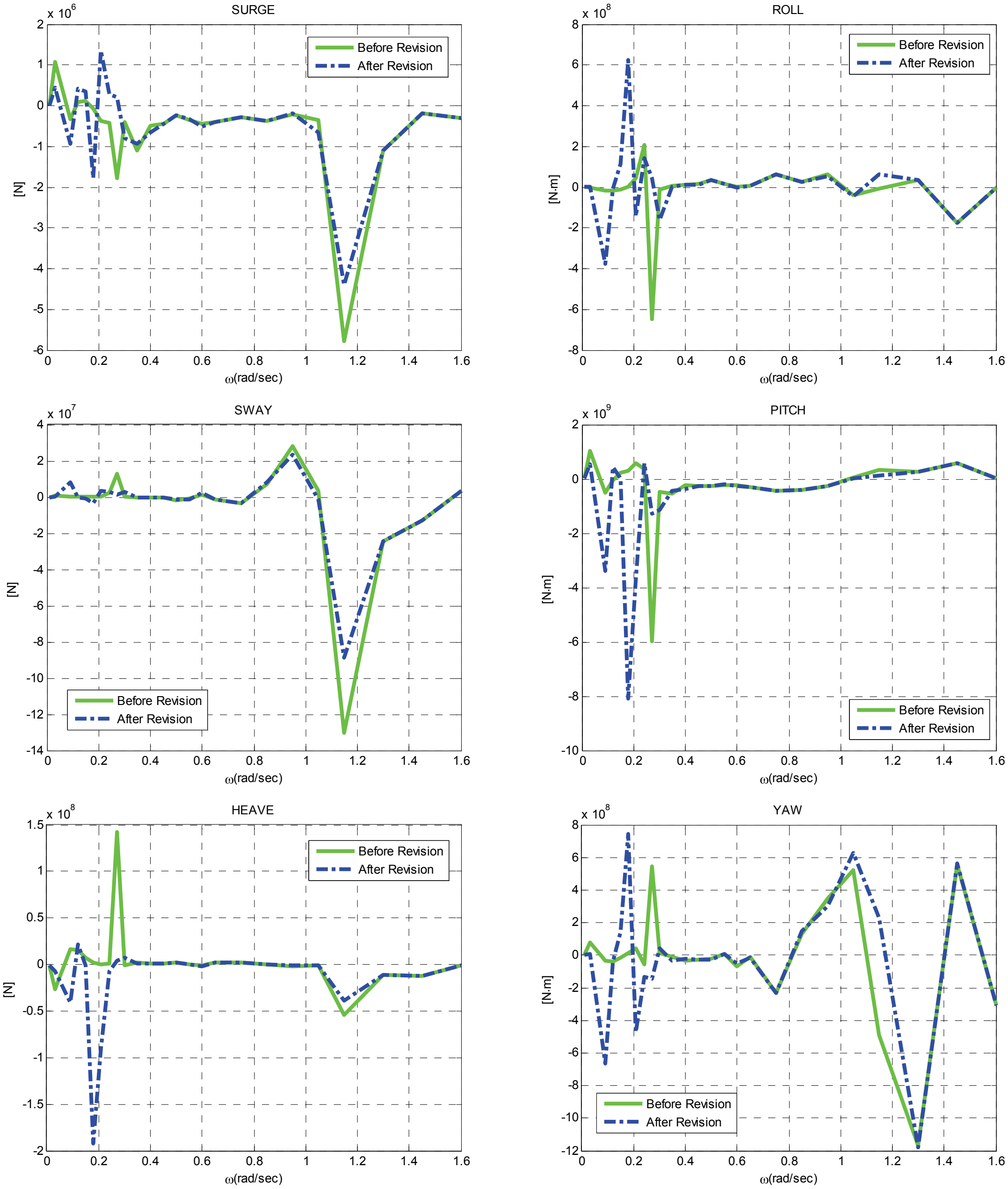

Figure 3.23 Mean Drift Force of Container Ship after Calibration I

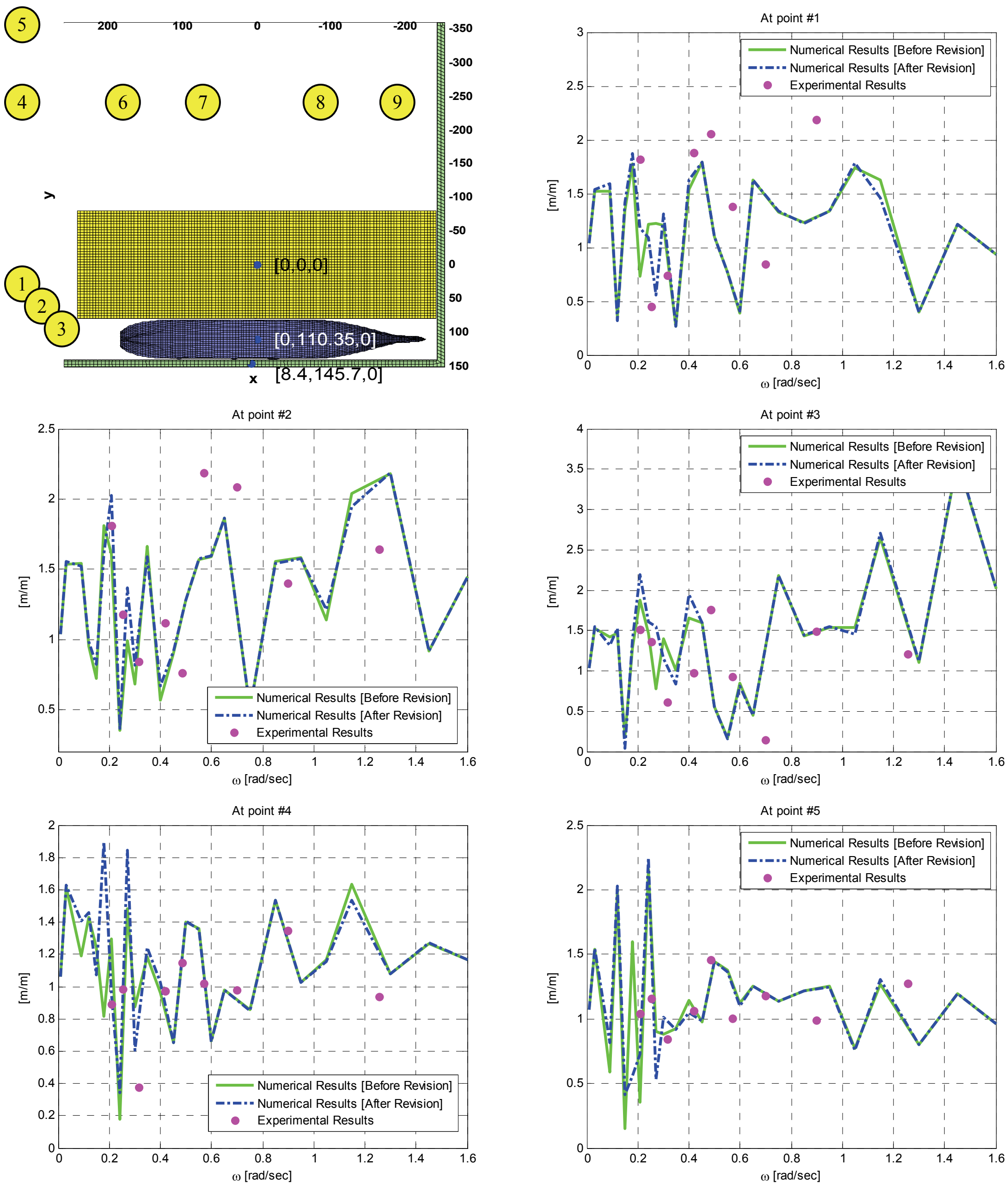

Figure 3.24 Free Surface Elevation Comparison after Calibration I

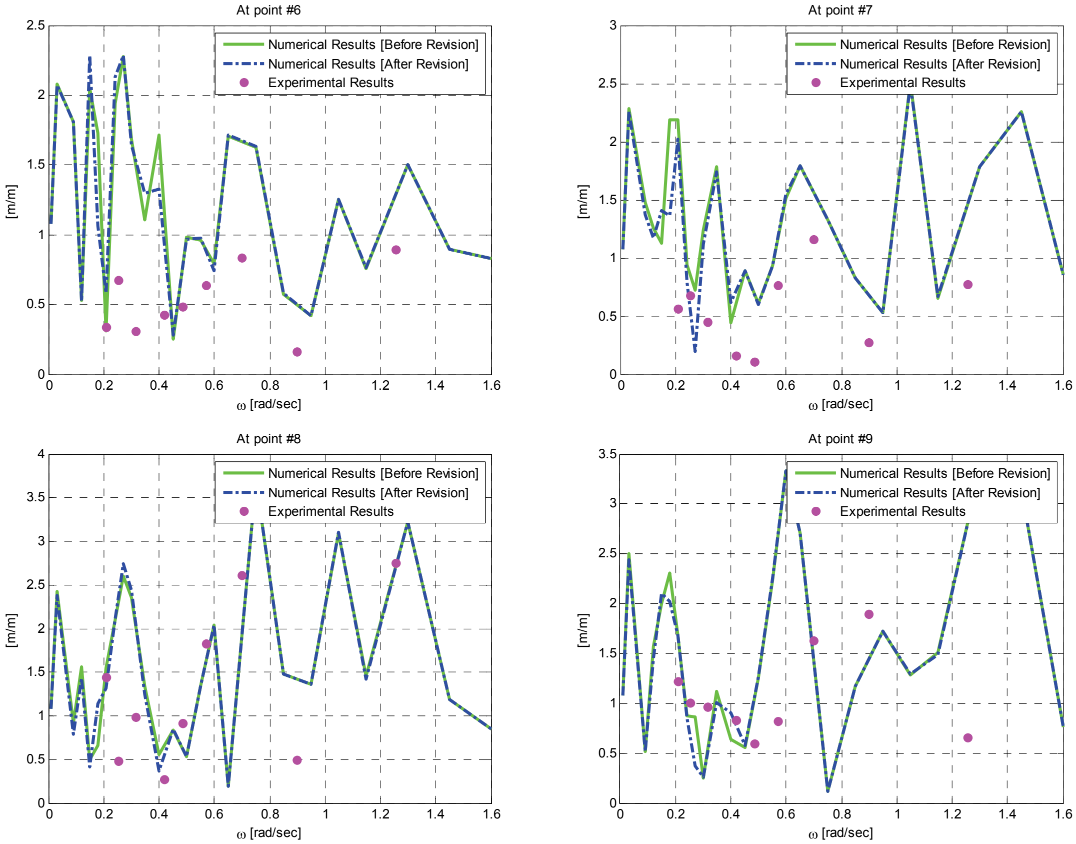

Figure 3.24 Continued

3.2.5 Smoothing Mean Drift Forces/Moments

As an additional step to optimize numerical analysis for time domain analysis in case of such multiple-body systems with side-by-side arrangement, mean drift forces/moments require certain treatments like smoothing remarkable large peaks. As mentioned in Buchner et al (2004), there exist several abnormally overestimated peaks at certain frequencies in mean drift force results, which represent pumping modes at the gaps due to absence of viscous effect in the fluid.

In this study, the exaggerated peaks are manually smoothed to make the peaks reasonably high, as shown in Fig. 3.25 and Fig. 3.26. In the present time domain analysis, the mean drift force before smoothing is used until estimation of damping, and then the smoothed mean drift force is applied to the system in order to clearly see overestimated effects of the original mean drift force.

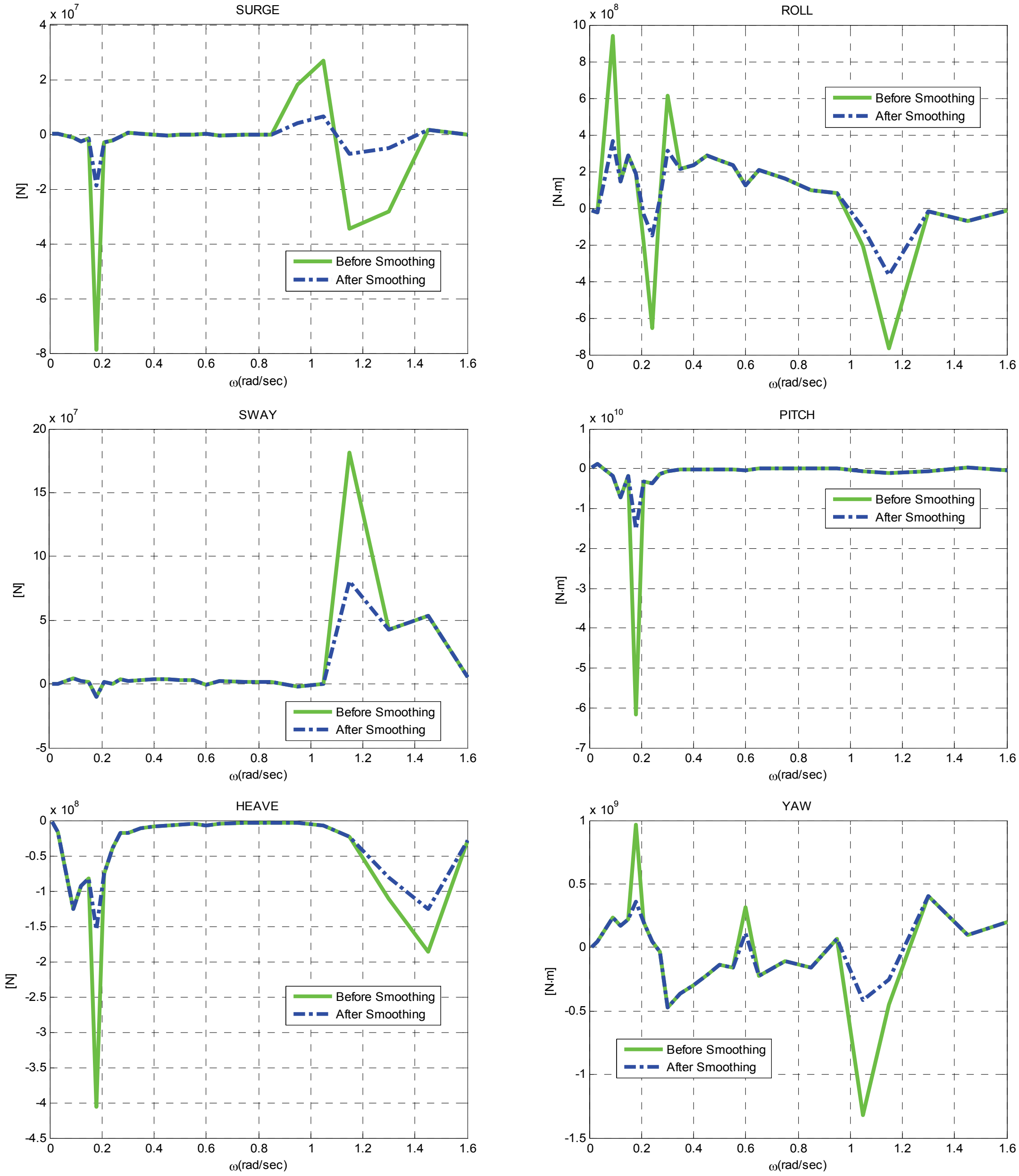

Figure 3.25 Smoothed Mean Drift Force of Floating Quay, 3-body Case

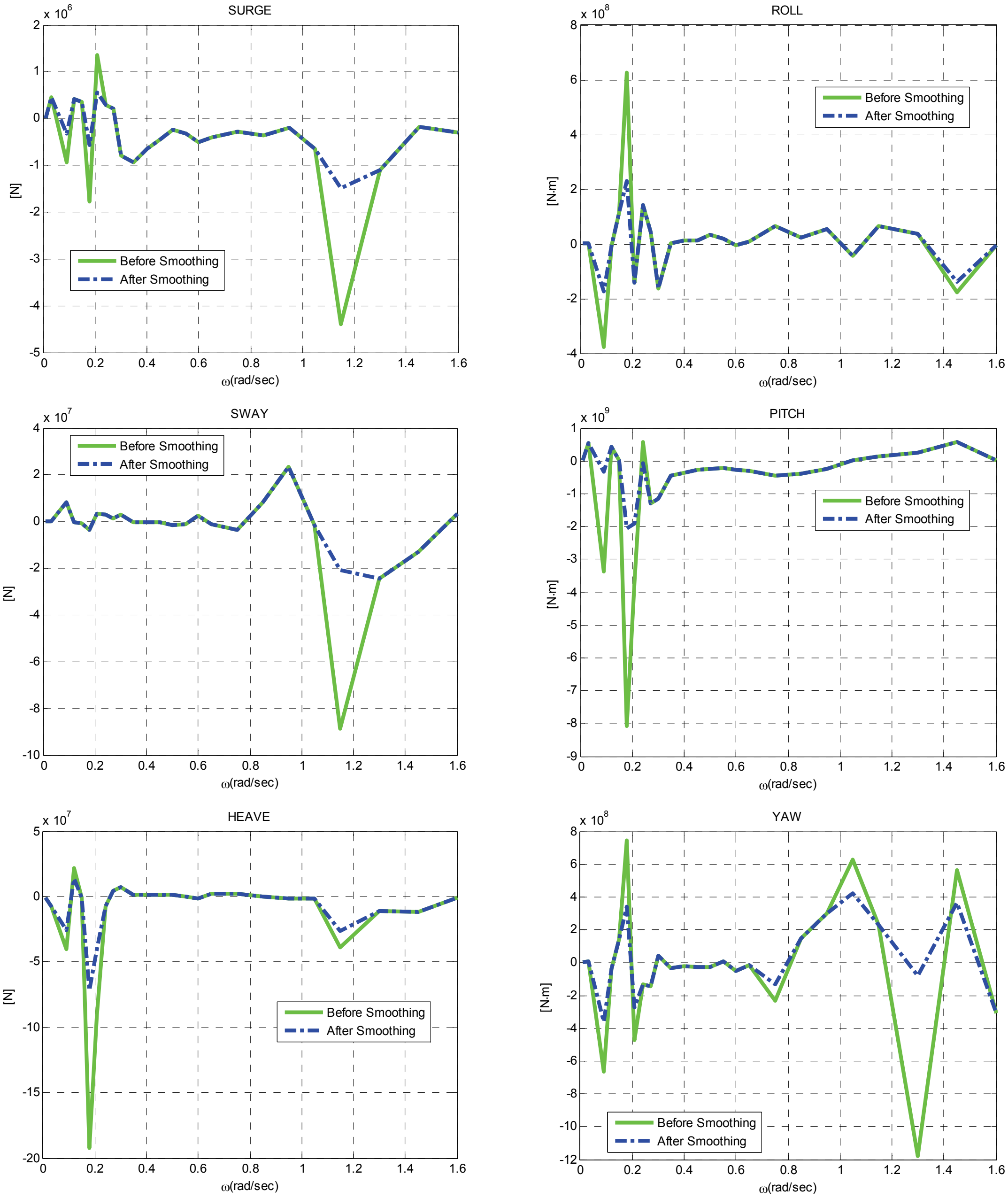

Figure 3.26 Smoothed Mean Drift Force of Container Ship, 3-body Case

3.3 Time Domain Analysis

Using CHARM3D, which is based on the theoretical backgrounds described in Section 2.3, an irregular wave test of simulation is carried out for this three-body case. To apply the second order wave force, drift force, Newman's approximation is adopted as same as the two-body case. And the total dynamic information is made of two 12×12 matrices: external mass matrix and sum of the external stiffness matrix and the hydrostatic stiffness matrix.

3.3.1 Drag Plate Information

As described in Section 2.3.2, the drag plate information is applied to account for the viscous effect of the real ocean fluid; in frequency domain, the viscosity is completely ignored since the analysis is based on the ideal fluid theory and external damping is also assumed to be zero. At the beginning stage to estimate damping force, a set of drag plate information is input to calculate the damping force using the Morison equation. The drag plates for the container ship are designed as shown in Fig. 3.27, and the input information is given by Table 3.8; those for the floating quay are identical to values of the two-body case before calibration II.

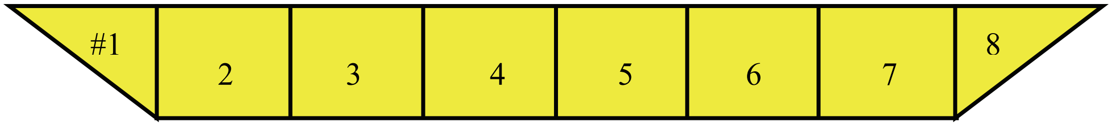

(a) Plates to x-z plane for sway

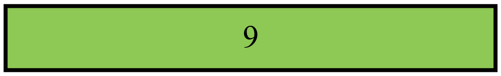

(b) Plates to y-z plane for sway

Figure 3.27 Drag Plates of Container Ship

Moreover, the damping force is estimated from the comparison of response histories between the simulation and experiment by increasing the C_D and adopting linear critical damping of roll motion, as demonstrated in Section 2.3.4.3.

Table 3.8 Drag Plates Information of Container Ship

Plate number	$\frac{1}{2}\rho A C_D$	*Center Coordinates of each drag plate*	*Unit Normal Vector*
1	403950	-187.67, 0, -4.67	0, 1, 0
2	807905	-140.75, 0, -7	0, 1, 0
3	807905	-84.45, 0, -7	0, 1, 0
4	807905	-28.15, 0, -7	0, 1, 0
5	701715	24.45, 0, -7	0, 1, 0
6	701715	73.35, 0, -7	0, 1, 0
7	701715	122.25, 0, -7	0, 1, 0
8	350860	163.00, 0, -4.67	0, 1, 0
9	803600	0, 0, -7	1, 0, 0

3.3.2 Sea State

For this three-body case, the KORDI carried out the experiment of only one irregular wave test, which is same as the two-body case. Thus, at this step, the same irregular wave test in Table 3.9 is simulated to examine the survivability of this three-body system. And as a set of additional case study, the operability is also investigated by input of less severe sea state conditions, after finishing the second calibration process.

Table 3.9 Sea State of 3-body Case

Sea state	*Identified Values*
Wave Spectrum Type	Bretschneider-Mitsuyatsu Spectrum
Significant Wave Height (H_S) [m]	2.8
Peak Period (T_P) [sec]	15.5
Wave Frequency Region [rad/sec]	0.25 ~ 1.5
The Number of Incident Waves	126

Contrary to the two-body case, not only currents but also wind forces are ignored in the experiment, and thus those are not accounted in time domain simulation.

3.3.3 Response History Comparison

In the previous sections, the input to perform the irregular wave test of simulation has been prepared from the experiment. The simulation is conducted for about 1 hour 40 min, and the time interval for each step is 0.05 sec.

3.3.3.1 Confirmation of Time Domain Results

To check reliability of the numerical analysis as described in Section 2.3.4.1, CHARM3D spectrum RAO's calculated from the response histories are compared with a set of WAMIT RAO's. At this point, we should take notice that this time domain results is obtained from inputs identical to the inputs of the frequency domain analysis; meanwhile, the irregular wave test, which is prepared in Section 3.3.1 to 3.3.2, is identified from the experiment. Thus, two inputs are excluded to implement a new irregular wave test to compare with WAMIT RAO: the drag plate information and drifts forces/moments.

FFT is tuned to make incident wave spectrum, which is calculated from wave elevation measured in CHARM3D, matched with the theoretical wave spectrum, as shown Fig. 3.28.

The RAO comparison between CHARM3D Spectrum RAO and WAMIT RAO show good agreement. Fig. 3.29 and Fig. 3.30 represent the RAO comparison of the floating quay and container ship, respectively; the CHARM3D Spectrum RAO is indicated as CHARM3D RAO in the figures.

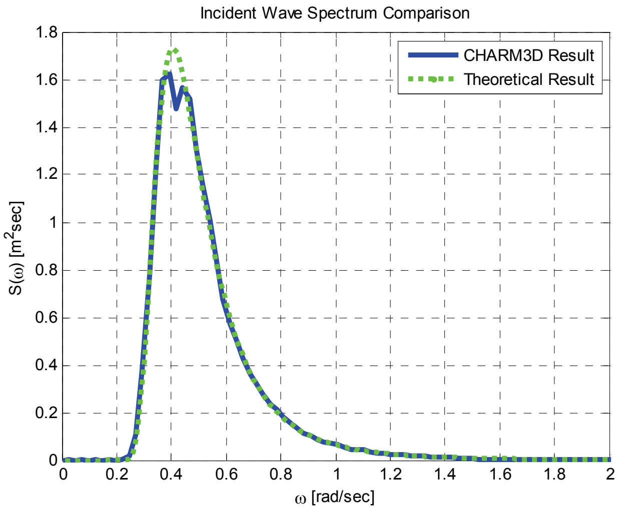

Figure 3.28 Comparison of Incident Wave Spectra in Simulation, 3-body Case

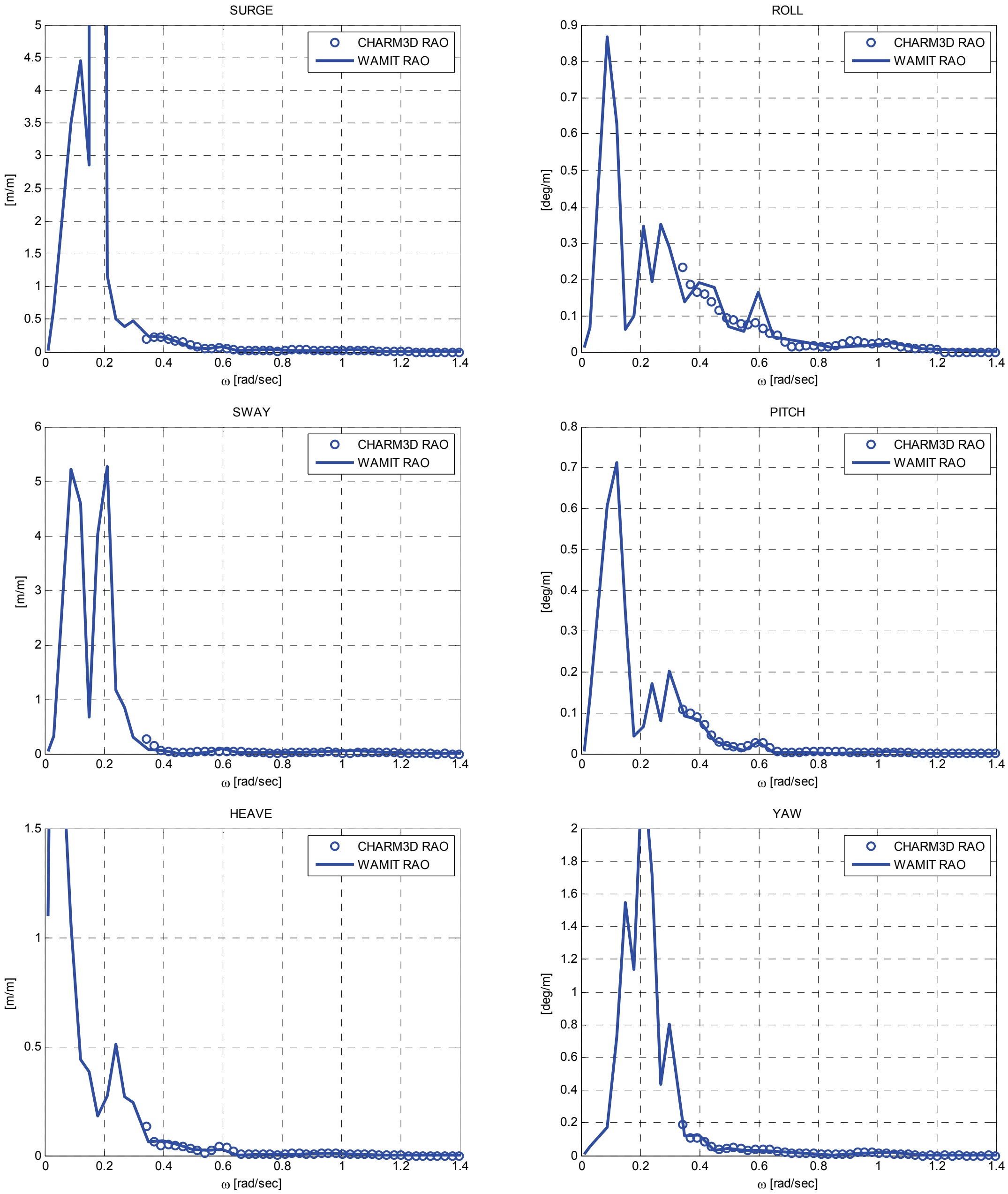

Figure 3.29 RAO Comparison between Time Domain and Frequency Domain of Floating Quay, 3-body Case

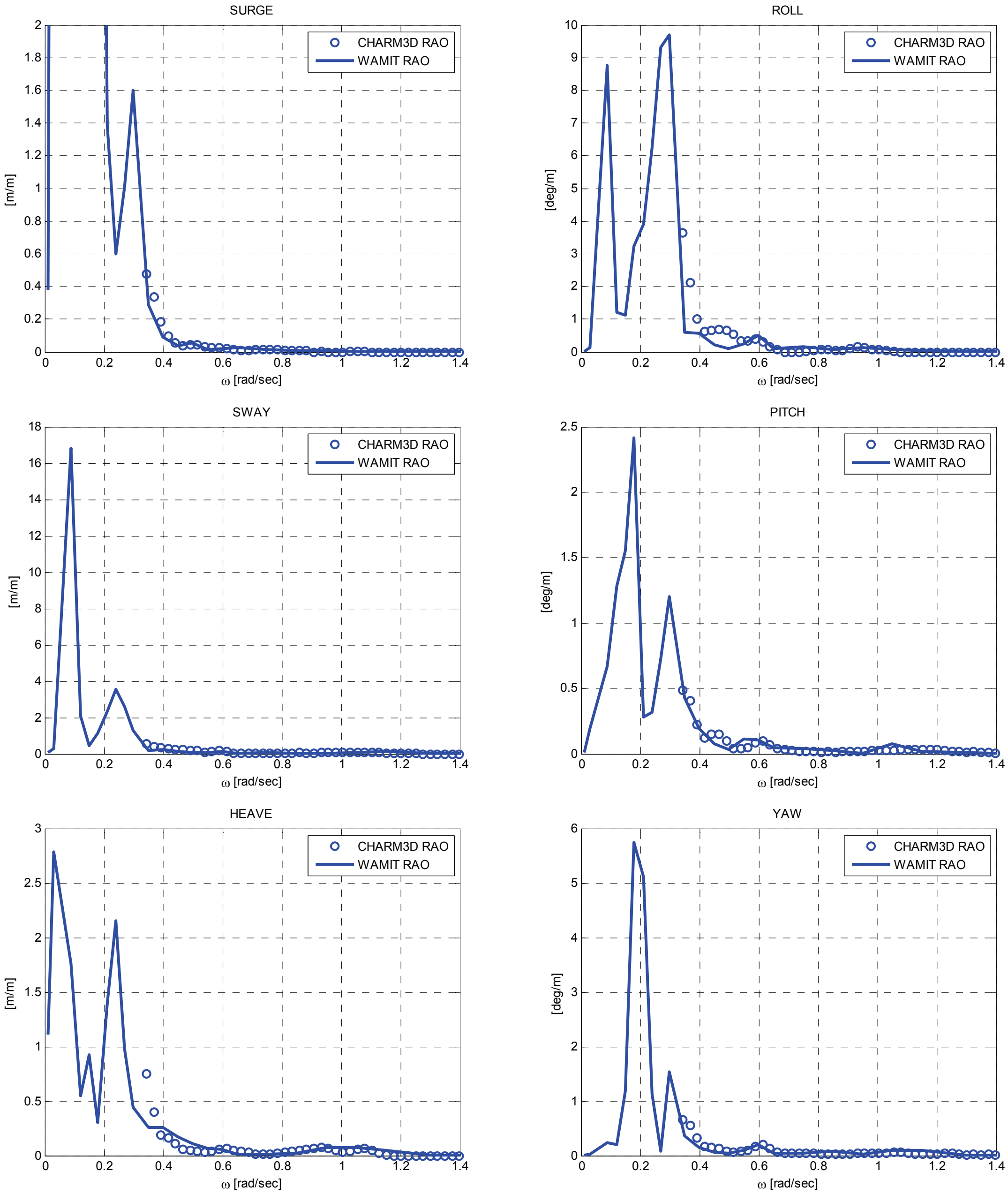

Figure 3.30 RAO Comparison between Time Domain and Frequency Domain of Container Ship, 3-body Case

3.3.3.2 Comparison of Responses with Experiment

In same manner in the two-body case, each coordinate system in Fig. 3.31 should be indentified between the experiment and numerical analysis before the comparison of the response histories.

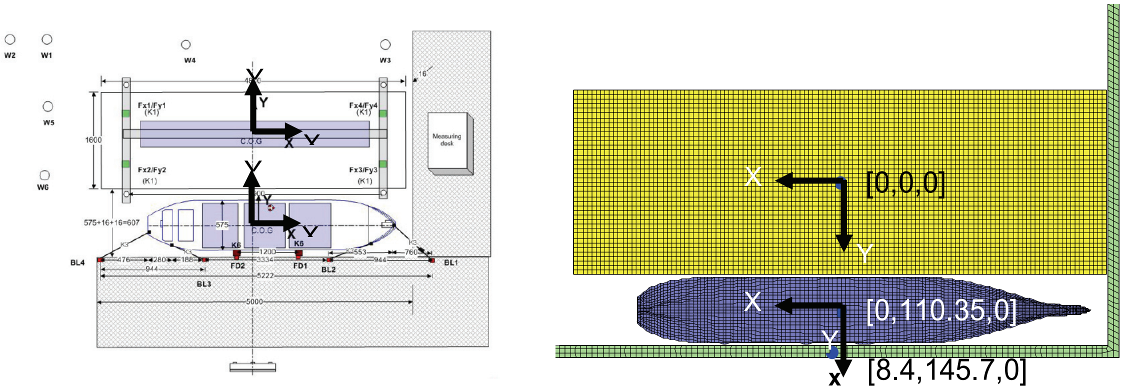

Figure 3.31 Coordinate System Comparison between Experiment and Simulation, Three-body Case

As same with the two-body case, coordinate systems of the experiment have opposite directions of x and y coordinates, and they have z coordinate offsets: 0.14m for the floating quay and 9.2m for the container ship.

The coordinate systems of the experiment are transformed to those of the simulations using equation (2.25) and (2.26). After the transformation, the response histories of the experiment are shown in Fig. 3.32 and Fig. 3.33.

After this identification of the coordinate system, the response histories of the simulation, which are the results of the initial damping force, are compared with those of the experiment in Fig. 3.34 and Fig. 3.35.

From the differences in the response comparisons, damping is calibrated and smoothed drift force is applied to the system.

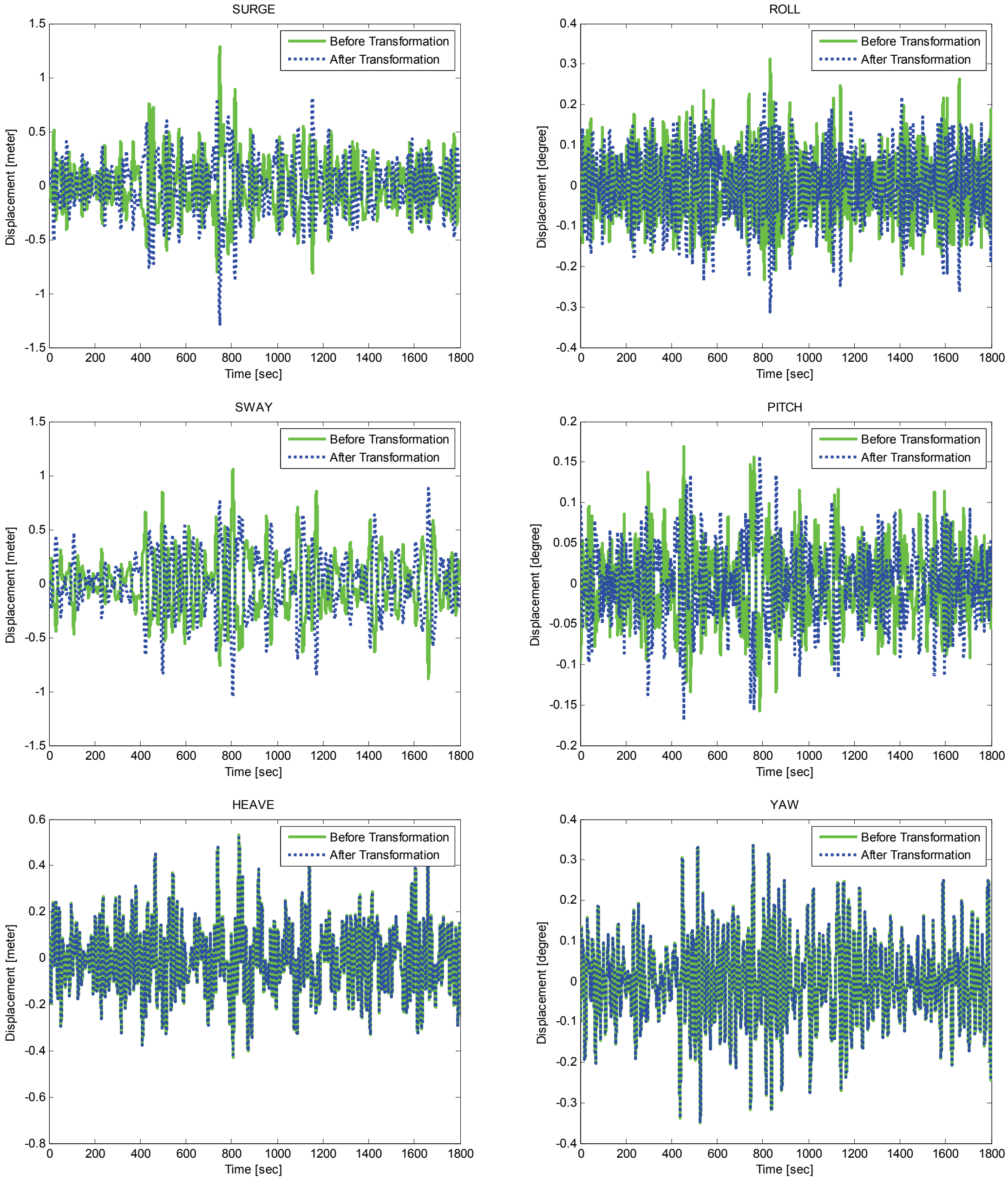

Figure 3.32 Floating Quay’s Responses of Experiment after Coordinate Transformation, 3-body Case

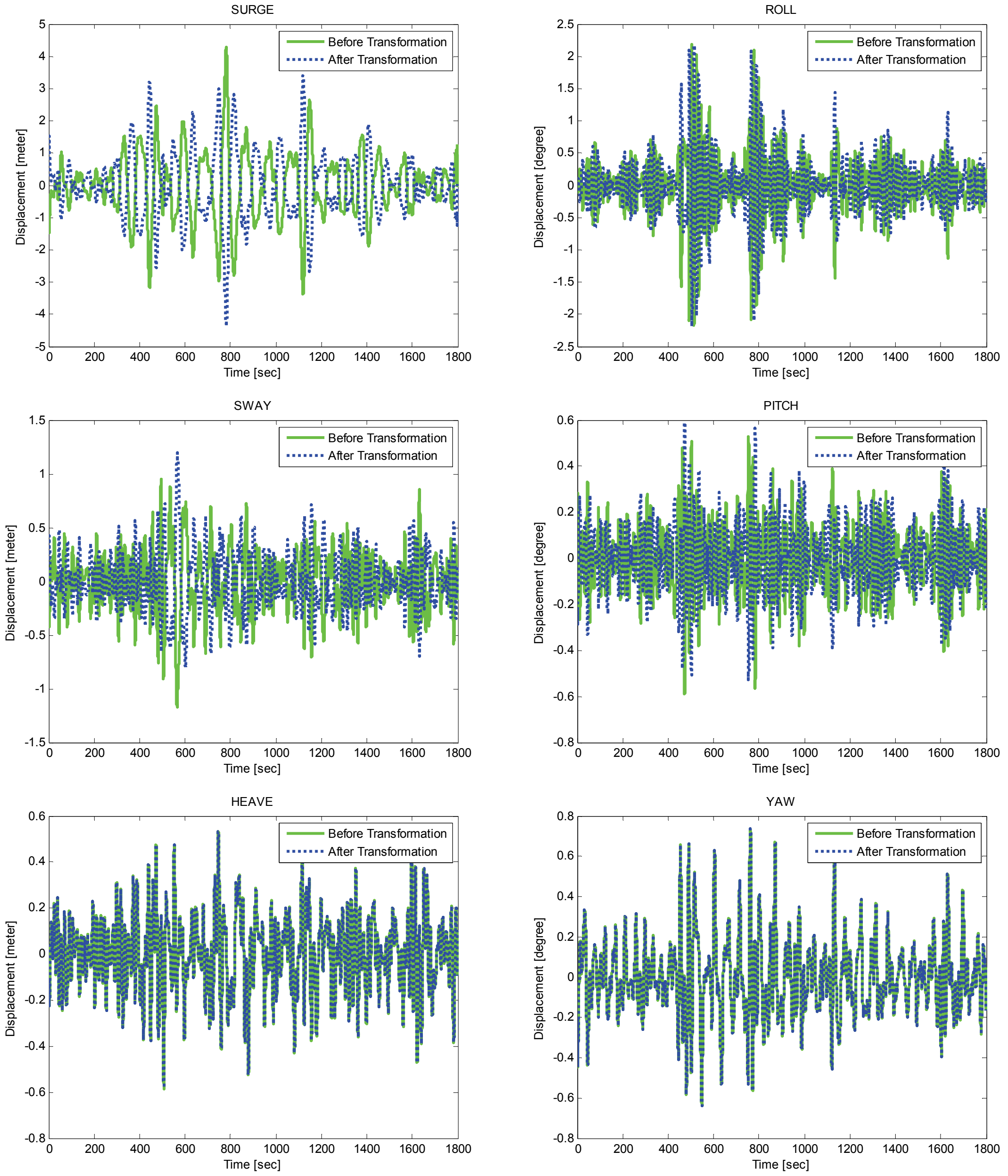

Figure 3.33 Container Ship's Responses of Experiment after Coordinate Transformation, 3-body Case

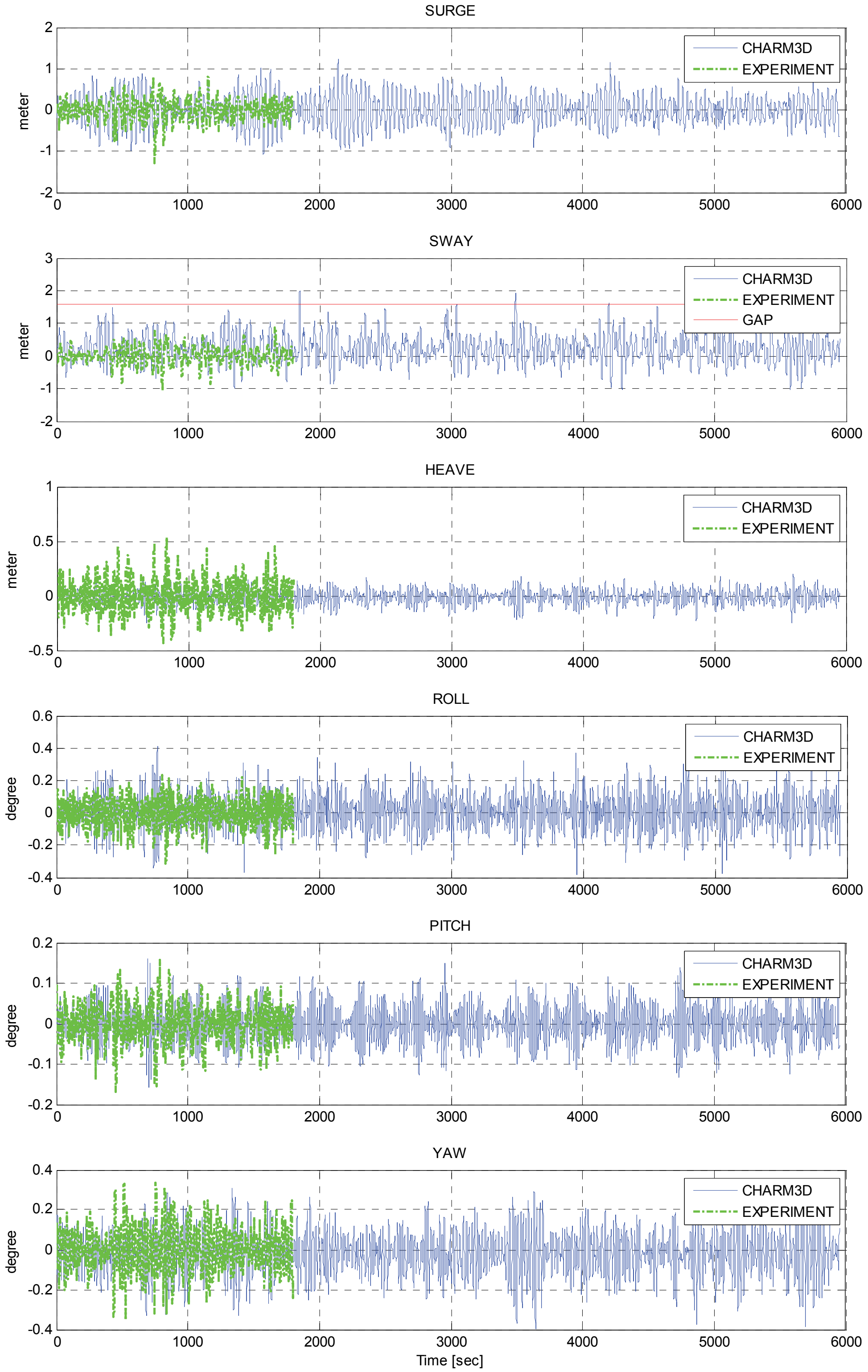

Figure 3.34 Comparison of Response Histories for Floating Quay, 3-body Case

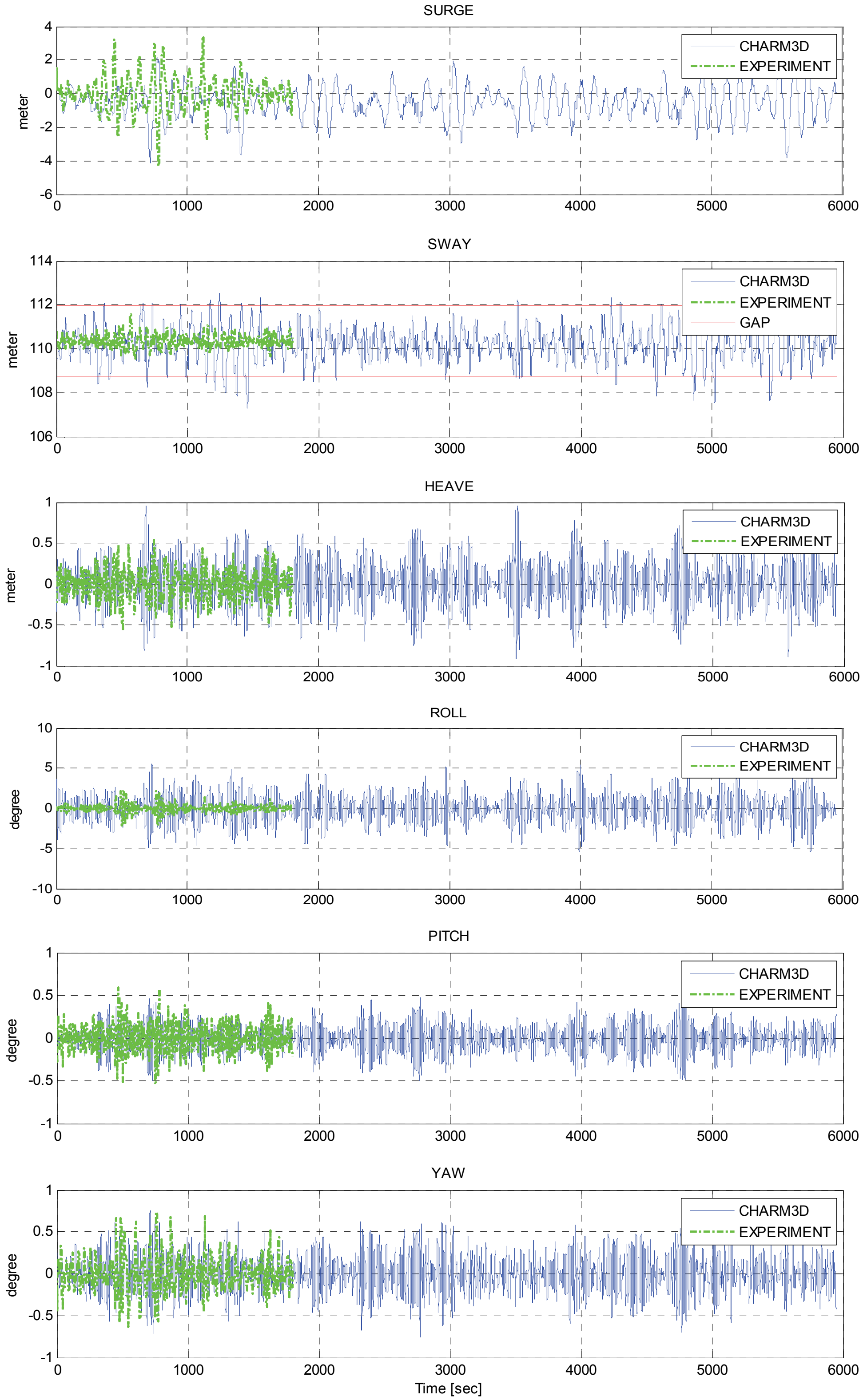

Figure 3.35 Comparison of Response Histories for Container Ship, 3-body Case

3.3.3.3 Calibration II: Damping Force Estimation

By comparison of the response histories, at first the motions, which have narrow gap effects, have overestimated responses to the numerical analysis; for example, surge and sway motions of the floating quay show almost one and a half times larger responses than those of experiment. In case of the container ship, only sway motion has exaggerated response as much as almost two times than the experiment. Thus, the drag coefficients C_D are changed to 6 for the surge and sway of the floating quay and 8 for the sway of the container ship; the values are empirically obtained by comparison of a series of irregular wave test simulation.

Next, roll motions of the two bodies should be corrected using the extra damping coefficient. In this study, for the extra roll damping, a critical damping coefficient is applied, as described in Section 2.3.4.3; the exaggerated roll motion is a well-known phenomenon in a general numerical analysis, which is caused by underestimated radiation roll damping.

From the comparisons of the roll motions between the simulation and experiment, the container ship has larger difference than the floating quay; it is largely due to effects of the bilge keel with gap effects on the both sides of the container ship (Chakrabarti 2001 and Buchner et al. 2004). Thus, 20% of critical roll damping for the container ship is applied to this three-body system, and 5% of the critical damping for the floating quay is used like the two-body case.

The revised damping inputs of the floating quay are same as the values in Section 2.3.4.3, and those of the container ship are summarized in Table 3.10 and 3.11.

Table 3.10 Roll Damping Coefficient; Container Ship

α	ω_{roll} [rad/sec]
20%	0.3068

The natural frequency of the roll motion is picked in the same manner with the floating quay case such that in roll RAO comparison of the container ship a peak placed out of the low frequency region and not appeared in the other motions remarkable is assumed to be a resonance peak.

Table 3.11 Calibration of Damping Force Inputs; Container Ship

Plate number	$\frac{1}{2}\rho AC_D,\ \ C_D = 2$	$\frac{1}{2}\rho AC_D,\ \ C_D = 8, 2$
1	403950	1610000
2	807905	3230000
3	807905	3230000
4	807905	3230000
5	701715	2810000
6	701715	2810000
7	701715	2810000
8	350860	1400000
9	803600	803600

Results to the revised damping inputs are shown in Fig. 3.36 to Fig. 3.39. From the comparison after the second calibration general motions except for the heave of the floating quay show good agreement with experiment results; all the responses are somewhat decreased due to the increased damping forces/moments.

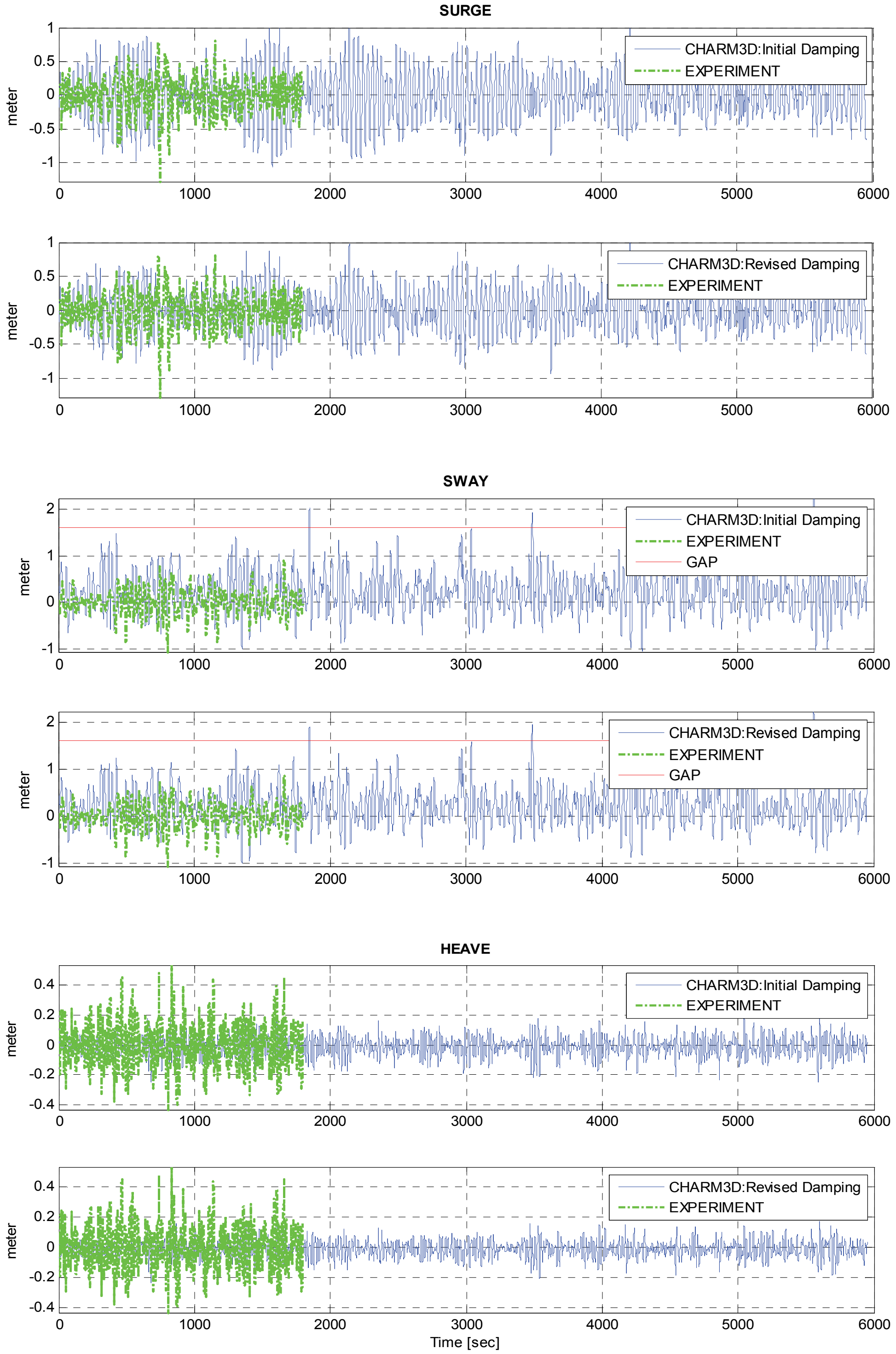

Figure 3.36 Comparison of Response Histories of Floating Quay after Calibration II, 3-body Case: Surge, Sway, and Heave

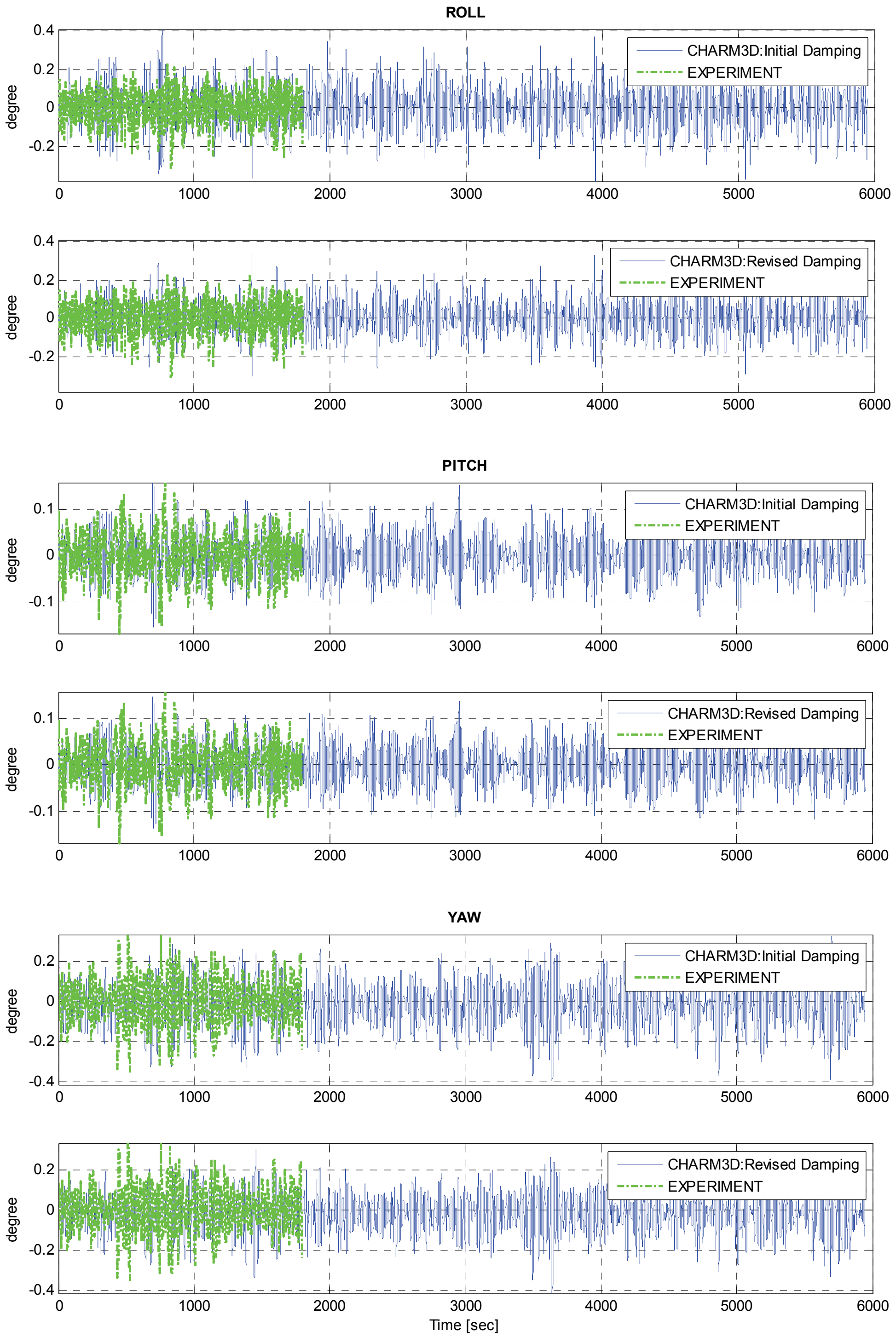

Figure 3.37 Comparison of Response Histories of Floating Quay after Calibration II, 3-body Case: Roll, Pitch, and Yaw

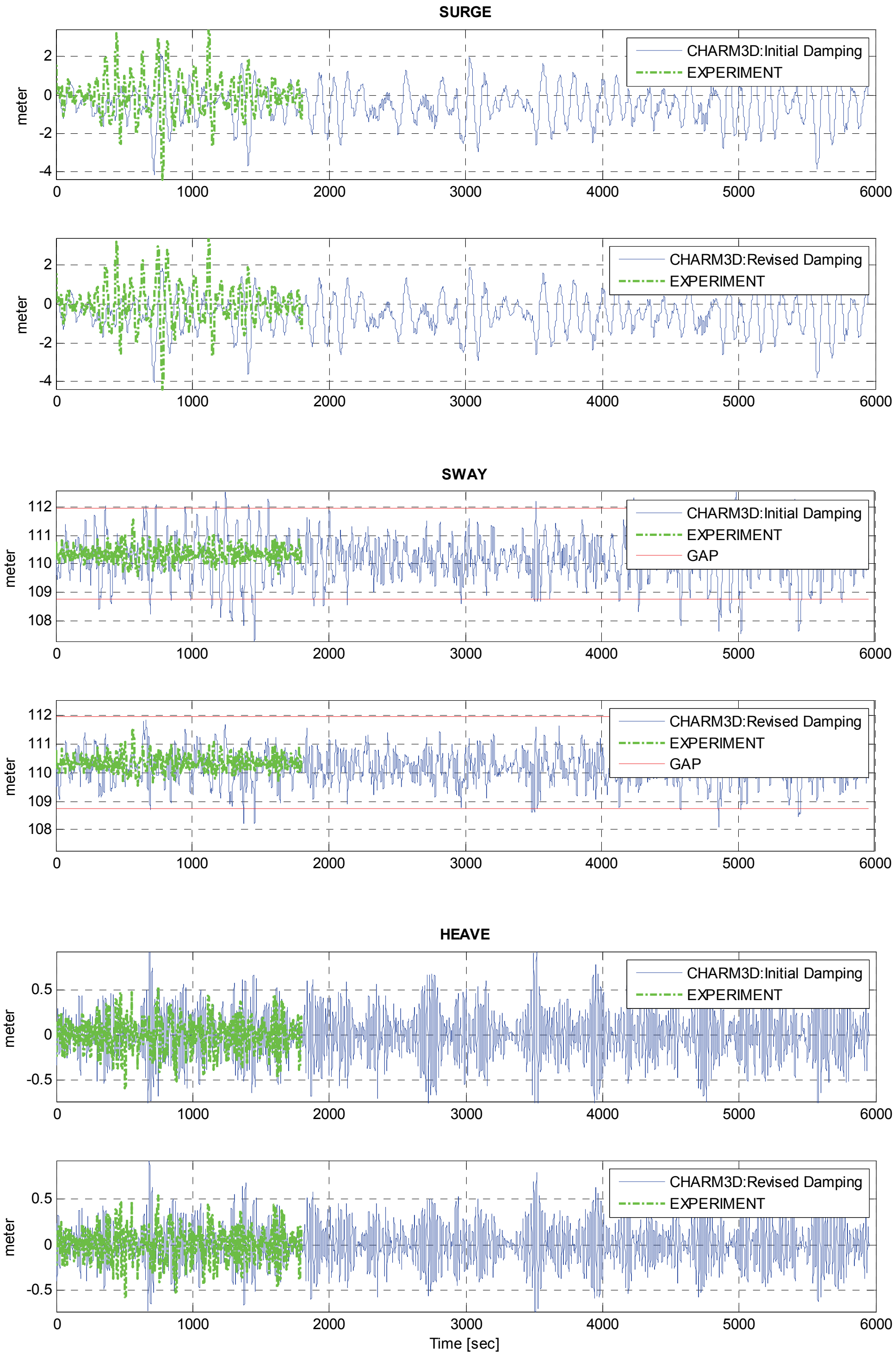

Figure 3.38 Comparison of Response Histories of Container Ship after Calibration II, 3-body Case: Surge, Sway, and Heave

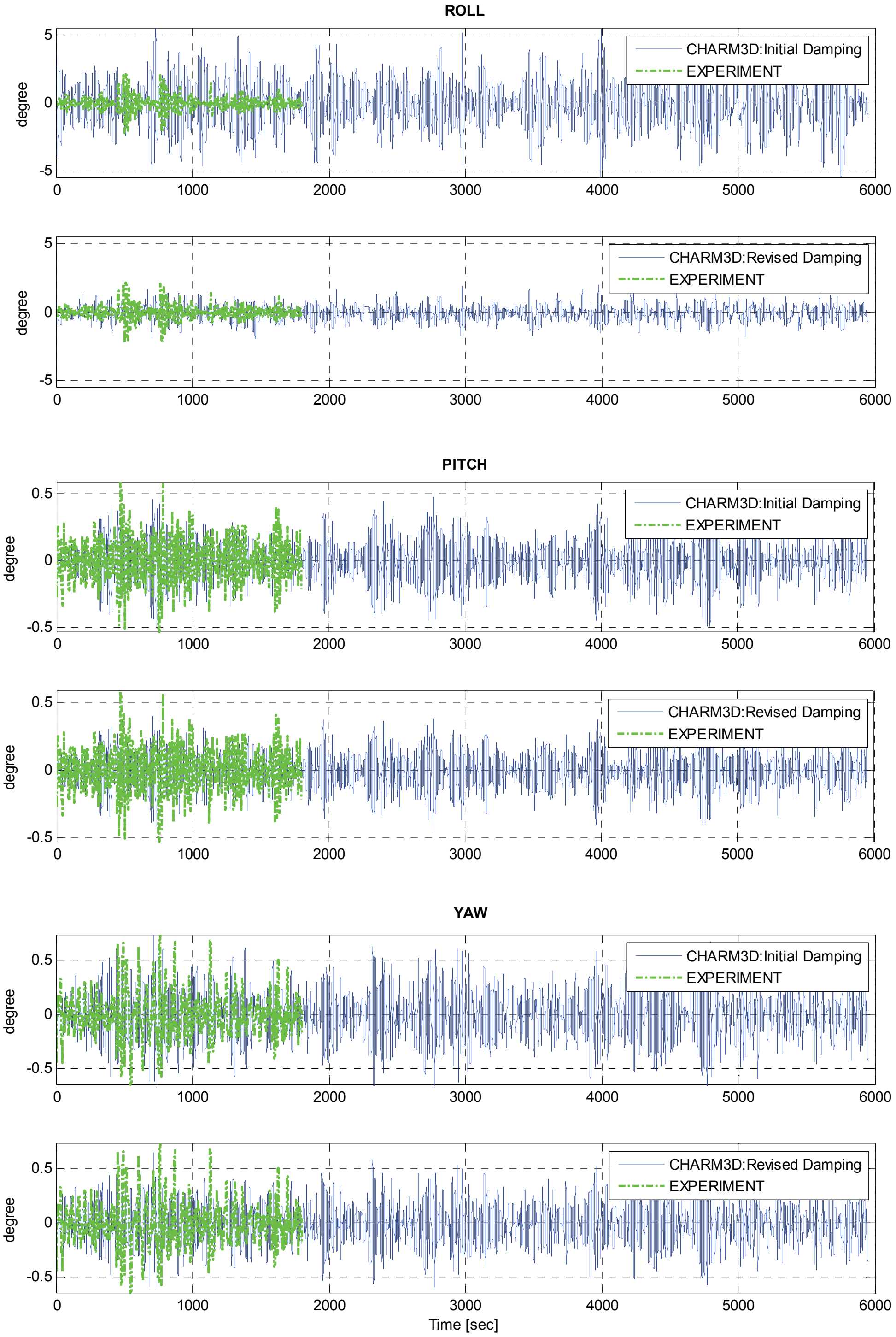

Figure 3.39 Comparison of Response Histories of Container Ship after Calibration II, 3-body Case: Roll, Pitch, and Yaw

3.3.3.4 Overestimated Drift Force and Treatment

Despite two calibration processes, external stiffness revision and damping estimation, the horizontal responses like surge, sway of the floating quay and sway of the container ship still show somewhat differences between experiment and simulation. As mentioned in Section 3.2.5, it is largely due to overestimated drift forces at pumping mode frequencies.

Thus, at this point the original drift forces/moments input is altered to the smoothed drift forces/moments inputs in Fig. 3.25 and Fig. 3.26; all the other inputs are fixed as developed so far to see the effects only by drift forces/moments.

After input of the smoothed drift forces/moments the renewed responses are compared in Fig. 3.40 to Fig. 3.43. The comparisons of statistics are given in Table 3.12 and 3.13. In addition, total RAO comparisons, which include the updated CHARM3D RAO, are plotted in Fig. 3.44 and Fig. 3.45.

In terms of limits of motions, the floating quay still has responses over the limit for surge and sway motions, 0.48 meter, in both of simulation and experiment even though surge and sway of the floating quay and sway of the container ship are quite decreased after smoothing drift forces/moments. In the meantime, heave, pitch, and yaw motions of the floating quay for both the experiment and the simulation are in the limits, 0.8 meter, 1 degree, and 1 degree, respectively.

Meanwhile, in roll motion the response to the experiment is within the limit, 3 degree, but the response to the numerical analysis has several peaks of the limit. In this regard, it is seen that uncertain energy dissipation in the experimental system caused the underestimated response.

In case of the container ship, the limits of the responses are considered to be same as the values of the floating quay except for surge and sway motions; the limit for surge is assumed to be 1m, and that for sway is assumed to be 0.6m. Based on the limits, surge and sway of both simulation and experiment have responses out of the limits, and a couple of peaks in heave motion of the numerical analysis are out of the limit. Meanwhile, all the other responses are within each limit.

To conclude, because of the severe sea state conditions there exist certain peaks out of each limit in terms of comparisons of the responses not only for simulation but also for experiment.

Thus, to see the operability of the floating harbor system, additional numerical analysis is required; for instance, an operating sea state condition is input to the simulation, which is optimized to the relevant experiment so far.

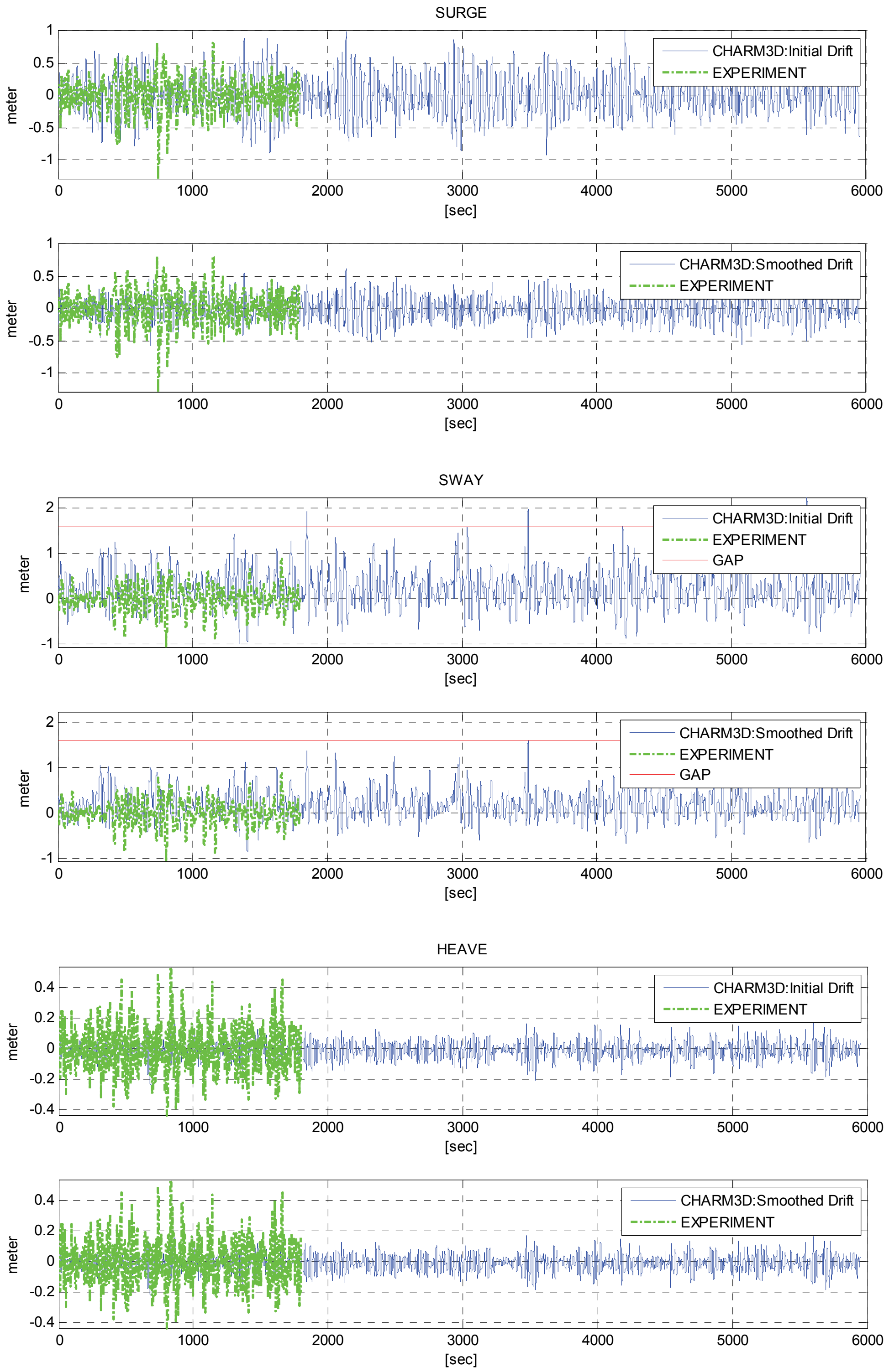

Figure 3.40 Comparison of Response Histories of Floating Quay after Smoothing Drift Force, 3-body Case: Surge, Sway, and Heave

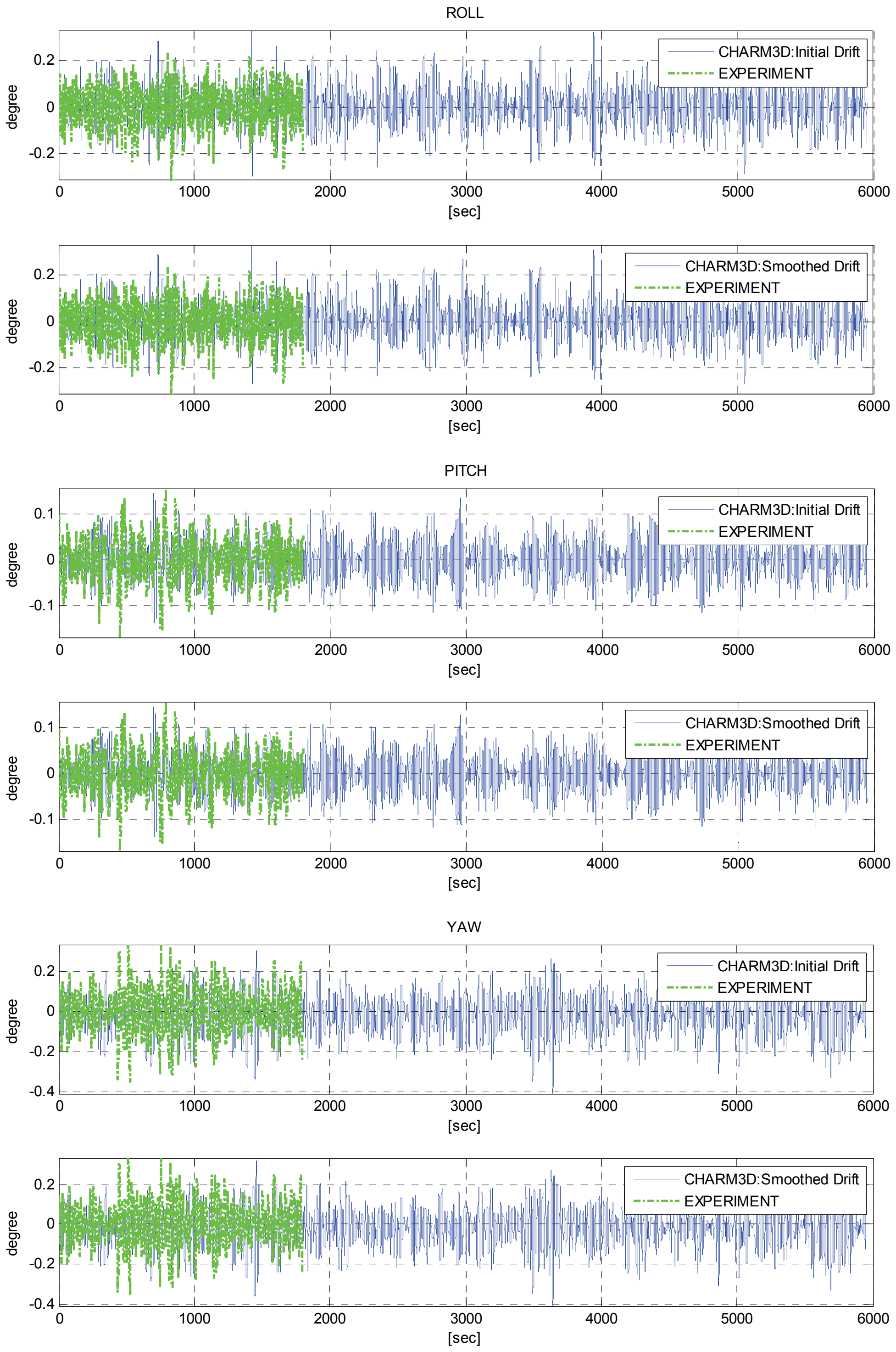

Figure 3.41 Comparison of Response Histories of Floating Quay after Smoothing Drift Force, 3-body Case: Roll, Pitch and Yaw

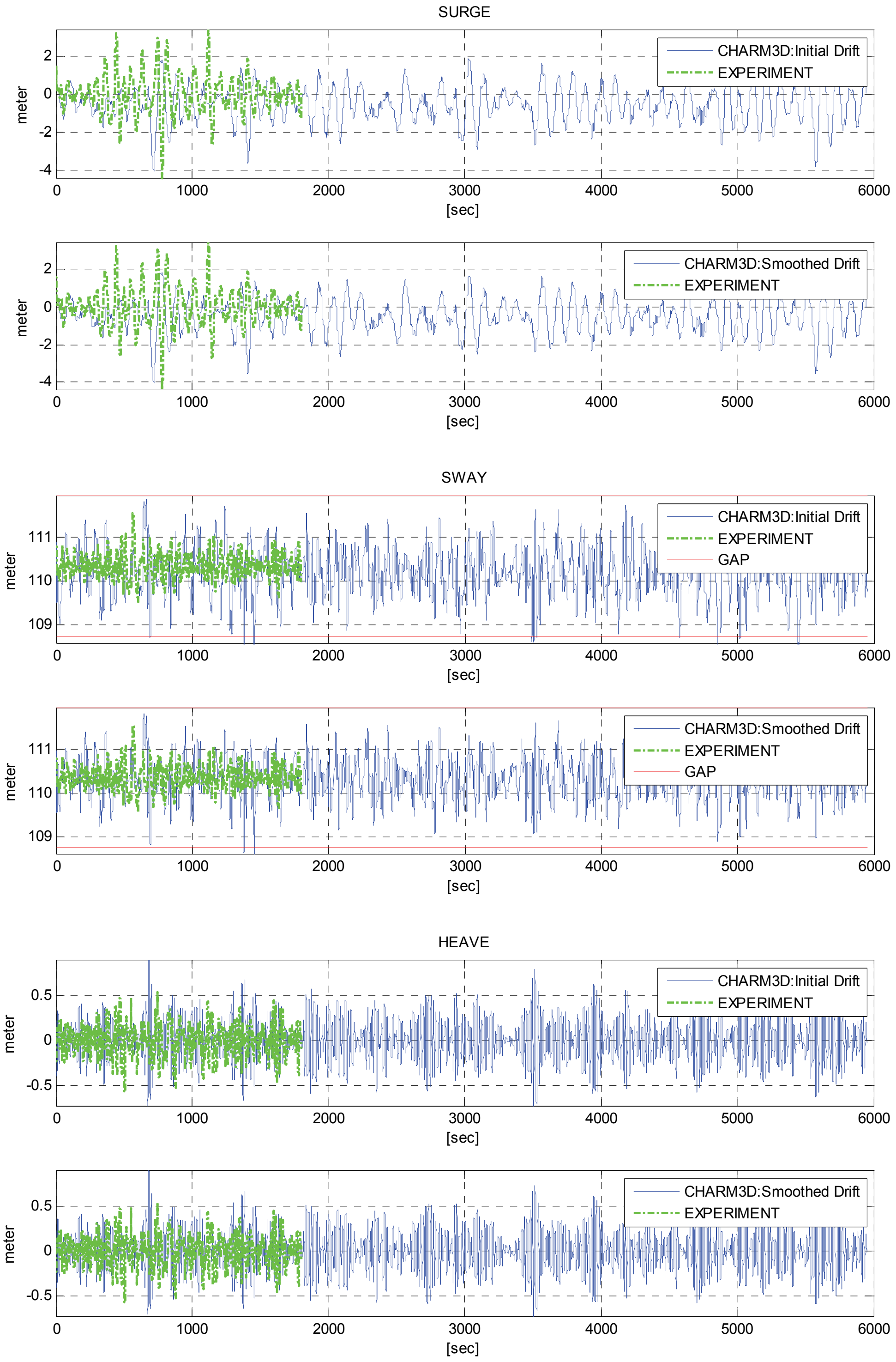

Figure 3.42 Comparison of Response Histories of Container Ship after Smoothing Drift Force, 3-body Case: Surge, Sway, and Heave

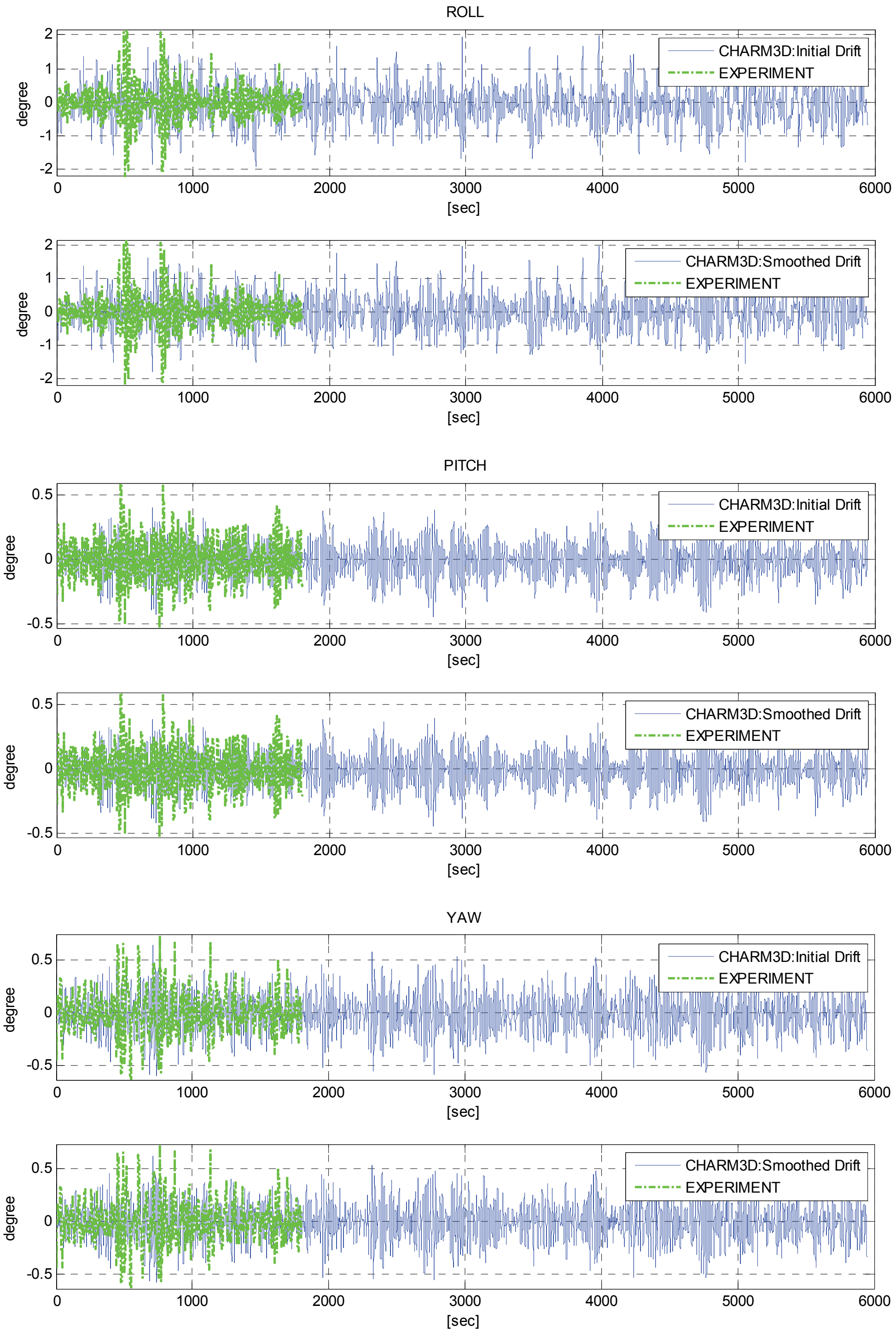

Figure 3.43 Comparison of Response Histories of Container Ship after Smoothing Drift Force, 3-body Case: Roll, Pitch and Yaw

Table 3.12 Statistics of Responses; Floating Quay of 3-body Case

Motion	*Mean*	*RMS*	*STD*	*Max*	*Min*
Surge [m]	-0.001 -0.006 (0.0)	0.2939 0.1733 (0.2559)	0.2939 0.1732 (0.2559)	1.01 0.6133 (0.8121)	-0.9347 -0.5857 (-1.288)
Sway [m]	0.2402 0.1966 (0.0)	0.4646 0.3622 (0.2729)	0.3977 0.3043 (0.2729)	2.225 1.905 (0.8835)	-0.9868 -0.8502 (-1.052)
Heave [m]	-0.0111 -0.0107 (0.0)	0.0549 0.0529 (0.1471)	0.0538 0.0518 (0.1471)	0.1728 0.1701 (0.5324)	-0.2339 -0.2177 (-0.4301)
Roll [deg]	0.0074 0.0070 (0.0)	0.0846 0.0824 (0.08297)	0.0842 0.0821 (0.08297)	0.3420 0.3333 (0.2319)	-0.2979 -0.2706 (-0.3113)
Pitch [deg]	-0.0005 -0.0005 (0.0)	0.0409 0.0406 (0.04584)	0.0409 0.0406 (0.04584)	0.1455 0.1448 (0.157)	-0.1383 -0.1383 (-0.1688)
Yaw [deg]	-0.0173 -0.0171 (0.0)	0.0981 0.0974 (0.1076)	0.0966 0.0959 (0.1076)	0.3026 0.3186 (0.3357)	-0.4166 -0.4112 (-0.3508)

Table 3.13 Statistics of Responses; Container Ship of 3-body Case

Motion	*Mean*	*RMS*	*STD*	*Max*	*Min*
Surge [m]	-0.4910 -0.4702 (0.0)	1.0654 1.0189 (1.036)	0.9455 0.9039 (1.036)	2.553 2.478 (3.41)	-4.052 -4.038 (-4.363)
Sway [m]	-0.15 -0.03 (-0.05)	0.5848 0.4736 (0.28)	0.5652 0.4726 (0.2755)	1.45 1.45 (1.15)	-2.25 -1.74 (-0.85)
Heave [m]	0.0048 0.0053 (0.00036)	0.2214 0.2191 (0.1716)	0.2213 0.2191 (0.1716)	0.9223 0.8987 (0.5341)	-0.7321 -0.7227 (-0.5796)
Roll [deg]	-0.0699 0.0023 (0.0)	0.5416 0.5066 (0.4818)	0.5372 0.5066 (0.4818)	1.989 1.992 (2.167)	-1.920 -1.795 (-2.182)
Pitch [deg]	-0.0103 -0.0102 (0.0)	0.1269 0.1264 (0.1528)	0.1265 0.1260 (0.1528)	0.3952 0.3924 (0.5886)	-0.4461 -0.4386 (-0.5271)
Yaw [deg]	-0.0031 -0.0013 (0.0)	0.1829 0.1774 (0.1975)	0.1829 0.1774 (0.1975)	0.6454 0.6266 (0.7379)	-0.5976 -0.5742 (-0.6378)

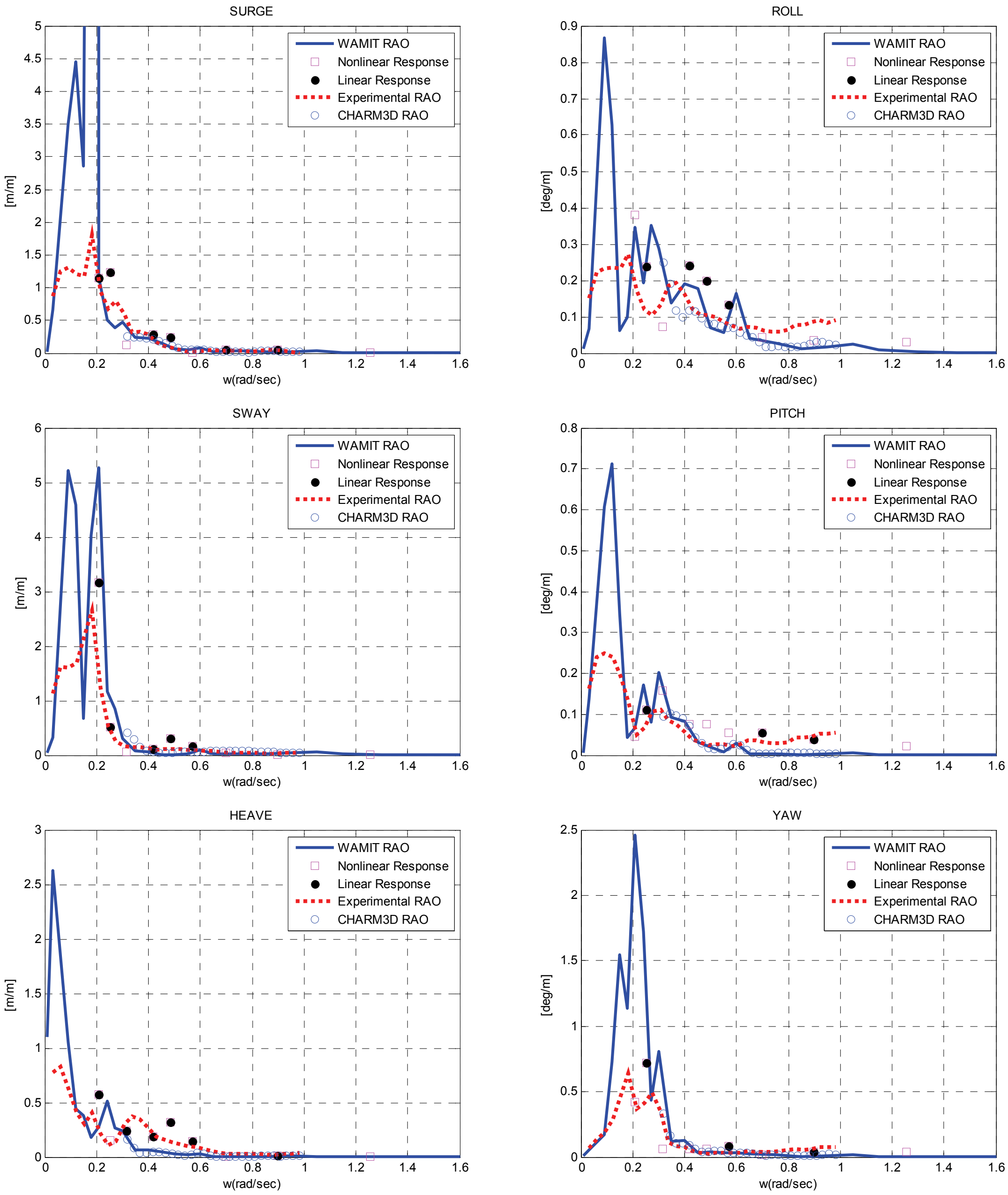

Figure 3.44 Total RAO Comparison of Floating Quay, 3-body Case

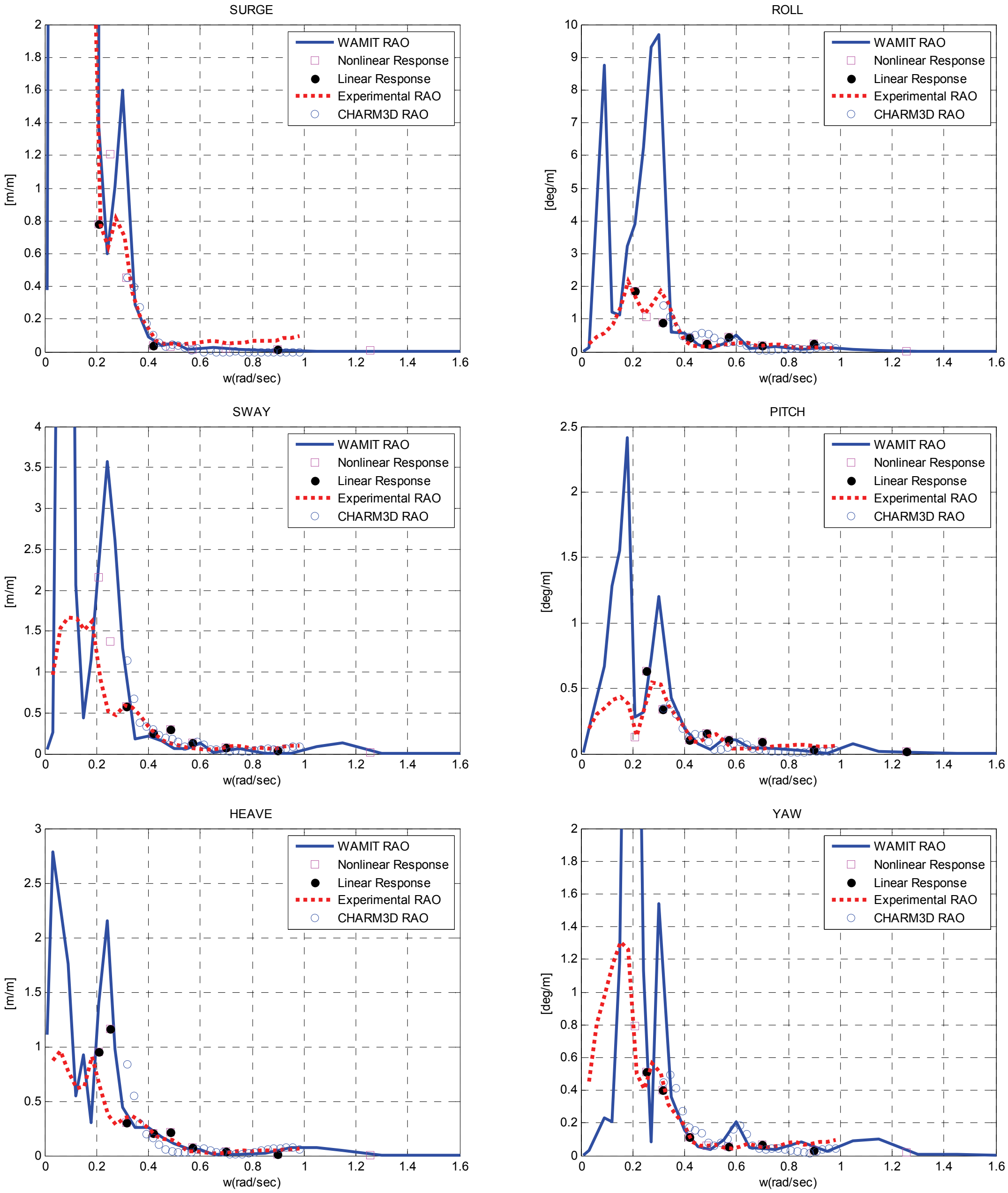

Figure 3.45 Total RAO Comparison of Container Ship, 3-body Case

3.3.3.5 Comparison of Fender Force

From a couple of calibration processes and smoothing drift force the current numerical analysis on time domain can be considered as optimized one fit to the experiment. In that, the final responses as above are assumed to be the best results from the optimized simulation.

Using the responses, the fender forces of the floating quay are compared between experiment and simulation. While the fender force of the experiment is data directly measured in the experiment, the fender force of the simulation is obtained by multiplication of response and stiffness.

To calculate the fender force from the responses, the measuring points in the simulation are assigned as same as the experimental measuring points, which are indicated as a series of Fx, Fy in Fig. 3.1. The positions are given in Table 3.14.

Table 3.14 Measuring Points of Fender Force

Position	**Coordinates**
Fx1, Fy1	195, -40, 0.1
Fx2, Fy2	195, 40, 0.1
Fx3, Fy3	-195, 40, 0.1
Fx4, Fy4	-195,-40, 0.1

At each time step, positions of the four points after the 6DOF displacements are calculated, and then differences from the initial positions is multiplied by the stiffness of surge and sway as the fender force at each step.

If the initial positions are x, y, z, the final position X, Y, Z after 6 DOF displacements $D_x, D_y, D_z, \theta_x, \theta_y, \theta_z$ are obtained by matrix multiplication as

$$\begin{bmatrix} X \\ Y \\ Z \end{bmatrix} = \begin{bmatrix} \cos\theta_z & -\sin\theta_z & 0 \\ \sin\theta_z & \cos\theta_z & 0 \\ 0 & 0 & 1 \end{bmatrix} \begin{bmatrix} \cos\theta_y & 0 & -\sin\theta_y \\ 0 & 1 & 0 \\ \sin\theta_y & 0 & \cos\theta_y \end{bmatrix} \begin{bmatrix} 1 & 0 & 0 \\ 0 & \cos\theta_x & -\sin\theta_x \\ 0 & \sin\theta_x & \cos\theta_x \end{bmatrix} \begin{bmatrix} x \\ y \\ z \end{bmatrix} + \begin{bmatrix} D_x \\ D_y \\ D_z \end{bmatrix} \tag{3.9}$$

And the fender force at each step is calculated by

$$\begin{bmatrix} F_x \\ F_y \end{bmatrix} = \begin{bmatrix} K_x & 0 \\ 0 & K_y \end{bmatrix} \begin{bmatrix} X - x \\ Y - y \end{bmatrix} \tag{3.10}$$

Fig. 3.46 is the comparison of the fender forces between the simulation and experiment, and they generally show good correspondence; however, the sway fender force at point #2 has large peaks in the experimental results set, and the sway fender force at point #4 show overestimated results of the simulation as much as about one and a half times than those of the experiment. Statistics from the results are summarized in Table 3.15. Between two rows of each measuring point, the first row represents the statistics of simulation, and the next row is experimental results.

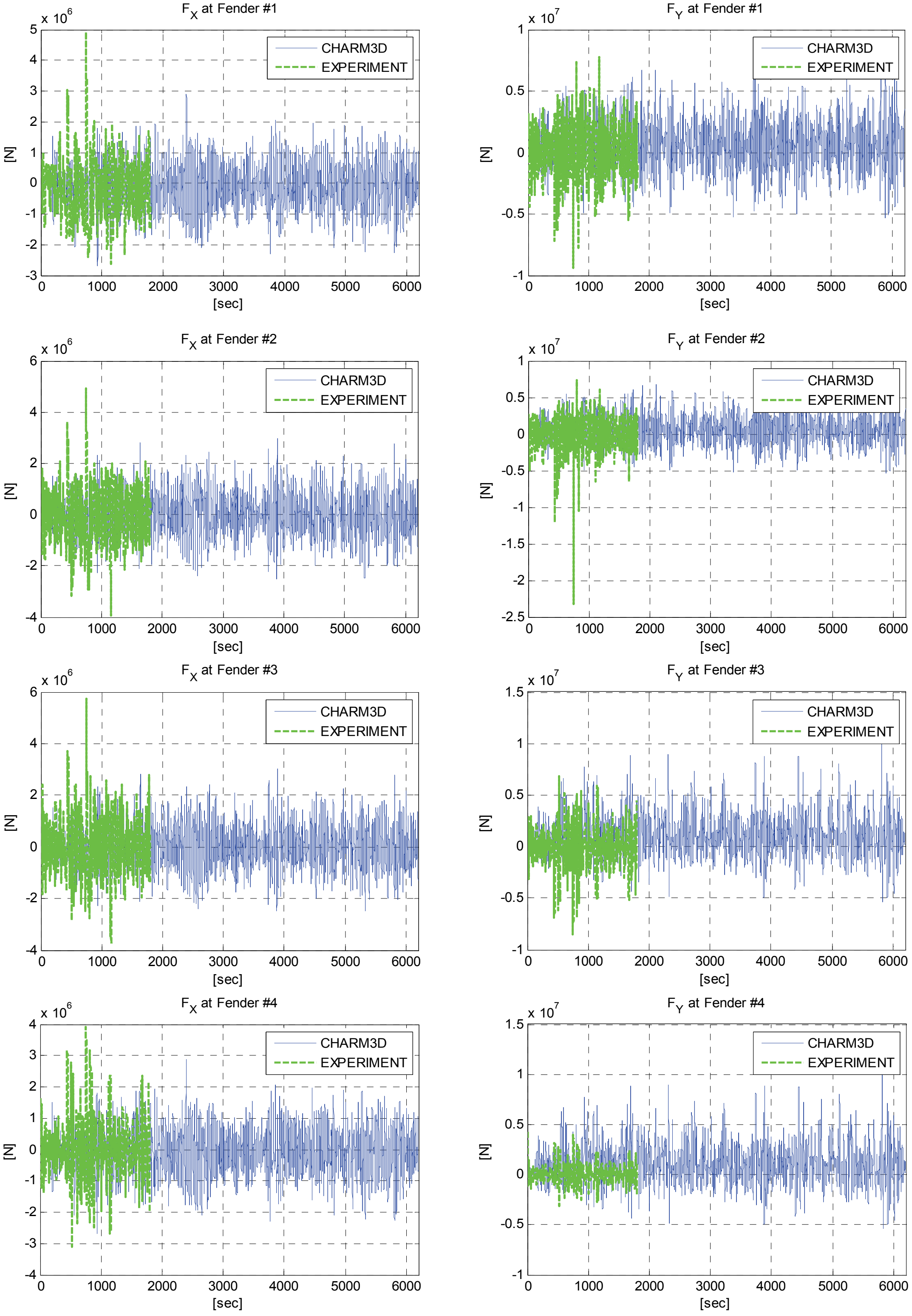

Figure 3.46 Comparison Fender Force

Table 3.15 Statistics of Fender Force

Measuring Points	*Mean*	*RMS*	*STD*	*Max*	*Min*
Fx1	-7.576E+4	722980.3	0.719E+6	2.890E+6	-2.702E+6
	-1.158E+5	948495.4	9.414E+5	4.916E+6	-2.629E+6
Fy1	6.159E+5	2058307	1.964E+6	8.976E+6	-5.352E+6
	4.833E+4	2161540	2.161E+6	7.767E+6	-9.409E+6
Fx2	2.204E+4	807900.7	8.076E+5	2.989E+6	-2.499E+6
	1061	1056001	1.056E+6	4.930E+6	-3.951E+6
Fy2	6.151E+5	2058068	1.964E+6	8.973E+6	-5.355E+6
	-2.085E+5	2407047	2.398E+6	7.415E+6	-2.315E+7
Fx3	2.473E+4	808578.3	8.082E+5	3.026E+6	-2.485E+6
	2.806E+4	1058372	1.058E+6	5.751E+6	-3.752E+6
Fy3	1.133E+6	2330018	2.036E+6	1.138E+7	-5.360E+6
	-3.138E+4	1846267	1.846E+6	6.786E+6	-8.527E+6
Fx4	-0.731E+5	722507.5	7.188E+5	2.894E+6	-2.696E+6
	1.024E+4	856361.2	8.563E+5	3.927E+6	-3.099E+6
Fy4	1.134E+6	2331378	2.037E+6	1.138E+7	-5.357E+6
	1.052E+4	861864.2	8.618E+5	4.246E+6	-3.090E+6

3.3.3.6 Relative Motions

To examine the relative motions, at first two sets of target positions are assigned, as shown in Table 3.16. From Fig. 3.47 the targeted points of the floating quay are picked as crane operating rooms, and targeted points of the container ship are positions horizontally identical to the operating rooms but on the top of the container ship as working scope of the cranes. At the points, the horizontal and vertical relative displacements are calculated as shown in Fig. 3.48, and the statistics are obtained as given in Table 3.17; all the relative motions are calculated from the final results of the optimized simulation. In the Table 3.17, at each measuring points the first row presents the heave relative motion and the second row represents horizontal relative motion.

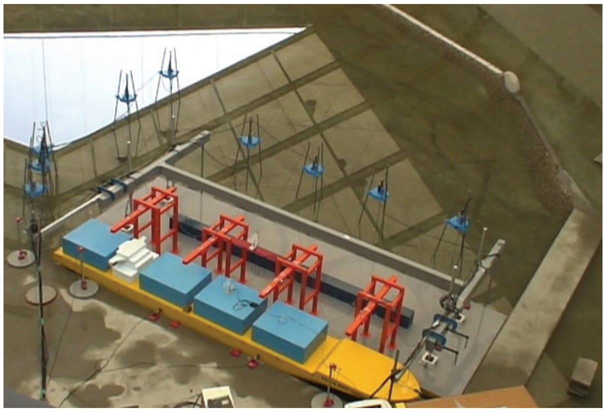

Figure 3.47 Schematic of 3-body Case

Table 3.16 Measuring Points of Relative Displacements

Measuring Point	*Floating Quay*	*Container Ship*
1	132.25 , 94 , 77	132.25 , 0 , 35
2	43.25 , 94 , 77	43.25 , 0 , 35
3	-43.25 , 94 , 77	-43.25 , 0 , 35
4	-132.25 , 94 , 77	-132.25 , 0 , 35

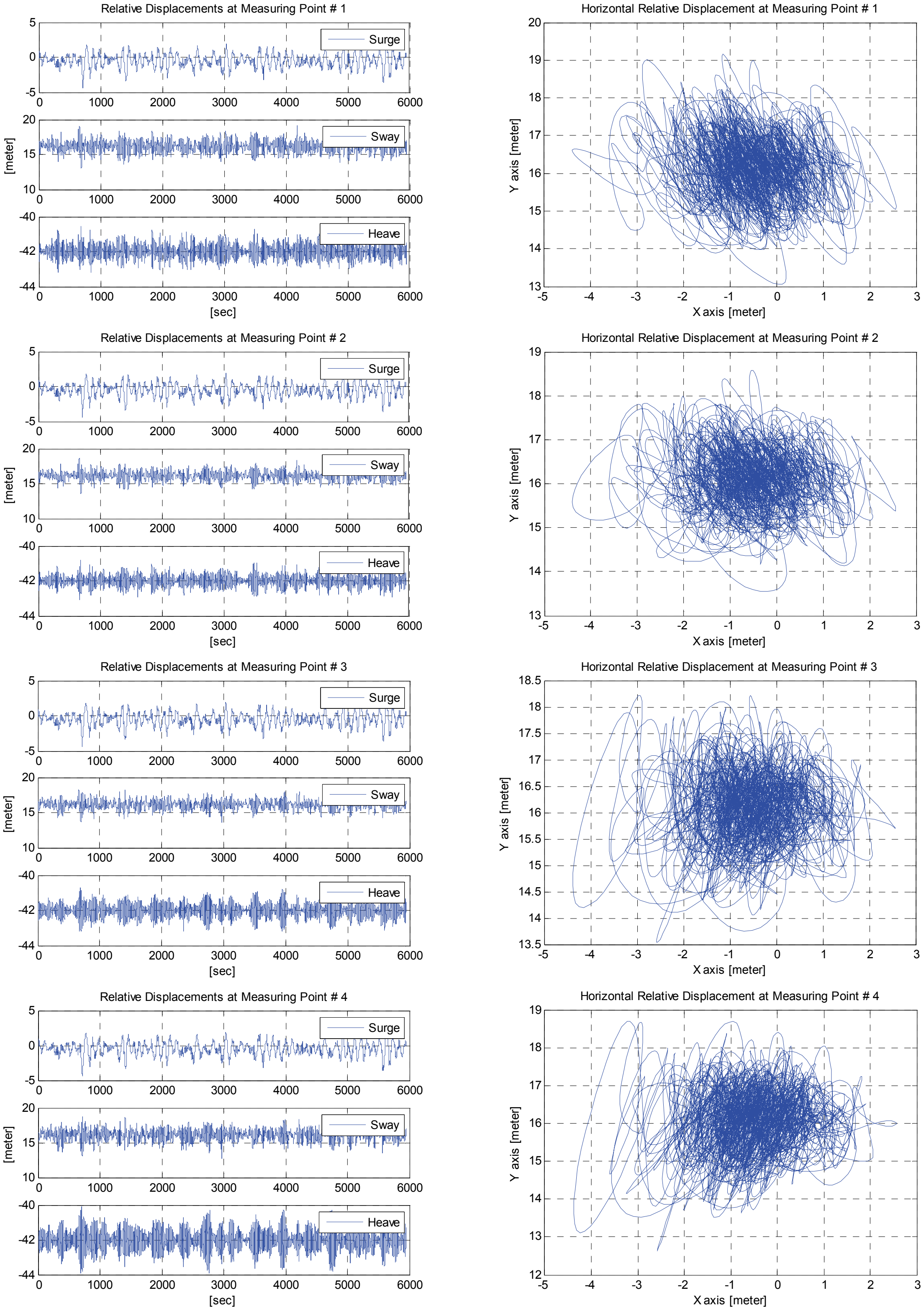

Figure 3.48 Relative Displacements on Cranes

Table 3.17 Statistics of Relative Motions at Cranes

Measuring Points	*Mean*	*RMS*	*STD*	*Max*	*Min*
#1	-41.97 16.17	41.27 16.19	0.3987 0.8209	-40.55 19.16	-43.20 13.05
#2	-41.99 16.15	41.99 16.16	0.3121 0.6589	-40.79 18.57	-43.09 13.54
#3	-42.00 16.12	42.00 16.13	0.3927 0.6460	-40.70 18.22	-43.20 13.54
#4	-42.02 16.10	42.02 16.12	0.5767 0.7889	-40.08 18.69	-43.92 12.65

Next, relative motions of 6 DOF responses of the container ship with respect to the floating quay are compared between the simulation and the experiment in Fig. 3.49, and statistics of the responses are summarized in Table 3.18.

Table 3.18 Statistics of 6DOF Relative Motions

Motions	*Mean*	*RMS*	*STD*	*Max*	*Min*
Surge	-0.464/0.0	1.003/1.156	0.890/1.156	2.298/4.229	-3.981/-4.89
Sway	-0.223/0.0	0.633/0.329	0.593/0.329	1.729/1.147	-2.583/-1.032
Heave	0.016/0.0	0.259/0.248	0.259/0.248	1.093/0.697	-0.829/-0.643
Roll	-0.005/0.0	0.507/0.470	0.507/0.470	1.986/2.215	-1.758/-2.212
Pitch	-0.010/0.0	0.159/0.172	0.159/0.172	0.518/0.615	-0.545/-0.579
Yaw	0.016/0.0	0.216/0.202	0.216/0.202	0.767/0.712	-0.626/-0.688

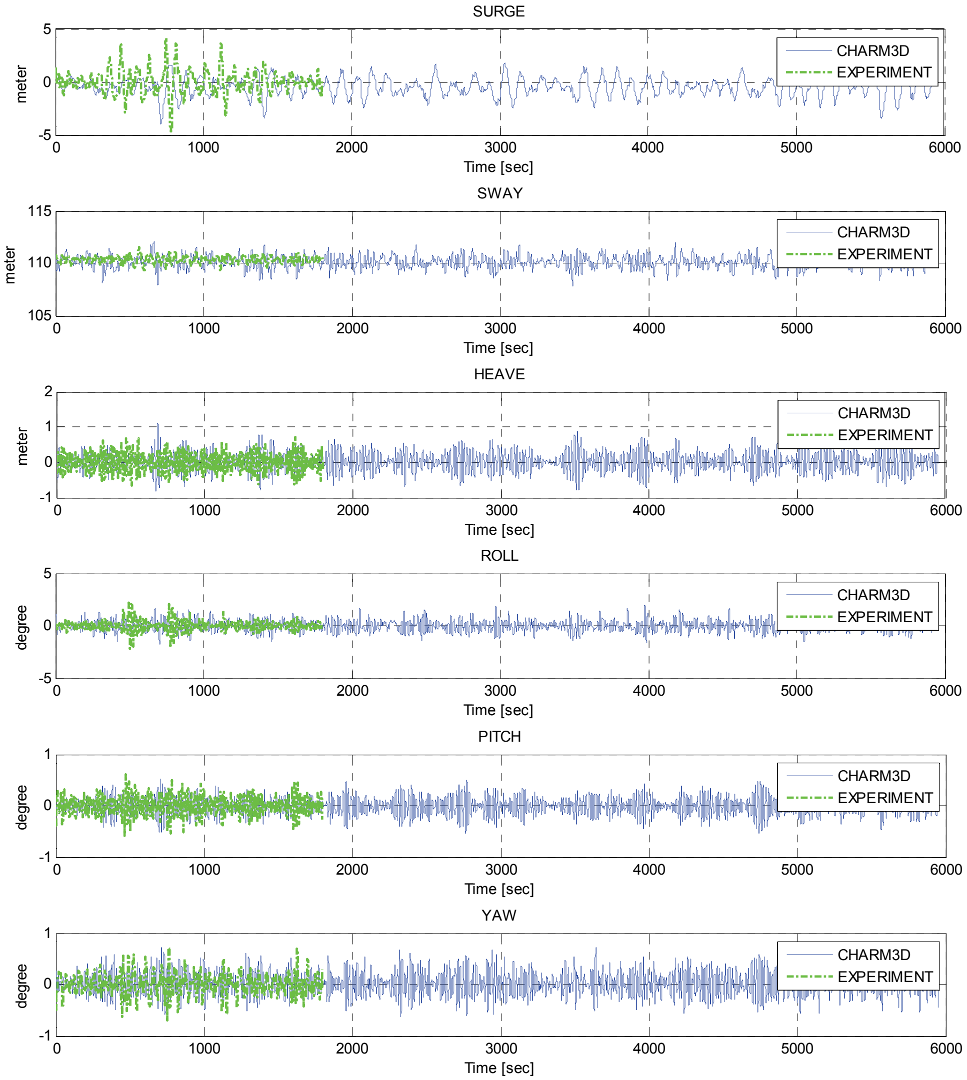

Figure 3.49 Relative Response Histories for 6 DOF Motions

3.3.3.7 Acceleration at Crane Operating Room

To examine operability of the cranes, accelerations at the operating rooms are calculated from the response histories of the simulation; if the acceleration is over a certain critical value, the operator would be interrupted by the noticeable acceleration, and thus it consider as one of parameters to operate in the cranes.

Limit of the acceleration is assumed from the KORDI such that Root Mean Square (RMS) of the acceleration should be less than $0.2\mathrm{m/s^2}$; as this value is temporarily given limit, there are no clear references for operability of such vast floating structures.

The positions of the crane operating room are assumed to be same as the measuring points of the floating quay in the Table 3.16. In Fig. 3.50, horizontal and heave accelerations are shown, and statistics of the results are given in Table 3.19. In the table, two rows of each measuring point represent statistics of horizontal acceleration by the first row and those of heave acceleration by the next row, respectively. The table shows that all the RMS is within the limit.

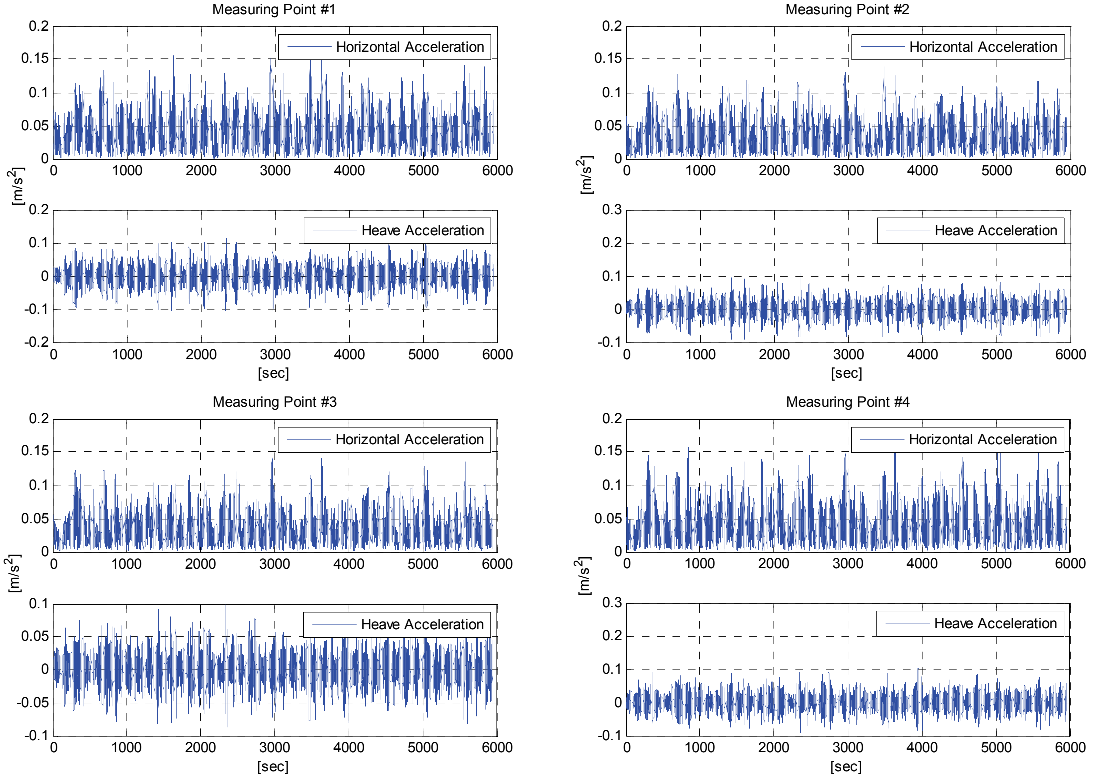

Figure 3.50 Accelerations at Crane Operating Rooms

Table 3.19 Statistics of Accelerations at Crane Operating Rooms

Measuring Points	*Mean*	*RMS*	*STD*	*Max*	*Min*
#1	0.0438 0.0	0.0502 0.0313	0.0246 0.0313	0.1681 0.1157	0.0003 -0.1049
#2	0.0391 0.0	0.0448 0.0268	0.0218 0.0268	0.1389 0.1072	0.0002 -0.0925
#3	0.0396 0.0	0.0455 0.0254	0.0225 0.0254	0.1413 0.0991	0.0001 -0.0872
#4	0.0451 0.0	0.0523 0.0273	0.0265 0.0273	0.1708 0.1028	0.0004 -0.0916

3.4 Comparison with Conventional Harbor System

As an additional numerical analysis, a conventional harbor system is investigated and compared with the floating harbor system on frequency domain and time domain, which consists of only two bodies: the fixed harbor on the port of the container ship, as shown in Fig. 3.51.

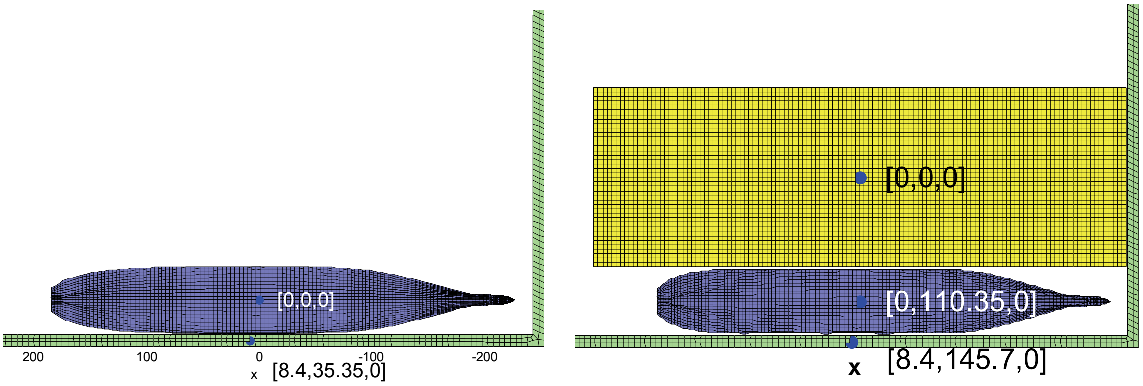

Figure 3.51 Schematic Comparison: Conventional Harbor System (Left), Floating Harbor System(Right)

In particular, the hydrodynamic properties and responses of the container ship are compared between two cases: one is the ship in the conventional floating harbor system, and the other is the ship in the floating harbor system.

Inputs of the simulation for the conventional harbor system are identical to those of the container ship and fixed quay in the three-body floating harbor system.

For frequency domain analysis of the conventional harbor system, boundary condition is same as the three-body case. To input the geometric information, the same panel coordinates are used only for the container ship and fixed quay. The body coordinate system of the container ship is coincided with the global coordinate system, and the longitudinal gap is fixed as 1.6 meter. The external dynamic information is adopted from the two-body case for the fixed quay, and that of the container ship is taken up from the values in the three-body case after the first calibration as external stiffness revision. Using WAMIT, the hydrodynamic properties and RAO are calculated, and the results are compared with those of the container ship in the three-body case, as shown in Fig. 3.52 to Fig. 3.56; as mentioned in Section 3.2.5, mean drift forces/moments are smoothed to account for reduced pumping peaks by viscous effect.

For time domain analysis of the conventional harbor system, sea state conditions are same as the previous cases, and drift force is applied through Newman's Approximation in the same manner with other cases. The damping coefficients are fixed as the values after the second calibration of damping estimation in the three-body case such that $C_D = 8$ for drag plates toward sway motion and $\alpha = 20\%$ to obtain the linear roll damping coefficients, as described in Section 3.3.3.3. The response histories of the container ship in the conventional harbor system are compared with those in the three-body case in Fig. 3.57 to Fig. 3.58.

From comparisons of the response histories, the responses of the container ship in the conventional system are generally larger than those in the floating harbor system; in Table 3.20 statistics for the comparison of container ship responses are summarized, and they show clearly larger responses for all 6 DOF motions in the conventional harbor system.

Thus, it would be advantage from the floating harbor system that the motions of the container ship become more stable.

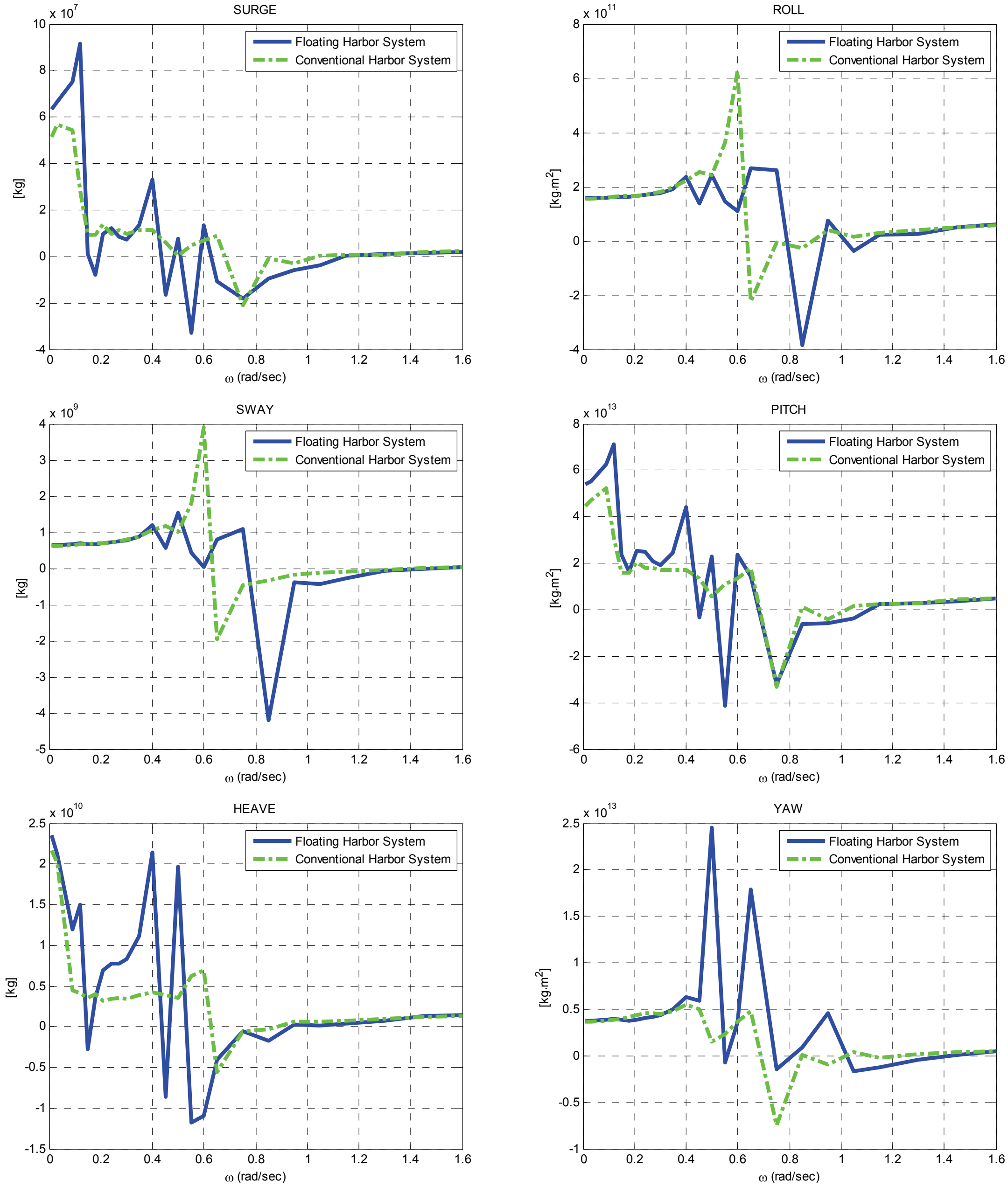

Figure 3.52 Comparison of Added Mass/Moment of Inertia between 2 Cases: Floating Harbor System and Conventional Harbor System

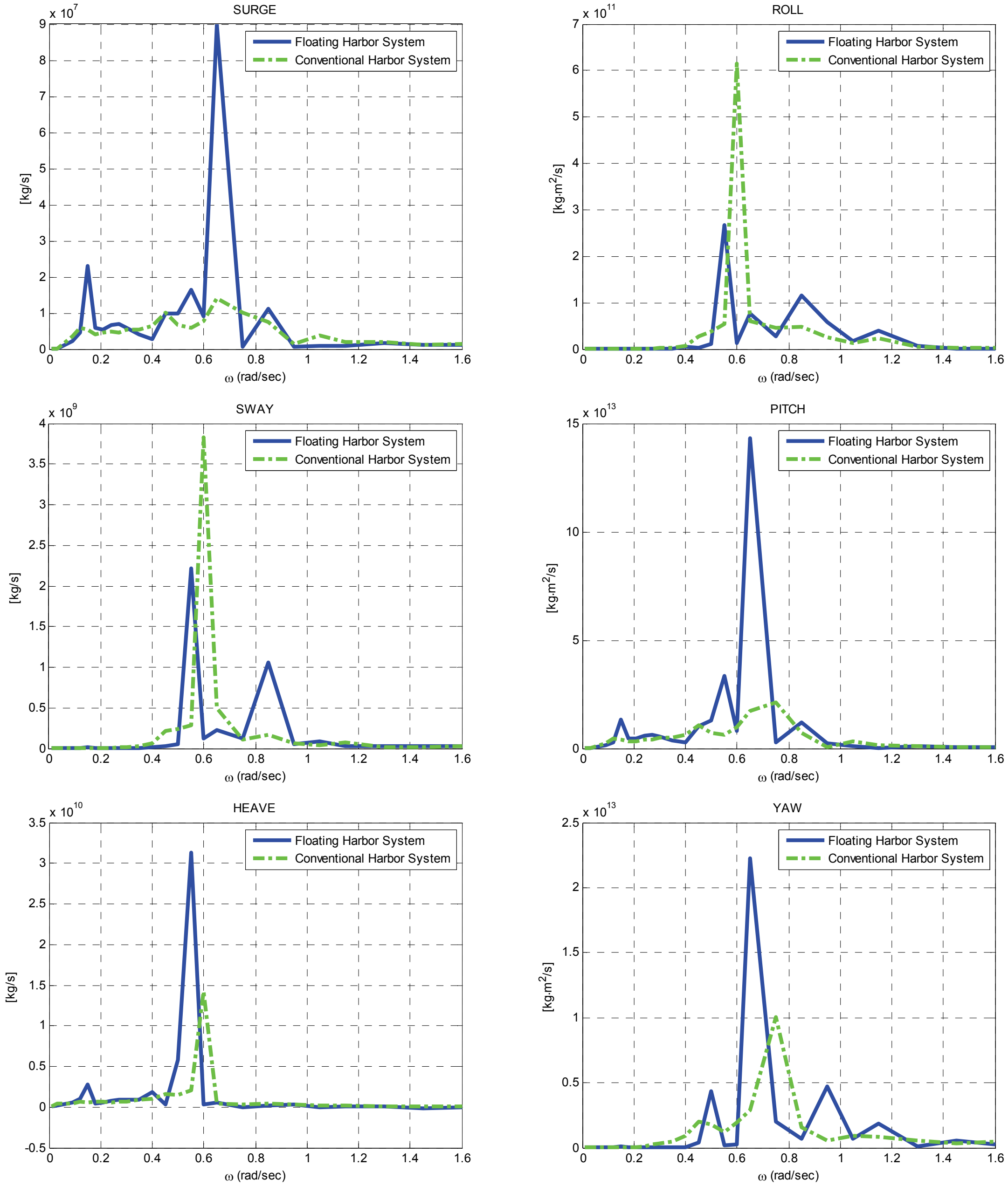

Figure 3.53 Comparison of Radiation Damping Coefficients between 2 Cases: Floating Harbor System and Conventional Harbor System

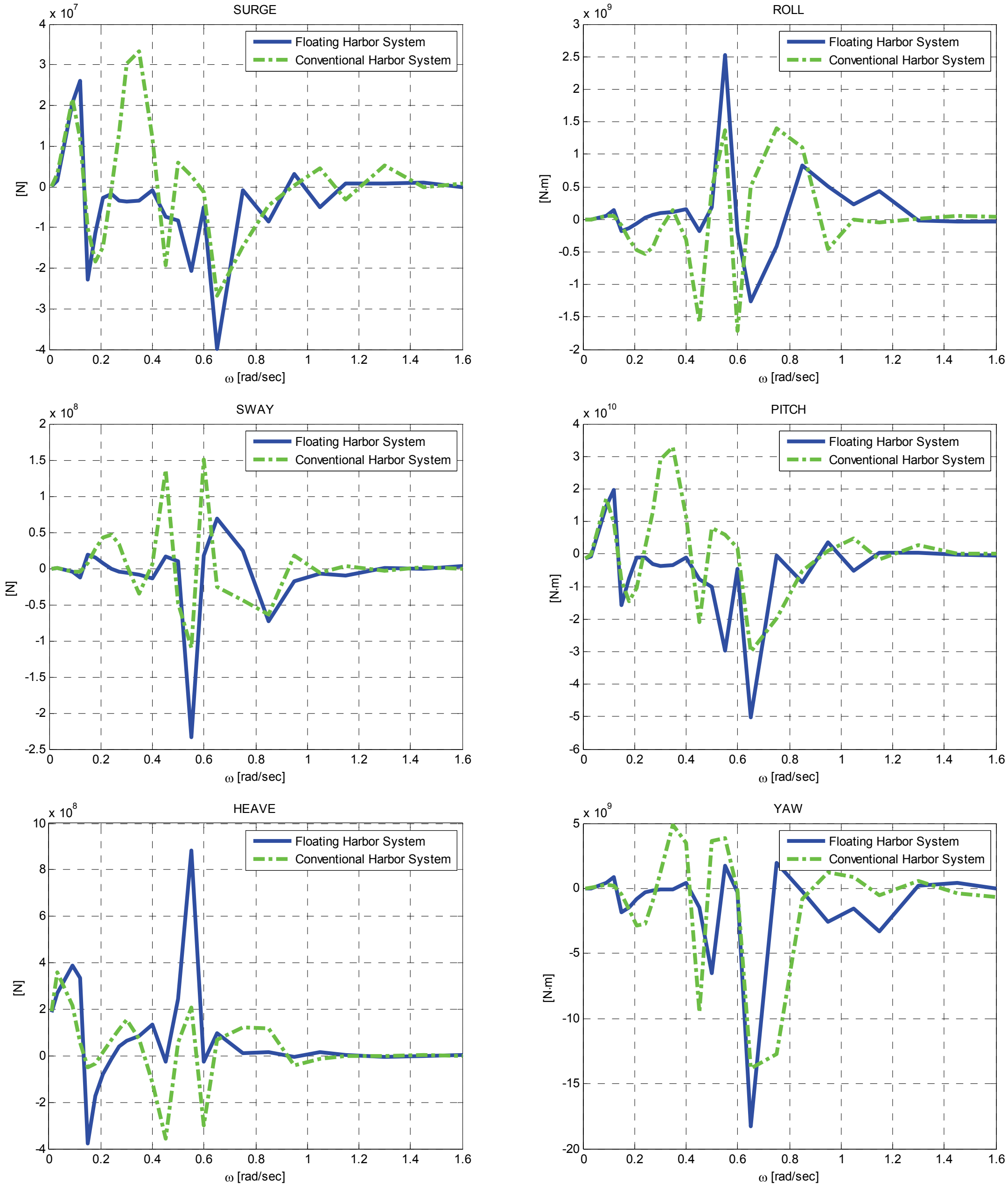

Figure 3.54 Comparison of Wave Exciting Force/Moment between 2 Cases: Floating Harbor System and Conventional Harbor System

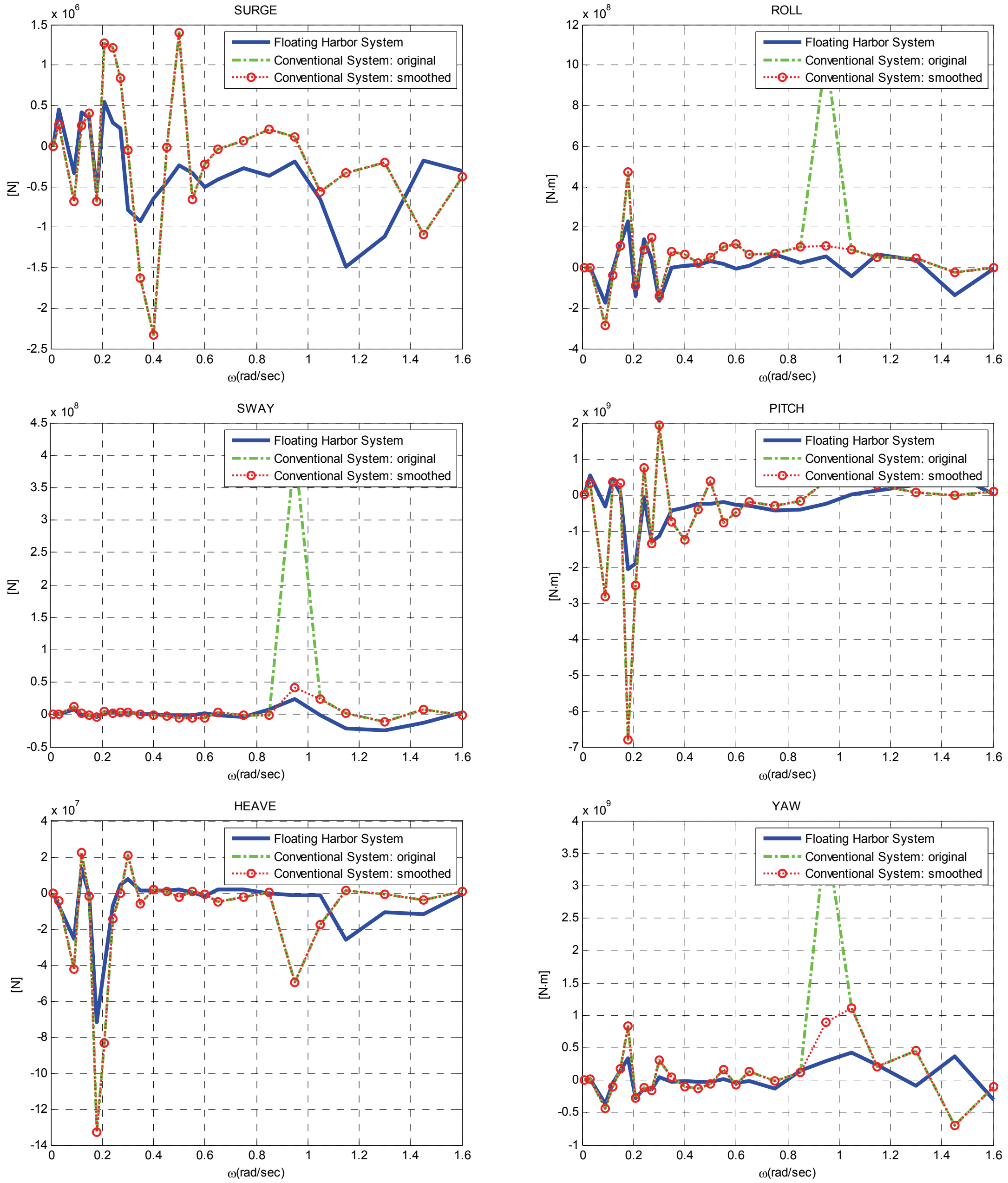

Figure 3.55 Comparison of Smoothed Drift Force/Moment between 2 Cases: Floating Harbor System and Conventional Harbor System

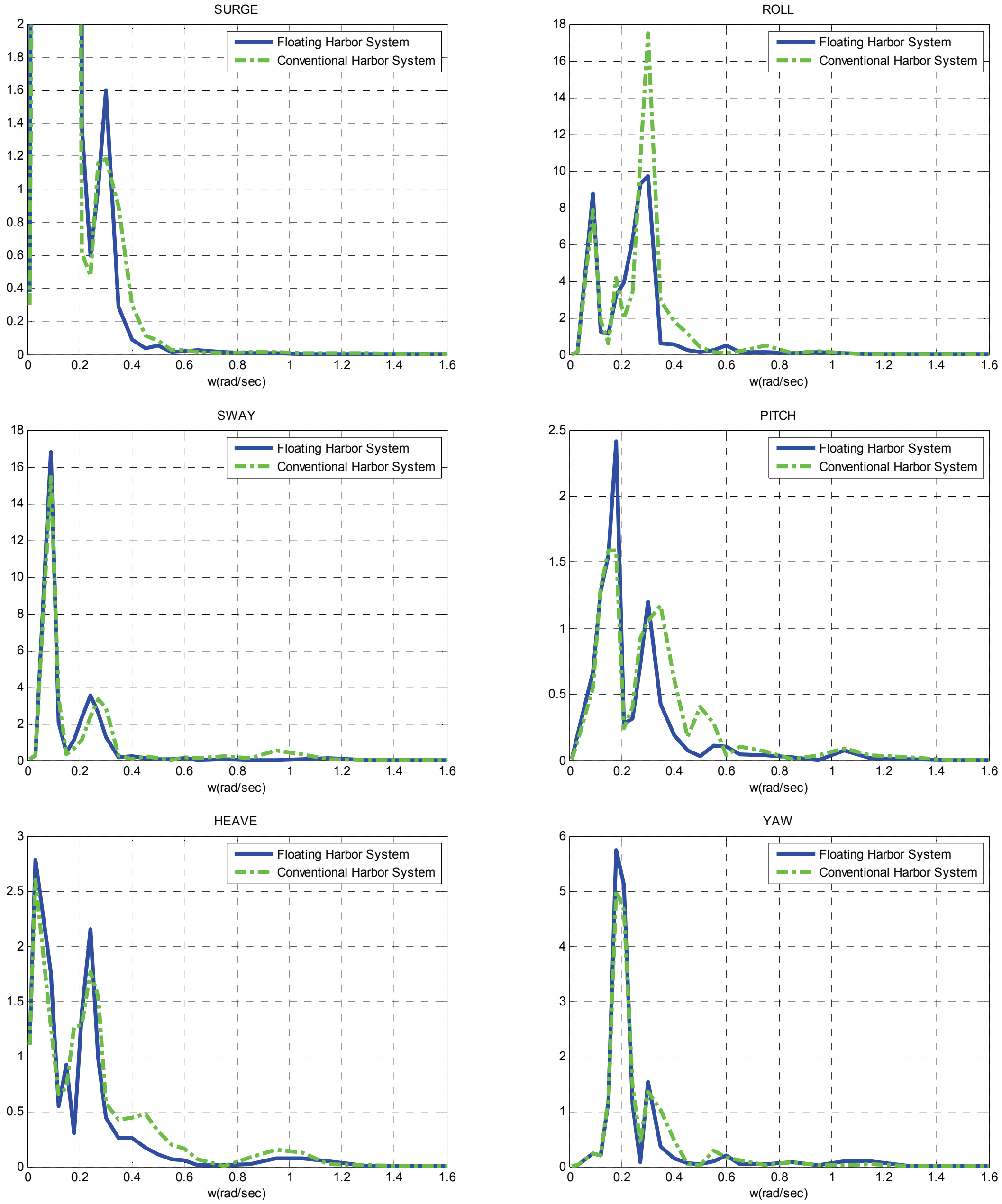

Figure 3.56 Comparison of RAO between 2 Cases: Floating Harbor System and Conventional Harbor System

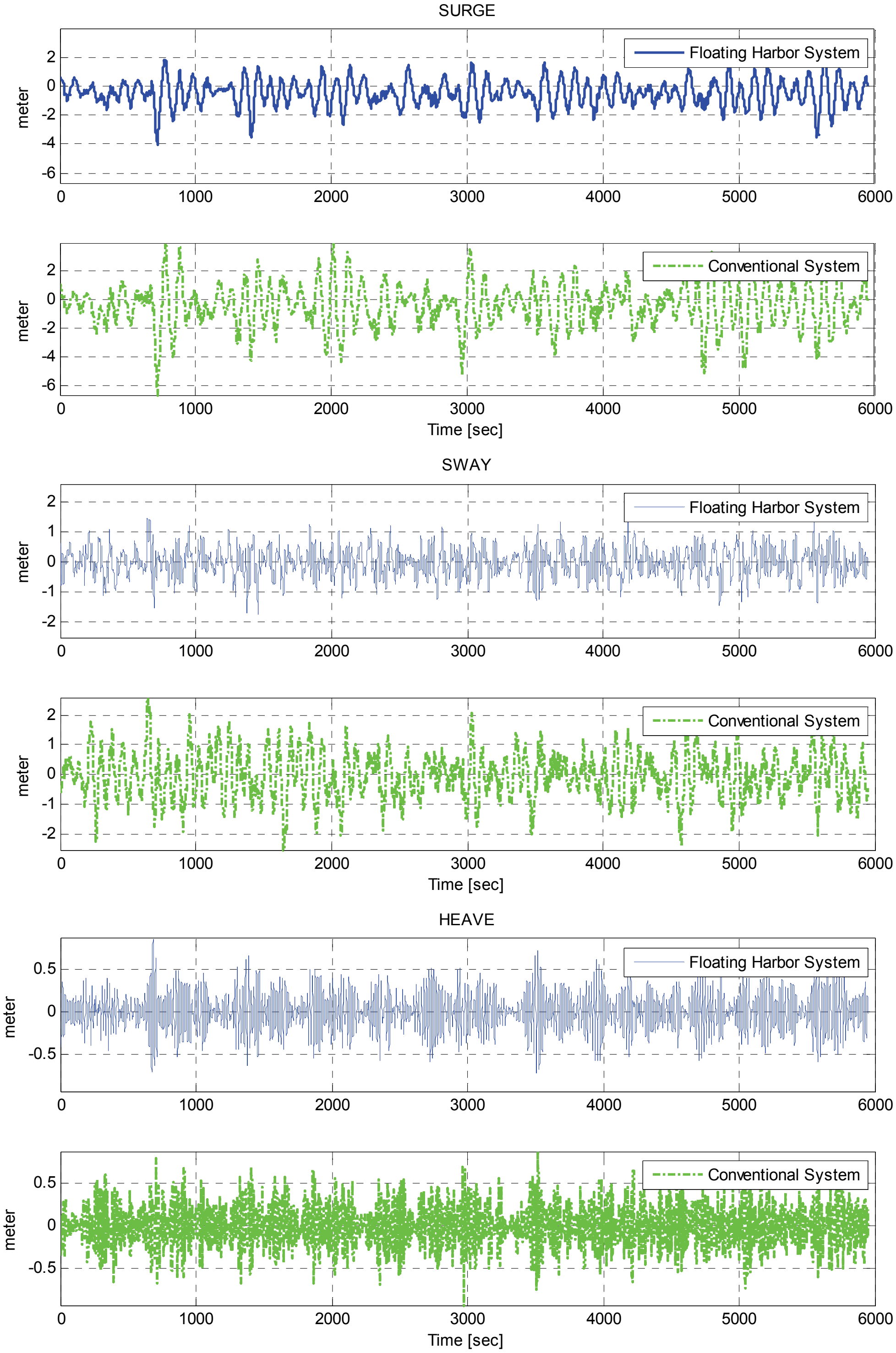

Figure 3.57 Comparison of Response Histories for Surge, Sway, Heave between 2 Cases: Floating Harbor System and Conventional Harbor System

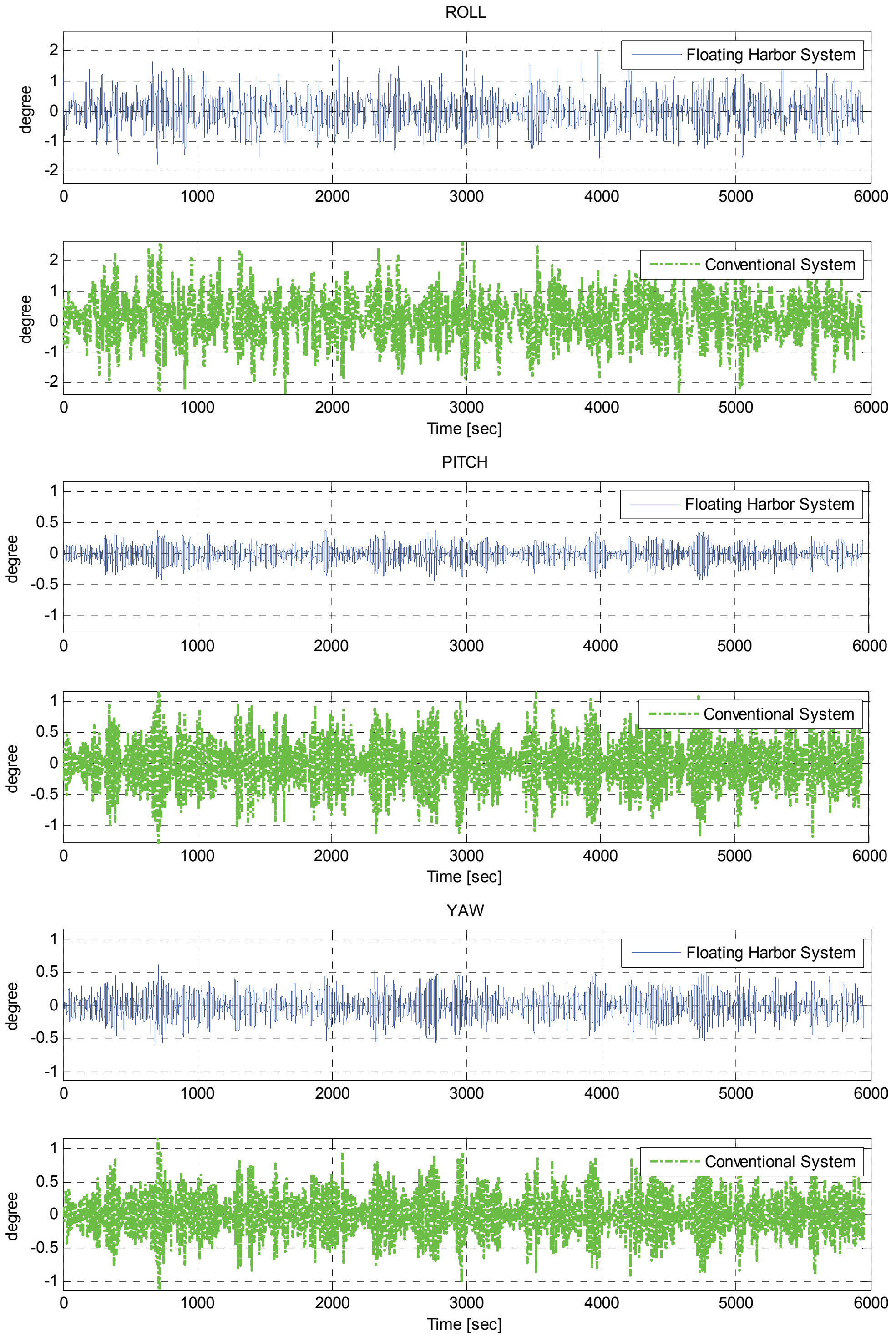

Figure 3.58 Comparison of Response Histories for Roll, Pitch, Yaw between 2 Cases: Floating Harbor System and Conventional Harbor System

Table 3.20 Statistics of Comparison with Conventional Harbor System

Motions	*Mean*	*RMS*	*STD*	*Max*	*Min*
Surge	-0.470	1.019	0.904	2.478	-4.038
	-0.426	1.577	1.518	3.906	-6.665
Sway	-0.026	0.474	0.473	1.451	-1.742
	-0.034	0.769	0.768	2.590	-2.531
Heave	0.005	0.219	0.219	0.899	-0.723
	-0.004	0.234	0.234	0.867	-0.936
Roll	0.002	0.507	0.507	1.992	-1.795
	0.137	0.752	0.739	2.650	-2.381
Pitch	-0.010	0.126	0.126	0.392	-0.439
	-0.009	0.370	0.370	1.170	-1.261
Yaw	-0.001	0.177	0.177	0.627	-0.574
	0.010	0.306	0.306	1.155	-1.122

3.5 Operating Sea State Condition

Based on the optimized numerical analysis tool for the 3-body floating harbor system, the global performances of the 3-body floating harbor system are investigated for an operating wave condition as described in Table 3.21; up to this point, the sea state used in numerical analysis and experiment was survival condition.

Table 3.21 Operating Sea State Condition

	Significant Wave Height (m)	*Peak Period(s)*
Survival Condition	2.8	15.5
Operating Condition	0.88	7.5

The results from the operating condition and the survival condition are compared in terms of statistics of relative motions for the container ship with respect to the floating quay in Table 3.22; Fig. 3.59 and Fig. 3.60 represent 6 DOF responses of the two floating bodies in the operating sea state condition.

Table 3.22 Comparison of Relative Motions between 2 Sea State Conditions: Operating Condition and Survival Condition

Motions	*Mean*	*STD*	*Max*	*Min*
Surge	-0.0449 0.4639	0.1490 0.8995	0.4312 2.2980	-0.5035 -3.9810
Sway	-0.0894 -0.2229	0.3712 0.5930	1.0995 1.7294	-1.6613 -2.5832
Heave	0.0000 0.0160	0.0347 0.2590	0.1103 1.0930	-0.1267 -0.8288
Roll	-0.0014 -0.0047	0.1761 0.5065	0.5905 1.9860	-0.6117 -1.7580
Pitch	-0.0004 -0.0097	0.0094 0.1588	0.0381 0.5176	-0.0434 -0.5453
Yaw	0.0032 0.0158	0.0338 0.2162	0.1330 0.7670	-0.1404 -0.6264

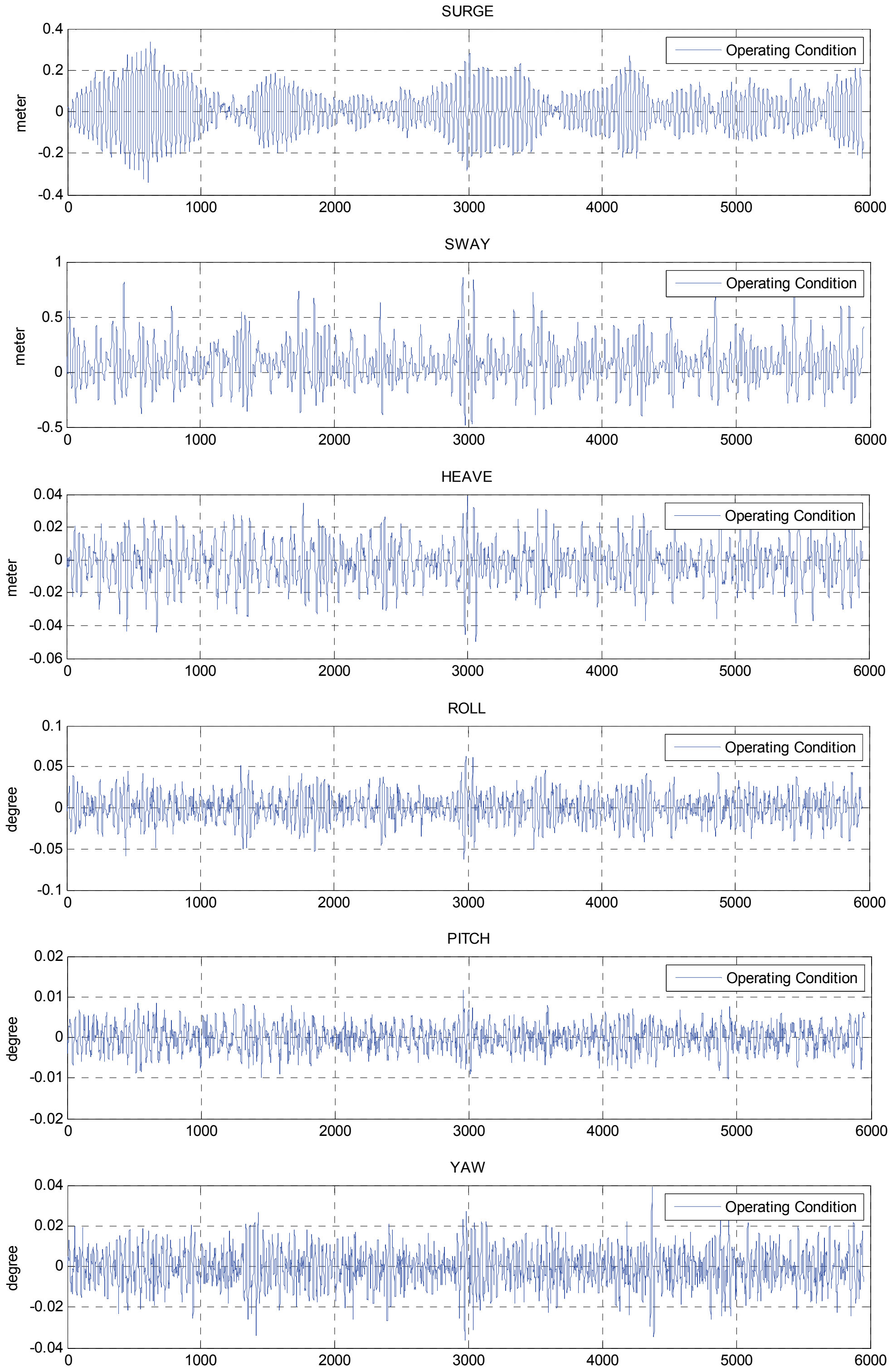

Figure 3.59 Response Histories of Floating Quay to Operating Sea State, 3-body Case

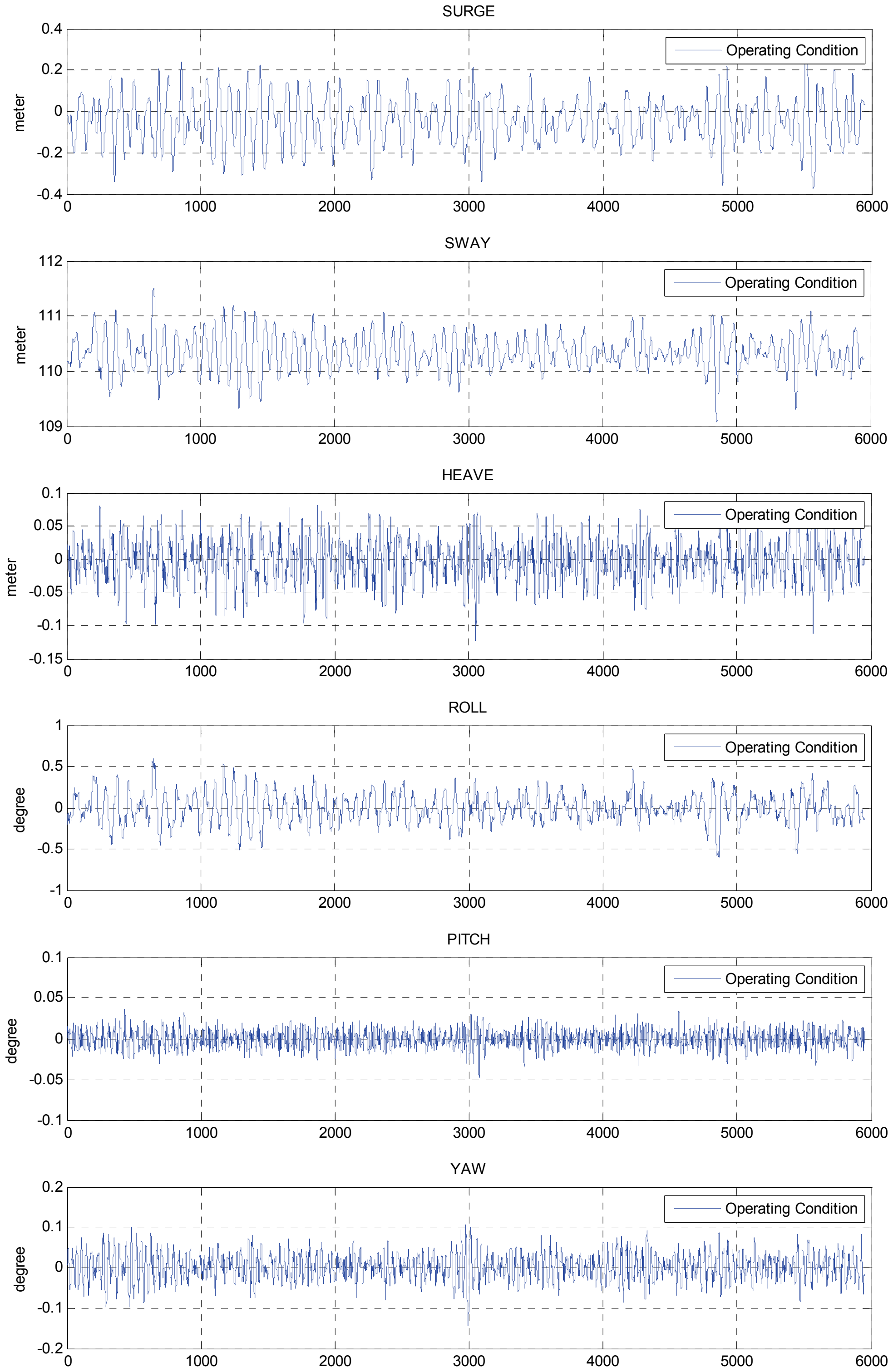

Figure 3.60 Response Histories of Container Ship to Operating Sea State, 3-body Case

CHAPTER IV

CONCLUSION

Results from the numerical analysis are generally well matched with those of the experiment on both of frequency and time domains using WAMIT and CHARM3D with three additional processes: revising external stiffness, estimating damping coefficients, and smoothing drift forces/moments.

For the large scale of the floating quay and the container ship with remarkably narrow gap, finer panels are used since the hydrodynamic properties are more sensitive to the panel size, and mean drift forces/moments are smoothed.

Considering resonance phenomenon the external stiffness is revised to get the natural frequency of simulation matched with that of the experiment. In addition, as natural frequencies are practically placed in low frequency region, a frequency region to be analyzed is extended to 0.01 rad/sec. After that, damping coefficients are revised to match responses between numerical analysis and experiment on time domain.

Results from the optimal simulation show good correspondence with experiment in terms of RAO on frequency domain and response histories on time domain. And dolphin fender force also has good agreement between the simulation and experiment except for certain strange peaks in experiments; the correspondences represent reliability and capability not only for the optimized numerical analysis but the experiment. Furthermore, the research shows the feasibility and benefits of the floating harbor system.

REFERENCES

Buchner, B., Dijk, A., Wilde, J., 2001. Numerical Multiple-body Simulations of Side-by-side Mooring to an FPSO. In Proceedings of the Eleventh International Offshore and Polar Engineering Conference, Stavanger, Norway, 343-353.

Buchner, B., Gerrit, B., Jaap, W., 2004. The Interaction Effects of Mooring in Close Proximity of Other Structures. In Proceedings of 14th International Society of Offshore and Polar Engineers Conference, Toulon, France, 297-306.

Charkrabarti, S., 2001. Empirical Calculation of Roll Damping for Ships and Barges. Ocean Engineering, 28, 915-932.

Cummins, W., 1962. The Impulse Response Function and Ship Motion. Technical Report 1661, David Taylor Model Basin-DTNSRDC.

Choi, Y.R., Hong, S.Y., 2002. An Analysis of Hydrodynamic Interaction of Floating Multi-body Using Higher-order Boundary Element Method. In Proceedings of the Twelfth International Offshore and Polar Engineering Conference, Kitakyushu, Japan, 303-308.

Chen, H.C., Huang E. T., 2004. Time-domain Simulation of Floating Pier/Ship Interactions and Harbor Resonance. In Proceedings of the Fourteenth International Offshore and Polar Engineering Conference, Toulon, France, Volume I, 772-774.

Hong, S.Y., Kim, J.H., Cho, S.K., Choi, Y.R., Kim, Y.S., 2005. Numerical and Experimental Study on Hydrodynamic Interaction of Side-by-side Moored Multiple Vessels. Ocean Engineering 32, 783-801.

Huijsmans, R.H.M., Pinkster, J.A., Wilde, J.J., 2001. Diffraction and Radiation of Waves Around Side-by-side Moored Vessels. In Proceedings of the Eleventh International Offshore and Polar Engineering Conference, Stavanger, Norway, 406-412.

Inoue, Y., Islam, M.R., 1999. Comparative Study of Numerical Simulation and

Experimental Results for a Parallely Connected FPSO and LNG in Waves. In Proceedings of the Ninth International Offshore and Polar Engineering Conference, Brest, France, 360-367.

Kim, M. H., 1997. WINTCOL/WINPOST User's Manual. Ocean Engineering Program, Civil Engineering Department, Texas A&M University, College Station, TX.

Kim, M.H., Kumar, B., Chae, J.W., 2006. Performance Evaluation of Loading/Offloading from Floating Quay to Super Container Ship. In Proceedings of the Sixteenth International Offshore and Polar Engineering Conference, San Francisco, CA, 144-149

Kodan, N., 1984. The Motions of Adjacent Floating Structures in Oblique Waves. In Proceedings of the Third International Conference on Offshore Mechanics & Arctic Engineering, 1, 206-213.

Lee, C.H., 1995. WAMIT Theory Manual. Department of Ocean Engineering, Massachusetts Institute of Technology, Cambridge, MA.

Lee, D. H., Kim, M. H. , 2005. Two-body Resonant Interactions by Fully Coupled and Partially Coupled Method. Civil Engineering in the Oceans VI, 494-503

Mercier, R., 2004. Dynamics of Offshore Structures, Class Notes, OCEN-676-600, Texas A&M University, College Station, TX.

Newman, J.N., 1967, Drift Force and Moment on Ships in Waves. Journal of Ship Research, 11, 51-60.

Ran, Z., 2000. Coupled Dynamic Analysis of Floating Structures in Waves and Currents. Ph.D. Dissertation. Texas A&M University, College Station, TX.

Sannasiraj, S.A., Sundaravadivelu, R., Sundar, V., 2000. Diffraction-radiation of Multiple Floating Structures in Directional Waves. Ocean Engineering, 28, 201-234.

VITA

HeonYong Kang received his Bachelor of Science degree in naval architecture and ocean engineering from Pusan National University in August 2008. He entered the Ocean Engineering Program at Texas A&M University in September 2008 and received his Master of Science degree in May 2010. His research interests analysis of floating structures systems and theoretical development of wave mechanics. He plans to pursue his Ph.D. degree and make progress in the analysis and theory of wave mechanics.

Mr. Kang may be reached at: Ocean Engineering Program, Civil Engineering Department, Texas A&M University, College Station, TX 77843-3136.

His email is hykang@tamu.edu.